Multielectron Redox in Lithium-Rich, Industrial-Element Sulfides for High Energy Density Lithium-Ion Battery Cathodes

Thesis by
Eshaan Salim Patheria

In Partial Fulfillment of the Requirements for the
Degree of
Doctor of Philosophy

CALIFORNIA INSTITUTE OF TECHNOLOGY
Pasadena, California

2025
Defended May 30, 2025

Eshaan Salim Patheria
ORCID: 0000-0002-2761-8498

ACKNOWLEDGEMENTS

I consider myself extremely lucky and grateful for the past 6 years at Caltech—I have many people to thank.

First and foremost, Dr. Kimberly A. See, my PhD advisor—being your student has been nothing short of a dream come true. Your impact on my life has been outsized: you have guided me to think critically and creatively, trained me in the art of effective communication, presentation, and writing, and consistently encouraged and wholeheartedly supported me to pursue my dreams—all with utmost patience. Of many special memories, I will always remember a long one-on-one meeting with you, when you were very close to your delivery date for Morgan, spent walking in circles around campus, where I (nervously at first) shared some of my life's long-term dreams and goals with you, which I had written down on your signature goal-setting worksheets. I thought you might consider some of my goals too optimistic or unrealistic, but instead you smiled, encouraged me, and started to rigorously help me plan out how I might achieve those goals. This is what I am most grateful for—your deep commitment to helping me realize my greatest potential and always believing in me (and every one of your students). Your commitment and belief have emboldened me to take risks, to challenge myself, and to grow in ways that only the rarest kind of mentor can enable. Thank you for everything—I am honored, deeply grateful, and extremely excited to keep working with and learning from you beyond my PhD.

Rory Newcomb, forever "Ms. Newcomb" to me—my high school science and International Baccalaureate Biology Higher Level teacher (then) at the American School of Bombay, in Mumbai, India. When it would have been very easy to follow a different, perhaps more comfortable path in life, you pushed me to find greater purpose in my work. You convinced me that it was possible, and that I must, pursue a career in which I can leverage my love for science to enhance the lives of individuals from far less privileged backgrounds than myself. Your love and support over a decade now continually guide me as I work to build that career. Thank you for many lessons that I will never forget: your 'tough love', dreadful parent-teacher conferences, throwing my lab reports into the Indian Ocean! I love you very much, and no one keeps it real with me like you do. I can hear your laughter as I write all this!

There are two sets of mentors I would like to thank from my undergraduate years at Harvard.

Dr. Philip Kim and Dr. Andrew Y. Joe—my undergraduate research mentors. I would never have pursued a PhD in chemistry without the foundational opportunity you gave me.

Before I began scientific research, I took part in the "Mobile Technology Summer Program" of the Lakshmi Mittal and Family South Asia Institute at Harvard. The program was led by Dr. Tarun Khanna and Dr. Satchit Balsari. You gave me a critical lens and toolkit to understand how new technology makes its way into the lives of underprivileged individuals and makes a positive impact. Since then, your willingness to meet me and help me—whenever I either email out of the blue or our paths cross in Cambridge, Bombay, or elsewhere—has been invaluable. You have kept me connected to my long-term goals surrounding tackling energy poverty.

Before I began my PhD at Caltech, I spent just over one year as a State Bank of India Youth for India (SBI YFI) Fellow at Gram Vikas, an NGO in Odisha, India. Here, I was given the opportunity to establish India's first village-level microgrid to use Li-ion batteries, in a village of ≈300 people called Maligaon in Kalahandi district.

Liby Johnson, "Liby Sir" to me, and Ashutosh Bhat—my primary mentors while I was at Gram Vikas. I will forever be indebted to you for the trust you placed in me—an inexperienced recent college grad—to take on such an immense challenge. My experiences in Maligaon will always anchor my career, worldview, and resilience.

Ayushi Khandelwal and Vaani Khanna—my 'mentees', SBI YFI Fellows who came after me at Gram Vikas to promote electricity use in Maligaon beyond households for livelihood activities. Your efforts and hard work kept me tethered to Maligaon, giving me a sense of purpose and direction I could never find anywhere else. Thank you, Ayushi, for your visit to Pasadena as well.

Nandei Majhi, "Nani", and Dulhaba Odandra, "Dulhaba Sir"—my best friends in Odisha. Your love traverses language barriers, lack of telecommunications infrastructure, and gaps of months (sometimes up to a year) with no contact. I look forward most to seeing you when I visit Odisha/Maligaon.

The people of Maligaon. Your journey towards and in energy access—and your trust, kindness, and love—will always anchor me and my sense of purpose.

I have been very lucky to find many mentors and great friends at Caltech.

Dr. Brent Fultz and Dr. Pedro Guzman—thank you for all of your time and patience teaching me about Mössbauer spectrometry. This is the data set I'm most proud of.

Dr. Ryan G. Hadt, Dr. Karthish Manthiram, and Dr. Garnet Chan—my committee members—thank you for your many thoughtful questions, feedback, and encouragement.

Dr. Bruce S. Brunschwig—I have greatly enjoyed our discussions, and so appreciate (and am inspired by!) your sincere interest in my work and detailed feedback emails after my research talks.

Dr. Forrest A. L. Laskowski—I've never received better, more rigorous feedback on research proposals and application essays than yours.

Dr. Seong Shik Kim and Dr. Joshua J. Zak—you laid the foundation for our 'cathodes' subgroup and taught me how to collect beautiful synchrotron data.

Daniel B. McHaffie—your rigor inspires me, and it always made me smile to find you on our frequent 'night shifts' in lab.

Dr. Prithvi Akella—road trips with you (frequently spontaneous) to the Bay Area, Yosemite, and many fun gatherings you organized are some of my favorite memories.

My undergraduate mentees—Leah S. Soldner and Nayantara Ramakrishnan.

Leah, thank you for trusting me taking you on as my first undergraduate mentee. Working with you was a privilege and highlight of my PhD. I can never forget your commitment to our beam time at the Stanford Synchrotron Radiation Lightsource—persisting on (and succeeding in) fixing a frozen motor at 3 AM (when I was ready to call it quits)!

Nayantara, I have never been more excited by a cold email from a stranger than when you emailed me from the Indian Institute of Technology Bombay! You accomplished in one summer what I, and most advanced PhD students, could only accomplish in a year!

That Leah and Nayantara (albeit briefly) overlapped with each other during my PhD was a very lucky coincidence. You are both brilliant scientists, and I'm so proud and excited that you both are pursuing PhDs at the Massachusetts Institute of Technology (Leah) and Stanford University (Nayantara). I would be very lucky (and very much hope) to work with either or both of you again in the future!

The See Group—thank you to all members, past and present, for being so lovely to work with. Especially my cohort members: Dr. Brian C. Lee, Dr. Kim H. Pham, and Dr. Steven H. Stradley.

Dr. Michelle D. Qian—my last cohort member who I want to specifically acknowledge. Thank you for being like a sister to me. You have brainstormed and re-brainstormed paper outlines with me, uplifted me when I've felt discouraged, and frequently reminded me (by your example) of the importance of being kind. I feel blessed that my PhD has been in (nearly) lock-step with you, till the last weeks of our sixth year. You are a very talented scientist, and I was able to look up to your example every step of the way.

Dr. Zachery W. B. Iton—you are an incredible scientist, a patient *de facto* chauffeur, and my *de facto* brother. I could not imagine my PhD without your daily phone calls, endless banter, and wise counsel. Thank you for always lending your ear to anything I wish to discuss –from the absolutely nonsensical to the most serious topics. Your scientific creativity and grit inspired me and continue to inspire me. Thank you, perhaps above all, for all the laughs.

Lastly, I want to thank my family.

My Masi (aunt), Dr. Ranjana H. Advani, and Mausa (uncle) Pradeep Jotwani. From (quite literally) the day I was born, your home has always been my home too. Masi, thank you for all the delicious home-cooked food, being my go-to emergency contact, and all your love and affection—all amid your grueling work schedule and frequent travel. Pradeep Mausa, thank you for your deep and sincere interest in my work, being the first to edit every fellowship application essay I've ever written, and celebrating my victories! The past 6 years have not been without quite extreme disasters—the COVID-19 pandemic, the January 2025 Los Angeles wildfires, etc. Each time the sky has fallen, I have, without hesitation, ran to the safety of your home.

My cousins Anjali Jotwani, LtCol. Vishaal Hariprasad, Tara Jotwani, and Ankit Sud. You have opened up your homes to me at the drop of a hat, in sickness and in good health (and taken great care of me when it's been sickness).

My late grandparents: my Nani and Nana (maternal grandparents) Sarla and Hira Advani, and my Dadi and Dada (paternal grandparents) Fatema and Hatim Patheria. Padma Shivdasani—my 'Nani 2' (grandmother 2). Thank you all for your love, your legacy shapes who I am and everyone I love.

My mother, Roshan Patheria, and my father Salim Patheria. Thank you for everything—you are the wind beneath my wings, my greatest cheerleaders, and pillars of support.

My sister—Ameera Patheria. You are my best friend, my closest confidante, and the best parts of Mom and Dad combined into one.

My partner—Anukta Jain. You are my biggest blessing. I could not imagine what my time at Caltech would have been like without you, and I cannot imagine the rest of my life without you. I love you foreever.

Mom, Dad, Ameera, and Anukta—words cannot express my thanks to you all. I love you all so much. This thesis is for you.

ABSTRACT

This thesis develops a thermodynamic and electronic framework for Li-ion battery cathodes and applies it to a new class of high-capacity sulfides composed exclusively of industrially abundant elements. It introduces Li-rich $Li_{2+y}Al_yFe_{1-2y}S_2$ cathodes that leverage reversible multielectron anion redox, in which the formation and cleavage of S – S bonds enable especially high extents of charge storage. A core design framework is established linking delithiated-phase stability to accessible electrochemical redox capacity. The chemical space is expanded with Cu-substituted phases, $Li_{2.2-z}Cu_zAl_{0.2}Fe_{0.6}S_2$, in which unique Cu-S electronic interactions delocalize charge compensation beyond S – S bonds, thereby improving the reversibility of anion redox. These materials achieve high energy densities using only industrial elements, offering a promising foundation for next-generation Li-ion cathodes that address both performance and raw materials constraints. Thus, this thesis advances the long-term goal of building more sustainable energy systems and expanding access to electricity worldwide.

PUBLISHED CONTENT AND CONTRIBUTIONS

Iton, Z. W. B.; Kim, S. S.; Patheria, E. S.; Qian, M. D.; Ware, S. D.; See, K. A. Battery materials. *Comprehensive Inorganic Chemistry III* **2023**, 308–363.
E.S.P. wrote and edited part of this book chapter.

Li, X.; Kim, S. S.; Qian, M. D.; Patheria, E. S.; Andrews, J. L.; Morrell, C. T.; Melot, B.C.; See, K. A. Reducing Voltage Hysteresis Li-Rich Sulfide Cathodes by Incorporation of Mn. *Chem. Mater.* **2024**, *36*, 5687–5697.
E.S.P. collected data and proofread the manuscript.

Kim, S. S.; Kitchaev, D. A.; Patheria, E. S.; Morrell, C. T.; Qian, M. D.; Andrews, J. L.; Yan, Q.; Ko, S-T.; Luo, J.; Melot, B. C.; Van der Ven, A.; See, K. A. Cation Vacancies Enable Anion Redox in Li Cathodes. *J. Am. Chem. Soc.* **2024**, *146* (30), 20951–20962.
E.S.P. collected data and proofread the manuscript.

Qian, M. D.; Patheria, E. S.; Dulock, N. V.; Morrell, C. T.; See, K. A. Alkali-independent Anion Redox in $LiNaFeS_2$. *Chem. Mater.* **2024**, *36* (16), 7953–7966.
E.S.P. collected data and proofread the manuscript.

Patheria, E. S.; Guzman, P.; Soldner, L. S.; Qian, M. D.; Morrell, C. T.; Kim, S. S.; Hunady, K.; Priesen Reis, E. R.; Dulock, N. V.; Neilson, J. R.; Nelson Weker, J.; Fultz, B.; See, K. A. High-Energy Density Li-Ion Battery Cathode Using Only Industrial Elements. *J. Am. Chem. Soc.* **2025**, *147*, 9786–9799.
E.S.P. collected data and wrote the manuscript.

Patheria, E. S.; Iton, Z. W. B.; Laskowski, F. A. L.; See, K. A. Li-Ion Battery First Principles. *In preparation.*
E.S.P. wrote the manuscript.

Soldner, L. S.; Ramakrishnan, N. R.; Patheria, E. S.; Morrell, C. T.; Qian, M. D.; Davis, V. K.; See, K. A. $Cu^{>1+}$ Delocalizes Multielectron Redox and Determines Capacity Limits in Industrial Element Li-Ion Cathodes. *In preparation*.
E.S.P. collected data, and wrote and proofread the manuscript.

TABLE OF CONTENTS

Acknowledgements iii
Abstract viii
Published Content and Contributions ix
Table of Contents ix
List of Illustrations xii
List of Tables xxix
Chapter I: Introduction—Li-Ion Battery First Principles 1
Abstract 2
1.1 Introduction 3
1.2 The Li-ion battery model system 6
1.3 Thesis outline 15
Bibliography 17
Chapter II: Multielectron Redox Mechanism in $Li_{2+y}Al_yFe_{1-2y}S_2$ Cathodes . 18
Abstract 19
2.1 Introduction 20
2.2 Results and discussion 22
2.3 Conclusion 28
2.4 Experimental 28
2.5 Funding and user-facility acknowledgments 33
Bibliography 35
Chapter III: Capacity Limit Determinants of $Li_{2+y}Al_yFe_{1-2y}S_2$ Cathodes . . . 39
Abstract 40
3.1 Introduction 41
3.2 Results and discussion 41
3.3 Conclusion 47
3.4 Experimental 48
3.5 Funding and user-facility acknowledgments 51
Bibliography 52
Chapter IV: $Cu^{>1+}$ Delocalizes Multielectron Redox and Determines Capacity Limits in $Li_{2.2-z}Cu_zAl_{0.2}Fe_{0.6}S_2$ Cathodes 54
Abstract 55
4.1 Introduction 56
4.2 Results and discussion 58
4.3 Conclusion 73
4.4 Experimental 74
4.5 Funding and user-facility acknowledgments 81
Bibliography 83
Chapter V: Conclusion and Outlook for Multielectron Redox Industrial-Element Li-Ion Cathodes 88

Bibliography 91
Supplementary Information–Chapters 2 and 3
Bibliography
Supplementary Information–Chapter 4
Bibliography

LIST OF ILLUSTRATIONS

Number *Page*

1.1 All batteries contain an anode, electrolyte, and cathode. An electrolyte-permeable, electronically-insulating separator between the anode and cathode prevents electrical contact between the electrodes. The electrolyte is electronically insulating and ionically conducting. In the schematics, electrons are indicated as e^-, the anode material as j, and the cathode material as i. The solvated ions in the electrolyte are indicated as + and −. (a) During discharge, j is oxidized to j^+ at the anode, and i^+ is reduced to i at the cathode. Discharge is spontaneous. (b) During charge, j^+ is reduced to j, and i is oxidized to i^+. The names of the two electrodes, anode vs. cathode, are defined for the spontaneous reaction. Charging the battery requires an applied voltage across the cell. For both charge and discharge the direction of e^- and current I flow through the external circuit is indicated. . . 4

1.2 Example schematic showing the state of relevant electrochemical potentials for the cell components before assembly and at open-circuit equilibrium. (a) The pre-assembly diagram illustrates that the electrochemical potentials are located at higher energies in the anode than in the cathode. (b) The equilibrium diagram shows how the electrochemical potentials move in response to the electrostatic potential drop formed at each interface. The electrostatic potential drop forms because of the reactions shown in the insets, which produce or consume local Li^+-e^- pairs. A mismatch in the $\bar{\mu}^{\alpha}_{Li^+}$ levels across either interface is a driving force for the associated interfacial reaction; the reaction will proceed until the consequent electrostatic potential drop negates the difference in chemical potential across the interface, yielding a flat electrochemical potential profile. The measured OCV at equilibrium is given by the difference in the electrochemical potentials for the electrons. Note that because of the sign difference, the interfacial electric fields act in opposite manner on the electrochemical potentials for Li^+ vs. e^-. 9

1.3 (a) During discharge, the external circuit allows electrons to move directly from the anode to cathode. The electrostatic potential drop at the anode|electrolyte interface diminishes as electrons are removed, which pushes $\bar{\mu}^{\text{anode}}_{\text{Li}^+}$ to higher energies. Similarly, electrons arriving at the cathode diminish the electrostatic potential drop at the electrolyte|cathode interface, which pushes $\bar{\mu}^{\text{cathode}}_{\text{Li}^+}$ to lower energies. Li^+ flows from left to right across the interfaces, giving rise to a concentration gradient (visualized here by the slight slope in the electrochemical potentials). (b) During charge, an external device imposes an external voltage more positive than the OCV onto the cell. The applied voltage is achieved via increases in the interfacial electrostatic potential drops. Relative to $\bar{\mu}^{\text{electrolyte}}_{\text{Li}^+}$, the anode and cathode's $\bar{\mu}^{\alpha}_{\text{Li}^+}$ move to energies more negative and positive, respectively. Li^+ flows from right to left across the interfaces, giving rise to concentration gradients. 13

2.1 The crystal structure of (a) Li_2FeS_2 projected along the c-axis (top) and b-axis (bottom), and the crystal structure of (b) Li_5AlS_4 projected along the c-axis (top) and b-axis (bottom). In each panel, the solid black line indicates the unit cell of the structure shown, while the dashed black line indicates the unit cell of the other structure for comparison. 21

2.2 Synchrotron powder X-ray diffraction of (a) Li_2FeS_2, (b) $Li_{2.2}Al_{0.2}Fe_{0.6}S_2$, and (c) $Li_{2.4}Al_{0.4}Fe_{0.2}S_2$. The corresponding Rietveld refinement, reflection locations in Q (Å^{-1}) of each phase in the fit, and difference between fit and data are shown for each material. Superstructure reflections that are not fit by the Rietveld refinement are indicated by asterisks (*). The resulting lattice parameters (d) a, (e) b, and (f) c from each Rietveld refinement with respect to y in $Li_{2+y}Al_yFe_{1-2y}S_2$ with linear fits indicated by dashed lines. The lattice parameters follow a linear Vegard's trend, indicating that yLi^+ and yAl^{3+} successfully substitute for $2yFe^{2+}$ in $Li_{2.2}Al_{0.2}Fe_{0.6}S_2$ ($y = 0.2$) and $Li_{2.4}Al_{0.4}Fe_{0.2}S_2$ ($y = 0.4$). 23

2.3 First cycle galvanostatic charge and discharge curves of (a) Li_2FeS_2, (b) $Li_{2.2}Al_{0.2}Fe_{0.6}S_2$, and (c) $Li_{2.4}Al_{0.4}Fe_{0.2}S_2$ cycled at $C/10$ based on 1 e^- per formula unit. The dashed line across panels (a), (b), and (c) indicates the linear trend in Fe oxidation capacity with y. (d) The equilibrium voltage $V_{eq.}$ and (e) overpotential η during the first charge extracted from GITT. (f) The cycling of Li_2FeS_2 and $Li_{2.2}Al_{0.2}Fe_{0.6}S_2$ at $C/10$. (g) Rate capability tests of Li_2FeS_2 and $Li_{2.2}Al_{0.2}Fe_{0.6}S_2$ for 5 cycles each at $C/10$, $C/5$, $C/2$, 1C, and again at $C/10$. All C rates are based on 1 e^- per formula unit. The data points in (f) and (g) are the average of three replicate cells and error bars indicate the standard deviations. 24

2.4 *Ex-situ* Fe K-edge XAS spectra of (a) Li_2FeS_2 and (b) $Li_{2.2}Al_{0.2}Fe_{0.6}S_2$. The first derivative of the rising edge regions for (c) Li_2FeS_2 and (d) $Li_{2.2}Al_{0.2}Fe_{0.6}S_2$. The energies of the maxima of the first derivatives at each of the SOCs are overlaid with the corresponding galvanostatic cycling data for (e) Li_2FeS_2 and (f) $Li_{2.2}Al_{0.2}Fe_{0.6}S_2$. The dashed lines in all panels indicate the approximate positions of the pre-edge x, at 7113.0 eV, and the two rising edges observed at different SOCs, y and z, at 7117.2 eV and 7118.2 eV, respectively. 26

2.5 (a) *Ex-situ* S K-edge XAS and (b) a representative first cycle curve indicating the SOCs at which the XAS data was collected for Li_2FeS_2. The corresponding data for $Li_{2.2}Al_{0.2}Fe_{0.6}S_2$ are in (c) and (d), respectively. The dashed lines in (a) and (c) indicate the two pre-edge features v and w, at 2469.2 eV and 2471.8 eV, respectively. 27

3.1 (a) Charge curves of Li_2FeS_2 up to the transition point, after which the cell is stopped, disassembled, the cathode is rinsed in DMC, dried in vacuum, annealed at 200 °C under static vacuum (≈50 mTorr) for 2 hours, or rested under the same vacuum conditions for ≈1 week, and then assembled in a new cell for galvanostatic cycling. The standard galvanostatic cycling charge curve for uninterrupted cycling is indicated by the black, dashed line in panel (a). (b) *Ex-situ* XRD of Li_2FeS_2 focused on the 2θ ranges for the (0 0 1) reflection, and the (2 0 0) reflection of pyrite FeS_2 in the pristine, transition, and annealed states. (c) S K-edge XAS spectra of Li_2FeS_2 in the pristine, transition, and annealed states. As before in Figure 2.5, the dashed lines in panel (c) indicate the two pre-edge features v and w, at 2469.2 eV and 2471.8 eV, respectively. Panels (d), (e), and (f), respectively, indicate the same corresponding data for $Li_{2.2}Al_{0.2}Fe_{0.6}S_2$. 42

3.2 (a) The weighted averages and corresponding weighted standard deviations of the isomer shifts of the four Lorentzian doublets used to fit *ex-situ* Mössbauer spectra of Li_2FeS_2 at various SOCs. (b) The coordination number N of the first shell correlations, representing the average number of nearest S atoms coordinating Fe, extracted from EXAFS fits for Li_2FeS_2 at various SOCs. (c) The representative galvanostatic data showing the SOC for each data point. Panels (d), (e), and (f) indicate the same corresponding data, respectively, for $Li_{2.2}Al_{0.2}Fe_{0.6}S_2$. In panels (a) and (d), the weighted average is indicated by the symbol, and the weighted standard deviation is indicated by height of the box accompanying the symbol. The dotted/dashed dark purple horizontal line in panels (a) and (d) indicates the weighted average isomer shift at the transition SOC. 45

4.1 The crystal structures of (a) Li_2FeS_2 projected along the c-axis (top) and b-axis (bottom), (b) Li_5AlS_4 projected along the c-axis (top) and b-axis (bottom), and (c) $LiCuFeS_2$ projected along the c-axis (top) and b-axis (bottom). In each panel, the solid black line indicates the unit cell of the structure shown. 56

4.2 Synchrotron powder X-ray diffraction of (a) $Li_{2.2}Al_{0.2}Fe_{0.6}S_2$, (b) $Li_2Cu_{0.2}Al_{0.2}Fe_{0.6}S_2$, and (c) $Li_{1.8}Cu_{0.4}Al_{0.2}Fe_{0.6}S_2$. The corresponding Rietveld refinement, reflection locations in Q (Å^{-1}) of each phase in the fit, and difference between fit and data are shown for each material. Superstructure reflections that are not fit by the Rietveld refinement are indicated by asterisks (*). The resulting lattice parameters (d) a, (e) b, and (f) c from each Rietveld refinement with respect to z in $Li_{2.2-z}Cu_zAl_{0.2}Fe_{0.6}S_2$ with linear fits indicated by dashed lines. The lattice parameters mostly follow a linear Vegard's trend, indicating that Cu^+ successfully substitutes for Li^+ in $Li_2Cu_{0.2}Al_{0.2}Fe_{0.6}S_2$ ($z = 0.2$) and $Li_{1.8}Cu_{0.4}Al_{0.2}Fe_{0.6}S_2$ ($z = 0.4$). . 59

4.3 First cycle galvanostatic charge and discharge curves of (a) $Li_{2.2}Al_{0.2}Fe_{0.6}S_2$, (b) $Li_2Cu_{0.2}Al_{0.2}Fe_{0.6}S_2$, and (c) $Li_{1.8}Cu_{0.4}Al_{0.2}Fe_{0.6}S_2$ cycled at $C/10$ based on 1 e^- per formula unit. The dashed line across panels (a), (b), and (c) indicates the linear trend in capacity with z. (d) The cycling of $Li_{2.2}Al_{0.2}Fe_{0.6}S_2$, $Li_2Cu_{0.2}Al_{0.2}Fe_{0.6}S_2$, and $Li_{1.8}Cu_{0.4}Al_{0.2}Fe_{0.6}S_2$ at $C/10$. (e) Rate capability tests of $Li_{2.2}Al_{0.2}Fe_{0.6}S_2$, $Li_2Cu_{0.2}Al_{0.2}Fe_{0.6}S_2$, and $Li_{1.8}Cu_{0.4}Al_{0.2}Fe_{0.6}S_2$ for 5 cycles each at $C/10$, $C/5$, $C/2$, 1C, and again at $C/10$. All C rates are based on 1 e^- per formula unit. The data points in (d) and (e) are the average of three replicate cells and error bars indicate the standard deviations. (f) The equilibrium voltage $V_{eq.}$ and (g) overpotential η during the first charge extracted from GITT. 61

4.4 *Ex-situ* Fe K-edge XAS spectra of (a) $Li_{2.2}Al_{0.2}Fe_{0.6}S_2$ and (b) $Li_{1.8}Cu_{0.4}Al_{0.2}Fe_{0.6}S_2$. The first derivative of the rising edge regions for (c) $Li_{2.2}Al_{0.2}Fe_{0.6}S_2$ and (d) $Li_{1.8}Cu_{0.4}Al_{0.2}Fe_{0.6}S_2$. The energies of the maxima of the first derivatives at each of the SOCs are overlaid with the corresponding galvanostatic cycling data for (e) $Li_{2.2}Al_{0.2}Fe_{0.6}S_2$ and (f) $Li_{1.8}Cu_{0.4}Al_{0.2}Fe_{0.6}S_2$. The dashed lines in all panels indicate the approximate positions of the pre-edge w, at 7113.0 eV, the two rising edges observed at different SOCs, x and y, at 7117.2 eV and 7118.2 eV, respectively, and the additional high energy feature, z, at 7119.7 eV. 63

4.5 (a) *Ex-situ* S K-edge XAS and (b) a representative first cycle curve indicating the SOCs at which the XAS data was collected for $Li_{2.2}Al_{0.2}Fe_{0.6}S_2$. The corresponding data for $Li_{1.8}Cu_{0.4}Al_{0.2}Fe_{0.6}S_2$ are in (c) and (d), respectively. The dashed lines in (a) and (c) indicate the two pre-edge features u and v, at 2469.2 eV and 2471.8 eV, respectively. 65

4.6 (a) *Ex-situ* Cu K-edge XAS spectra, (b) magnified pre-edge region, and (c) first derivative of the rising edge regions for $Li_{1.8}Cu_{0.4}Al_{0.2}Fe_{0.6}S_2$. (d) The energies of the maxima of the first derivatives at each of the SOCs are overlaid with representative galvanostatic cycling data. The dashed lines in all panels indicate the approximate positions of the pre-edge r, at 8979.0 eV, and the lowest and highest energy rising edge positions observed at different SOCs, s and t, at 8981.9 eV and 8982.4 eV, respectively. 66

4.7 The first shell values of (a) $r_{\text{eff.}}$ and (b) N from Fe K-edge EXAFS analysis of $Li_{2.2}Al_{0.2}Fe_{0.6}S_2$, with (c) accompanying galvanostatic data indicating the SOCs at which EXAFS analysis is conducted. Panels (d), (e), and (f), respectively, indicate the same corresponding data for $Li_{1.8}Cu_{0.4}Al_{0.2}Fe_{0.6}S_2$. Panels (d) and (e) additionally include $r_{\text{eff.}}$ and N, respectively, from Cu K-edge EXAFS analysis of $Li_{1.8}Cu_{0.4}Al_{0.2}Fe_{0.6}S_2$. All $r_{\text{eff.}}$ and N values are shown with statistical error bars. Fe K-edge EXAFS data points are marked with solid red circles, while Cu K-edge EXAFS data points are marked with dashed cyan circles. 67

4.8 (a) Charge curves of $Li_{2.2}Al_{0.2}Fe_{0.6}S_2$ up to the transition point, after which the cell is stopped, disassembled, the cathode is rinsed in DMC, dried in vacuum, annealed at 200 °C under static vacuum (≈50 mTorr) for 2 hours, or rested at room temperature under the same vacuum conditions for ≈36 hours, and then assembled in a new cell for galvanostatic cycling. The standard galvanostatic cycling charge curve for uninterrupted cycling is indicated by the black, dashed line in panel (a). (b) *Ex-situ* XRD of $Li_{2.2}Al_{0.2}Fe_{0.6}S_2$ focused on the 2θ ranges of the (0 0 1) reflection, and the (2 0 0) reflection of pyrite FeS_2 in the pristine, transition, and annealed states. (c) Fe K-edge XAS spectra, (d) magnified pre-edge region, and (e) first derivative of the rising edge regions for $Li_{2.2}Al_{0.2}Fe_{0.6}S_2$ in the pristine, transition, and annealed states. As before in Figure 4.4, the dashed lines in panels (c), (d), and (e) indicate the approximate positions of the pre-edge w, at 7113.0 eV, and the two rising edges observed at different SOCs, x and y, at 7117.2 eV and 7118.2 eV, respectively. Panels (f), (g), (h), (i), and (j) contain the same corresponding data for $Li_{1.8}Cu_{0.4}Al_{0.2}Fe_{0.6}S_2$. Panel (g) focuses on the 2θ ranges of the (0 0 1) reflection of $Li_{1.8}Cu_{0.4}Al_{0.2}Fe_{0.6}S_2$ and the (2 0 4) reflection of chalcopyrite $CuFeS_2$. The dashed lines in panels (h), (i), and (j) indicate the approximate positions of the pre-edge w, at 7113.0 eV, and the two rising edges observed at different SOCs, x' and y', at 7118.5 eV and 7119.7 eV, respectively. 70

5.1 Indexed prices of Li-ion (a) key cathode raw materials and (b) battery packs from 2017 to 2024. All prices are normalized to July 2017. The spike in raw material costs in 2022 caused Li-ion pack prices to increase for the first time ever that same year, marked by the dashed gray lines. 89

S2 The refined phases (top) and only anion frameworks (bottom) of (a) Li_2FeS_2, (b) $Li_{2.2}Al_{0.2}Fe_{0.6}S_2$, (c) $Li_{2.4}Al_{0.4}Fe_{0.2}S_2$, from our sXRD data, and (d) Li_5AlS_4. The axes in (a) apply to all panels. The anion framework of Li_2FeS_2 has near perfect HCP symmetry. To easily observe changes to the anion framework with y in $Li_{2+y}Al_yFe_{1-2y}S_2$, we superimpose the S atoms in Li_2FeS_2, as transparent black circles, on top of the S atoms in $Li_{2.2}Al_{0.2}Fe_{0.6}S_2$, $Li_{2.4}Al_{0.4}Fe_{0.2}S_2$, and Li_5AlS_4. Qualitatively, the anion frameworks become more distorted from HCP symmetry with larger y. We hypothesize that the high charge density of Al^{3+} causes the distortions. 99

S3 The first cycles of three replicate cells from three separate reaction batches of (a) Li_2FeS_2, (b) $Li_{2.2}Al_{0.2}Fe_{0.6}S_2$, and (c) $Li_{2.4}Al_{0.4}Fe_{0.2}S_2$, all cycled at $C/10$ based on 1 e^- per formula unit. We mark the transition point from the sloping region associated with Fe oxidation to the S oxidation plateau during charge for each replicate with a dashed vertical gray line. The corresponding average capacity and standard deviations associated with the two regions are in Table S4. 99

S4 GITT curve and accompanying galvanostatic curve at $C/10$ of the first cycle of (a) Li_2FeS_2, and three representative time-relaxation profiles from the (b) Fe oxidation sloping region and (c) S oxidation plateau. Panels (d), (e), and (f) show the same corresponding data for $Li_{2.2}Al_{0.2}Fe_{0.6}S_2$, and panels (g), (h), and (i) show the same corresponding data for $Li_{2.4}Al_{0.4}Fe_{0.2}S_2$. GITT was obtained at $C/10$ based on 1 mole e^- per f.u. for 20 min separated by 4 h rest periods at open-circuit. The sections of the GITT curves for which the time-relaxation profiles are plotted are marked in panels (a), (d), and (g). Black dashed lines and circular data points mark the section limits of the sloping region, also used in panels (b), (e), and (h). Gray dashed lines and diamond-shaped data points mark the limits for the plateau, again used in panels (c), (f), and (i). 100

S5 (a) The gravimetric charge and discharge capacities and (b) the coulombic efficiencies of three replicate cells of Li_2FeS_2 cycled at $C/10$ based on 1 mole e^- per f.u. for 25 cycles. Panels (c) and (d) show the same corresponding data for $Li_{2.2}Al_{0.2}Fe_{0.6}S_2$. The average and standard deviation of the three replicates in (a) and (c) are shown in Figure 2.3f in the main text. 101

S6 Representative galvanostatic cycles 1, 5, 10, and 25 of (a) Li_2FeS_2 and (b) $Li_{2.2}Al_{0.2}Fe_{0.6}S_2$, both cycled at $C/10$ based on 1 mole e^- per formula unit. 101

S7 The gravimetric charge and discharge capacities of three replicate cells of (a) Li_2FeS_2 and (b) $Li_{2.2}Al_{0.2}Fe_{0.6}S_2$ subjected to rate capability tests of 5 cycles each at $C/10$, $C/5$, $C/2$, 1C, and again at $C/10$. All C rates are based on 1 e^- per formula unit. The average and standard deviation of these replicates are shown in Figure 2.3g in the main text. 102

S8 Representative galvanostatic cycles 1 (at $C/10$), 5 (at $C/10$), 10 (at $C/5$), 15 (at $C/2$), 20 (at $1C$), and 25 (again at $C/10$) of (a) Li_2FeS_2 and (b) $Li_{2.2}Al_{0.2}Fe_{0.6}S_2$ from the rate capability tests shown in Figure S7. All C rates are based on 1 mole e^- per formula unit. 102

S9 *Ex-situ* Fe K-edge XAS spectra of (a) Li_2FeS_2 and (b) $Li_{2.2}Al_{0.2}Fe_{0.6}S_2$ at the pristine, mid-slope, transition, annealed, and mid-plateau SOCs. The first derivative of the rising edge regions for (c) Li_2FeS_2 and (d) $Li_{2.2}Al_{0.2}Fe_{0.6}S_2$. The energies of the maxima of the first derivatives at each of the SOCs are overlaid with the corresponding galvanostatic cycling data for (e) Li_2FeS_2 and (f) $Li_{2.2}Al_{0.2}Fe_{0.6}S_2$. The dashed lines in all panels labeled x, y, and z indicate the same features as in Figure 2.4: the pre-edge x, at 7113.0 eV, and the two rising edges observed at different SOCs, y and z, at 7117.2 eV and 7118.2 eV, respectively. 105

S10 *Ex-situ* XRD, focused on the (0 0 1) reflection between ≈13° to 16° 2θ, of (a) Li_2FeS_2 in the pristine, transition, charged, and discharged states with (b) accompanying galvanostatic data. The same corresponding data for $Li_{2.2}Al_{0.2}Fe_{0.6}S_2$ is shown in panels (c) and (d), respectively. 107

S11 Full *ex-situ* XRD patterns between 10 to 85 2θ (°) of (a) Li_2FeS_2 in the pristine, transition, charged, and discharged states with (b) accompanying galvanostatic data. The same corresponding data for $Li_{2.2}Al_{0.2}Fe_{0.6}S_2$ is shown in panels (c) and (d), respectively. Figure S10 suggests that long-range order is restored in the discharged state by showing the recovery of the layer spacing associated with the (0 0 1) reflection. The near-identical full XRD patterns in the pristine and discharged states shown here confirm that this structural restoration extends to the entire long-range order, not just the layer spacing. 107

S12 XRD of the attempted synthesis of $Al_{0.2}Fe_{0.6}S_2$. The Rietveld refinement (fit), reflection locations of each phase in the fit, the weight percent contribution of each phase, and the difference between the fit and data are all shown. All observed reflections are accounted for by a three phase fit to Fe_7S_8 (10.6 wt%), Al_2FeS_4 (38.3 wt%), and FeS_2 (51.1 wt%). 109

S13 The crystal structure of (a) $Li_{2.2}Al_{0.2}Fe_{0.6}S_2$ from Rietveld refinement of the sXRD data in Figure 2.2 projected along the *a*-axis (top) and *c*-axis (bottom), and the crystal structure of (b) Al_2FeS_4 projected along the *a*-*c* plane (top) and *c*-axis (bottom). To show how the structures are related, the unit cell of the material being shown is indicated with a solid, black line, and the unit cell of the other material is indicated with a dashed, black line. The Li^+-only layers perpendicular to the *c*-axis in $Li_{2.2}Al_{0.2}Fe_{0.6}S_2$ contain octahedrally coordinated Li^+, while the corresponding layers in Al_2FeS_4 have only tetrahedrally coordinated Fe^{2+} or Al^{3+}. To easily compare tetrahedral sites, we omit all octahedrally coordinated cations in the bottom projections along the *c*-axis for both materials. This further highlights the possible structural similarity between delithiated $Li_{2.2}Al_{0.2}Fe_{0.6}S_2$ and Al_2FeS_4. 109

S14 *Ex-situ* XRD of the annealed states of (a) Li_2FeS_2 and (b) $Li_{2.2}Al_{0.2}Fe_{0.6}S_2$, and the transition states of (c) Li_2FeS_2 and (d) $Li_{2.2}Al_{0.2}Fe_{0.6}S_2$. Each panel shows the Rietveld refinement (fit), reflection locations of each phase in the fit, and the difference between the fit and data. All patterns are described by a single phase, except Li_2FeS_2 in the annealed state, which is fit to two phases: pyrite FeS_2 (16.8 wt%), and $Li_{2-x}FeS_2$ (83.2 wt%). While we label the phases in the fits as Li_{2-x} in (a) and (c) or $Li_{2.2-x}$ in (b) and (d) to indicate delithiated samples, the crystallographic information files used for the refinements are those of pristine (fully lithiated) Li_2FeS_2 and $Li_{2.2}Al_{0.2}Fe_{0.6}S_2$. . . . 110

S15 The weighted averages and corresponding weighted standard deviations of the isomer shifts (a) and quadrupole splittings (b) of the Lorentzian doublets used to fit *ex-situ* Mössbauer spectra of Li_2FeS_2, with the corresponding galvanostatic data (c) showing the SOCs at which the spectra are measured. Panels (d), (e), and (f), respectively, indicate the same corresponding data for $Li_{2.2}Al_{0.2}Fe_{0.6}S_2$. In panels (a), (b), (d), and (e), the weighted average is indicated by the symbol, and the weighted standard deviation is indicated by height of the box accompanying the symbol. The dotted/dashed dark purple horizontal line in panels (a) and (d) indicates the weighted average isomer shift at the transition SOC. The isomer shift data is discussed in the main text. The quadrupole splitting is similar in both materials. After annealing, the quadrupole splitting broadens for Li_2FeS_2 but narrows for $Li_{2.2}Al_{0.2}Fe_{0.6}S_2$, supporting that the former undergoes conversion while the latter does not. 111

S16 Mössbauer spectrum, four Fe sites in each fit, fit (sum of the Fe sites), and fit-data difference (Δ) of the (a) pristine, (b) mid-slope, (c) transition, (d) mid-plateau, (e) charged, (f) discharged, and (g) annealed states of Li_2FeS_2. The linewidth (Γ) of the four Fe sites is constrained to be equal in each fit and is shown in each panel. A single unidentified Fe site (peak) in annealed sample is indicated by an asterisk. 112

S17 Mössbauer spectrum, four Fe sites in each fit, fit (sum of the Fe sites), and fit-data difference (Δ) of the (a) pristine, (b) mid-slope, (c) transition, (d) mid-plateau, (e) charged, (f) discharged, and (g) annealed states of $Li_{2.2}Al_{0.2}Fe_{0.6}S_2$. The linewidth ($\Gamma$) of the four Fe sites is constrained to be equal in each fit and is shown in each panel. 113

S18 The first and second shell values of (a) $r_{\text{eff.}}$ and (b) N for Li_2FeS_2, with accompanying galvanostatic data (c) indicating the SOCs at which the EXAFS analysis is conducted. Panels (d), (e), and (f), respectively, indicate the same corresponding data for $Li_{2.2}Al_{0.2}Fe_{0.6}S_2$. All $r_{\text{eff.}}$ and N values are shown with statistical error bars. The first shell data is discussed in the main text. The second shell data shows similar trends for Li_2FeS_2 and $Li_{2.2}Al_{0.2}Fe_{0.6}S_2$. 116

S19 Fe K-edge EXAFS $k^3\chi(k)$ data, fit, fit window, and fit-data difference of the (a) pristine, (b) mid-slope, (c) transition, (d) mid-plateau, (e) charged, (f) discharged, and (g) annealed states of Li_2FeS_2. 117

S20 Fe K-edge EXAFS $k^3\chi(k)$ data, fit, fit window, and fit-data difference of the (a) pristine, (b) mid-slope, (c) transition, (d) mid-plateau, (e) charged, (f) discharged, and (g) annealed states of $Li_{2.2}Al_{0.2}Fe_{0.6}S_2$. . 118

S21 Fe K-edge EXAFS k^3-weighted $|\chi(R)|$ data, fit, fit window, and fit-data difference of the (a) pristine, (b) mid-slope, (c) transition, (d) mid-plateau, (e) charged, (f) discharged, and (g) annealed states of Li_2FeS_2. 119

S22 Fe K-edge EXAFS k^3-weighted $|\chi(R)|$ data, fit, fit window, and fit-data difference of the (a) pristine, (b) mid-slope, (c) transition, (d) mid-plateau, (e) charged, (f) discharged, and (g) annealed states of $Li_{2.2}Al_{0.2}Fe_{0.6}S_2$. 120

S23 The centroids of the Mössbauer spectra, the weighted averages and weighted standard deviations of the isomer shifts of Li_2FeS_2 (a), with accompanying galvanostatic data (b). Panels (c) and (d) respectively show the same corresponding data for $Li_{2.2}Al_{0.2}Fe_{0.6}S_2$. We calculate the centroids of the spectra in Figures S16 and S17 as centroid = $\frac{\sum_i I(v_i)\cdot v_i}{\sum_i I(v_i)}$ where $I(v_i)$ is the normalized absorption intensity, v_i is the velocity, and i indexes the data points. The dotted/dashed dark purple horizontal line in panels (a) and (c) indicates the centroid at the transition SOC. The centroids, calculated directly from the data without parameters, provide direct access to the isomer shift. They follow the same trend as the weighted average isomer shifts from our fits, confirming that the fits accurately represent the data and are unbiased. The annealed state of Li_2FeS_2 is omitted because it contains multiple phases, preventing meaningful spectral centroid analysis. 123

S24 The volumetric energy density versus the gravimetric energy density for commercial Li-ion battery cathodes NMC811 and LFP, and the emerging cathodes DRX, Li_2FeS_2, and $Li_{2.2}Al_{0.2}Fe_{0.6}S_2$. Among these materials, $Li_{2.2}Al_{0.2}Fe_{0.6}S_2$ exhibits the highest gravimetric energy density. Relevant values and references for determining the gravimetric and volumetric energy densities are provided in Table S9. 125

S25 The first cycles of three replicate cells from three separate cells of (a) $Li_{2.2}Al_{0.2}Fe_{0.6}S_2$, (b) $Li_2Cu_{0.2}Al_{0.2}Fe_{0.6}S_2$, and (c) $Li_{1.8}Cu_{0.4}Al_{0.2}Fe_{0.6}S_2$, all cycled at $C/10$ based on 1 e^- per formula unit. We mark the transition point from the sloping region associated with Fe oxidation to the S oxidation plateau during charge for each replicate with a dashed vertical gray line. The corresponding average capacity and standard deviations associated with the two regions are in Table S11. 134

S26 (a) The gravimetric charge and discharge capacities and (b) the coulombic efficiencies of three replicate cells of $Li_{2.2}Al_{0.2}Fe_{0.6}S_2$ cycled at $C/10$ based on 1 mole e^- per f.u. for 25 cycles. Panels (c) and (d), and (e) and (f) show the same corresponding data for $Li_2Cu_{0.2}Al_{0.2}Fe_{0.6}S_2$ and $Li_{1.8}Cu_{0.4}Al_{0.2}Fe_{0.6}S_2$, respectively. The average and standard deviation of the three replicates in (a) and (c) are shown in Figure 4.3d in the main text. 135

S27 Representative galvanostatic cycles 1, 5, 10, and 25 of (a) $Li_{2.2}Al_{0.2}Fe_{0.6}S_2$, (b) $Li_2Cu_{0.2}Al_{0.2}Fe_{0.6}S_2$, and (c) $Li_{1.8}Cu_{0.4}Al_{0.2}Fe_{0.6}S_2$, all cycled at $C/10$ based on 1 mole e^- per formula unit. 135

S28 The gravimetric charge and discharge capacities of three replicate cells of (a) $Li_{2.2}Al_{0.2}Fe_{0.6}S_2$, (b) $Li_2Cu_{0.2}Al_{0.2}Fe_{0.6}S_2$, and (c) $Li_{1.8}Cu_{0.4}Al_{0.2}Fe_{0.6}S_2$ subjected to rate capability tests of 5 cycles each at $C/10$, $C/5$, $C/2$, 1C, and again at $C/10$. All C rates are based on 1 e^- per formula unit. The average and standard deviation of these replicates are shown in Figure 4.3e in the main text. 136

S29 Representative galvanostatic cycles 1 (at $C/10$), 5 (at $C/10$), 10 (at $C/5$), 15 (at $C/2$), 20 (at $1C$), and 25 (again at $C/10$) of (a) $Li_{2.2}Al_{0.2}Fe_{0.6}S_2$, (b) $Li_2Cu_{0.2}Al_{0.2}Fe_{0.6}S_2$, and (c) $Li_{1.8}Cu_{0.4}Al_{0.2}Fe_{0.6}S_2$ from the rate capability tests shown in Figure S28. All C rates are based on 1 mole e^- per formula unit. 136

S30 GITT curve and accompanying galvanostatic curve at $C/10$ of the first cycle of (a) $Li_{2.2}Al_{0.2}Fe_{0.6}S_2$, (b) $Li_2Cu_{0.2}Al_{0.2}Fe_{0.6}S_2$, and (c) $Li_{1.8}Cu_{0.4}Al_{0.2}Fe_{0.6}S_2$. GITT was obtained at $C/10$ based on 1 mole e^- per f.u. for 20 min separated by 4 h rest periods at open-circuit. . 138

S31 (a) *Ex-situ* Fe K-edge XAS spectra and (b) first derivative of the rising edge for $Li_2Cu_{0.2}Al_{0.2}Fe_{0.6}S_2$. (c) The energies of the maxima of the first derivatives at each of the SOCs overlaid with the corresponding galvanostatic cycling data. The dashed lines in all panels indicate the approximate positions of the pre-edge w, at 7113.0 eV, the two rising edges observed at different SOCs, x and y, at 7117.2 eV and 7118.2 eV, respectively, and the additional high energy feature, z, at 7119.7 eV. 138

S32 (a) *Ex-situ* S K-edge XAS and (b) a representative first cycle curve indicating the SOCs at which the XAS data was collected for $Li_2Cu_{0.2}Al_{0.2}Fe_{0.6}S_2$. The dashed lines in (a) indicate the two pre-edge features u and v, at 2469.2 eV and 2471.8 eV, respectively. 139

S33 *Ex-situ* XRD, focused on the (0 0 1) reflection between ≈13° to 16° 2θ, of (a) $Li_{2.2}Al_{0.2}Fe_{0.6}S_2$ in the pristine, transition, charged, and discharged states with (b) accompanying galvanostatic data. The same corresponding data for $Li_2Cu_{0.2}Al_{0.2}Fe_{0.6}S_2$ and $Li_{1.8}Cu_{0.4}Al_{0.2}Fe_{0.6}S_2$ is shown in panels (c) and (d), and (e) and (f), respectively. 139

S34 Full *ex-situ* XRD patterns between 10 to 85 2θ (°) of (a) $Li_{2.2}Al_{0.2}Fe_{0.6}S_2$ in the pristine, transition, charged, and discharged states with (b) accompanying galvanostatic data. The same corresponding data for $Li_2Cu_{0.2}Al_{0.2}Fe_{0.6}S_2$ and $Li_{1.8}Cu_{0.4}Al_{0.2}Fe_{0.6}S_2$ is shown in panels (c) and (d), and (e) and (f), respectively. Figure S33 suggests that long-range order is restored in the discharged state by showing the recovery of the layer spacing associated with the (0 0 1) reflection. The near-identical full XRD patterns in the pristine and discharged states shown here confirm that this structural restoration extends to the entire long-range order, not just the layer spacing. 140

S35 (a) *Ex-situ* Cu K-edge XAS spectra, (b) magnified pre-edge region, and (c) first derivative of the rising edge regions for $Li_2Cu_{0.2}Al_{0.2}Fe_{0.6}S_2$. (d) The energies of the maxima of the first derivatives at each of the SOCs are overlaid with representative galvanostatic cycling data. The dashed lines in all panels indicate the approximate positions of the pre-edge r, at 8979.0 eV, and the lowest and highest energy rising edge positions observed at different SOCs, s and t, at 8981.9 eV and 8982.4 eV, respectively. 140

S36 The second shell values of (a) $r_{\text{eff.}}$ and (b) N from Fe K-edge EXAFS analysis of $Li_{2.2}Al_{0.2}Fe_{0.6}S_2$, with (c) accompanying galvanostatic data indicating the SOCs at which EXAFS analysis is conducted. Panels (d), (e), and (f), respectively, indicate the same corresponding data for $Li_{1.8}Cu_{0.4}Al_{0.2}Fe_{0.6}S_2$. Panels (d) and (e) additionally include $r_{\text{eff.}}$ and N, respectively, from Cu K-edge EXAFS analysis of $Li_{1.8}Cu_{0.4}Al_{0.2}Fe_{0.6}S_2$. All $r_{\text{eff.}}$ and N values are shown with statistical error bars. Fe K-edge EXAFS data points are marked with solid red circles, while Cu K-edge EXAFS data points are marked with dashed cyan circles. The first shell data is discussed in the main text. The second shell data shows similar trends for $Li_{2.2}Al_{0.2}Fe_{0.6}S_2$ and $Li_{1.8}Cu_{0.4}Al_{0.2}Fe_{0.6}S_2$. 141

S37 Fe K-edge EXAFS $k^3\chi(k)$ data, fit, fit window, and fit-data difference of the (a) pristine, (b) transition, (c) charged, and (d) discharged states of $Li_{2.2}Al_{0.2}Fe_{0.6}S_2$. The first shell data is discussed in the main text. 141

S38 Fe K-edge EXAFS $k^3\chi(k)$ data, fit, fit window, and fit-data difference of the (a) pristine, (b) transition, (c) charged, and (d) discharged states of $Li_{1.8}Cu_{0.4}Al_{0.2}Fe_{0.6}S_2$. 142

S39 Cu K-edge EXAFS $k^3\chi(k)$ data, fit, fit window, and fit-data difference of the (a) pristine, (b) transition, (c) charged, and (d) discharged states of $Li_{1.8}Cu_{0.4}Al_{0.2}Fe_{0.6}S_2$. 142

S40 Fe K-edge EXAFS k^3-weighted $|\chi(R)|$ data, fit, fit window, and fit-data difference of the (a) pristine, (b) transition, (c) charged, and (d) discharged states of $Li_{2.2}Al_{0.2}Fe_{0.6}S_2$. 143

S41 Fe K-edge EXAFS k^3-weighted $|\chi(R)|$ data, fit, fit window, and fit-data difference of the (a) pristine, (b) transition, (c) charged, and (d) discharged states of $Li_{1.8}Cu_{0.4}Al_{0.2}Fe_{0.6}S_2$. 143

S42 Cu K-edge EXAFS k^3-weighted $|\chi(R)|$ data, fit, fit window, and fit-data difference of the (a) pristine, (b) transition, (c) charged, and (d) discharged states of $Li_{1.8}Cu_{0.4}Al_{0.2}Fe_{0.6}S_2$. 144

S43 XRD of the attempted synthesis of $Al_{0.2}Fe_{0.6}S_2$. The Rietveld refinement (fit), reflection locations of each phase in the fit, the weight percent contribution of each phase, and the difference between the fit and data are all shown. All observed reflections are accounted for by a three-phase fit to FeS_2 (51.1 wt%), Al_2FeS_4 (38.3 wt%), and Fe_7S_8 (10.6 wt%). 147

S44 XRD of the attempted synthesis of $Cu_{0.2}Al_{0.2}Fe_{0.6}S_2$. The Rietveld refinement (fit), reflection locations of each phase in the fit, the weight percent contribution of each phase, and the difference between the fit and data are all shown. All but a few minor reflections between 20°and 30°2θ are accounted for by a three-phase fit to FeS_2 (45.8 wt%), $CuFeS_2$ (40.7 wt%), and Fe_7S_8 (13.6 wt%). 147

S45 XRD of the attempted synthesis of $Cu_{0.4}Al_{0.2}Fe_{0.6}S_2$. The Rietveld refinement (fit), reflection locations of each phase in the fit, the weight percent contribution of each phase, and the difference between the fit and data are all shown. All but a few minor reflections between 20°and 30°2θ are accounted for by a three-phase fit to $CuFeS_2$ (63.8 wt%), FeS_2 (31.6 wt%), and Fe_7S_8 (4.6 wt%). 148

S46 (a) S K-edge XAS spectra of $Li_{2.2}Al_{0.2}Fe_{0.6}S_2$ in the pristine, transition, and annealed states. (b) Galvanostatic data indicating the SOCs at which the XAS data was collected for $Li_{2.2}Al_{0.2}Fe_{0.6}S_2$. The corresponding data for $Li_{1.8}Cu_{0.4}Al_{0.2}Fe_{0.6}S_2$ are in (c) and (d), respectively. The dashed lines in (a) and (c) indicate the two pre-edge features u and v, at 2469.2 eV and 2471.8 eV, respectively. 148

S47 (a) *Ex-situ* Cu K-edge XAS spectra, (b) magnified pre-edge region, and (c) first derivative of the rising edge regions for $Li_{1.8}Cu_{0.4}Al_{0.2}Fe_{0.6}S_2$ in the pristine, transition, and annealed states. (d) The energies of the maxima of the first derivatives at each of the SOCs are overlaid with representative galvanostatic cycling data. The dashed lines in all panels indicate the approximate positions of the pre-edge r, at 8979.0 eV, and the lowest and highest energy rising edge positions observed at different SOCs, s and t, at 8981.9 eV and 8982.4 eV, respectively. . 149

S48 *Ex-situ* XRD of the annealed states of (a) $Li_{2.2}Al_{0.2}Fe_{0.6}S_2$ and (b) $Li_{1.8}Cu_{0.4}Al_{0.2}Fe_{0.6}S_2$, and the transition states of (c) $Li_{2.2}Al_{0.2}Fe_{0.6}S_2$ and (d) $Li_{1.8}Cu_{0.4}Al_{0.2}Fe_{0.6}S_2$. Each panel shows the Rietveld refinement (fit), reflection locations of each phase in the fit, and the difference between the fit and data. All patterns are described by a single phase, except $Li_{1.8}Cu_{0.4}Al_{0.2}Fe_{0.6}S_2$ in the annealed state, which is fit to two phases: chalcopyrite $CuFeS_2$ (8.6 wt%), and $Li_{1.8-x}Cu_{0.4}Al_{0.2}Fe_{0.6}S_2$ (91.4 wt%). While we label the phases in the fits as $Li_{2.2-x}$ in (a) and (c) or $Li_{1.8-x}$ in (b) and (d) to indicate delithiated samples, the crystallographic information files used for the refinements are those of pristine (fully lithiated) $Li_{2.2}Al_{0.2}Fe_{0.6}S_2$ and $Li_{1.8}Cu_{0.4}Al_{0.2}Fe_{0.6}S_2$. 150

S49 The volumetric energy density versus the gravimetric energy density for commercial Li-ion battery cathodes NMC811 and LFP, and the emerging cathodes DRX, Li_2FeS_2, $Li_{2.2}Al_{0.2}Fe_{0.6}S_2$, $Li_2Cu_{0.2}Al_{0.2}Fe_{0.6}S_2$, and $Li_{1.8}Cu_{0.4}Al_{0.2}Fe_{0.6}S_2$. Relevant values and references for determining the gravimetric and volumetric energy densities are provided in Table S14. 150

LIST OF TABLES

Number *Page*

S1 Rietveld refinement results for sXRD patterns of Li_2FeS_2, $Li_{2.2}Al_{0.2}Fe_{0.6}S_2$, and $Li_{2.4}Al_{0.4}Fe_{0.2}S_2$ using the $P2_1/m$ monoclinic space group unit cell, corresponding to Figure 2.2a, b, and c, respectively. 94

S2 The composition of four separate reaction batches, two each of Li_2FeS_2 and $Li_{2.2}Al_{0.2}Fe_{0.6}S_2$, measured by ICP-MS for Li, Al, and Fe, and by combustion analysis for S. The data are normalized to the target Fe content. 98

S3 The possible impurities that we check for the unfit reflections in the sXRD patterns for Li_2FeS_2 and $Li_{2.2}Al_{0.2}Fe_{0.6}S_2$ in Figure 2.2a and b, respectively. We check all polymorphs of each listed impurity, e.g., for FeS_2 we check the pyrite and marcasite polymorphs. The lists of possible impurities for reaction with the quartz tube and air exposure are summarized by chemical formulae that account for all possible combinations. We check all possible polymorphs/combinations that are in the Inorganic Crystal Structure Database under "experimental inorganic structures". 98

S4 The averages and standard deviations of the first cycle charge capacities of the three replicates of Li_2FeS_2, $Li_{2.2}Al_{0.2}Fe_{0.6}S_2$, and $Li_{2.4}Al_{0.4}Fe_{0.2}S_2$ in Figure S3. 98

S5 The averages and standard deviations of the first cycle charge and discharge gravimetric capacities, average voltages, and energy densities of the three replicates of Li_2FeS_2 and $Li_{2.2}Al_{0.2}Fe_{0.6}S_2$ in Figure S3. . 103

S6 Detected S content in wt% before and after annealing by combustion analysis. We also show the S loss in wt% and convert this to mole S per f.u. based on approximate molar masses of 129.7 g·mole^{-1} of $Li_{2-x}FeS_2$ ($x \approx 0.6$) and 115.5 g·mole^{-1} of $Li_{2.2-x}Al_{0.2}Fe_{0.6}S_2$ ($x \approx 0.4$). The results show that S loss cannot explain the changes we observe after annealing –$Li_{2.2}Al_{0.2}Fe_{0.6}S_2$ shows no S loss and Li_2FeS_2 shows very minimal S loss. 110

S7 All Mössbauer fit parameters of each spectrum in Figures S16 and S17. 114

S8 EXAFS fitting parameters for Li_2FeS_2 and $Li_{2.2}Al_{0.2}Fe_{0.6}S_2$. 121

S9 Relevant values and references used to determine the gravimetric and volumetric energy densities shown in Figure S24. For the emerging cathodes, i.e., DRX and those presented here, we also specify the rate in mA/g at which the performance metrics are reported. 126

S10 Rietveld refinement results for sXRD patterns of $Li_{2.2}Al_{0.2}Fe_{0.6}S_2$, $Li_2Cu_{0.2}Al_{0.2}Fe_{0.6}S_2$, and $Li_{1.8}Cu_{0.4}Al_{0.2}Fe_{0.6}S_2$ using the $P2_1/m$ monoclinic space group unit cell, corresponding to Figure 4.2a, b, and c, respectively. 131

S11 The averages and standard deviations of the first cycle charge capacities of the three replicates of $Li_{2.2}Al_{0.2}Fe_{0.6}S_2$, $Li_2Cu_{0.2}Al_{0.2}Fe_{0.6}S_2$, and $Li_{1.8}Cu_{0.4}Al_{0.2}Fe_{0.6}S_2$ in Figure S25. 134

S12 The averages and standard deviations of the first cycle charge and discharge gravimetric capacities, average voltages, and energy densities of the three replicates of $Li_{2.2}Al_{0.2}Fe_{0.6}S_2$, $Li_2Cu_{0.2}Al_{0.2}Fe_{0.6}S_2$, and $Li_{1.8}Cu_{0.4}Al_{0.2}Fe_{0.6}S_2$ in Figure S25. 137

S13 EXAFS fitting parameters for $Li_{2.2}Al_{0.2}Fe_{0.6}S_2$ and $Li_{1.8}Cu_{0.4}Al_{0.2}Fe_{0.6}S_2$. 145

S14 Relevant values and references used to determine the gravimetric and volumetric energy densities shown in Figure S49. For the emerging cathodes, i.e., DRX, LMFP, and those presented here, we also specify the rate in mA/g at which the performance metrics are reported. . . . 151

Chapter 1

INTRODUCTION—Li-ION BATTERY FIRST PRINCIPLES

Iton, Z. W. B.; Kim, S. S.; Patheria, E. S.; Qian, M. D.; Ware, S. D.; See, K. A. Battery materials. *Comprehensive Inorganic Chemistry III* **2023**, 308–363.

Patheria, E. S.; Iton, Z. W. B.; Laskowski, F. A. L.; See, K. A. Li-Ion Battery First Principles. *In preparation.*

ABSTRACT

Chapter 1 develops a thermodynamic model for Li-ion batteries based on electrochemical potentials across all major phases—anode, electrolyte, and cathode. By explicitly accounting for both Li^+ and e^- electrochemical potentials, the framework explains equilibrium and non-equilibrium behavior—including voltage, charge transfer, and interfacial electrostatics—from first principles. This foundation unifies atomistic and device-level perspectives on Li-ion battery operation and sets the stage for multielectron redox chemistries explored in later chapters.

1.1 Introduction

As a first-year PhD student, I watched a National Academy of Sciences (NAS) Chemical Sciences Roundtable titled "*Advances, Challenges, and Long-Term Opportunities of Electrochemistry: Addressing Societal Needs*", held on November 18-19, 2019. It was just over one month after the Nobel Prize in Chemistry had been awarded jointly to Dr. John B. Goodenough, Dr. M. Stanley Whittingham, and Dr. Akira Yoshino for the development of Li-ion batteries. It was especially exciting to see Li-ion batteries finally receive this long-overdue recognition—as even the Nobel Prize press release acknowledged: "This lightweight, rechargeable and powerful battery is now used in everything from mobile phones to laptops and electric vehicles. It can also store significant amounts of energy from solar and wind power, making possible a fossil fuel-free society."[1] In our excitement, all the first-year rotators, See Group members, and our advisor Dr. Kimberly A. See gathered each morning by 4:50 AM PT in Lecture Hall 153 of the Arthur Amos Noyes Laboratory of Chemical Physics to watch the livestream of the workshop, which would begin at 8:00 AM ET in Washington, D.C.

Dr. Larry Faulkner opened the workshop by emphasizing that: "Electrochemistry connects electrical energy and the material world—this will always be a most important linkage for human existence."[2] While he was likely directly referring to chemical materials, his words can be interpreted more broadly: electrochemistry links electrical energy not only with chemicals, but also with the material conditions that shape the human condition and quality of life. To me, this is the most exciting and beautiful aspect of electrochemistry: that it links electricity and chemicals at both atomic and societal scales. Fundamentally, via e^- transfer, electrochemistry converts between energy stored in electric fields and chemical energy stored in matter. Broadly, this process can shape a more sustainable society and improve human welfare by storing renewable electricity in chemical form. In a world facing the dual moral imperatives of eradicating energy poverty and combating climate change, electrochemistry offers a pathway to achieve both without compromise.

While electrochemistry underpins many different technologies today, batteries are arguably the most widely used—and most directly embody the definition of electrochemistry itself. A battery toggles between electrical and chemical energy via electrochemical reactions that occur concomitantly at two electrodes termed the anode and cathode. During discharge, an oxidation reaction at the anode releases electrons into the external circuit and is accompanied by a reduction reaction at the

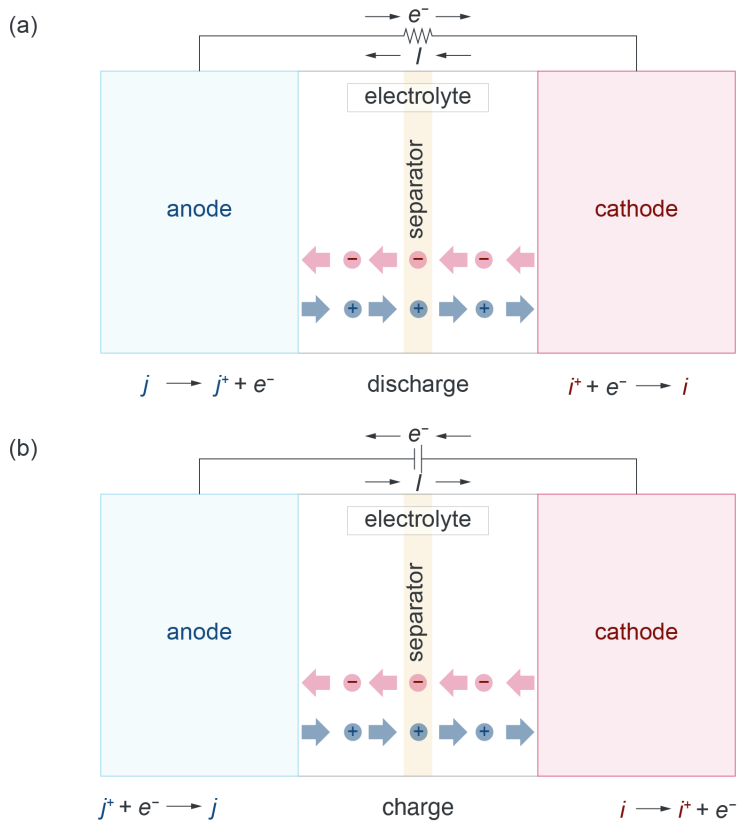

Figure 1.1: All batteries contain an anode, electrolyte, and cathode. An electrolyte-permeable, electronically-insulating separator between the anode and cathode prevents electrical contact between the electrodes. The electrolyte is electronically insulating and ionically conducting. In the schematics, electrons are indicated as e^-, the anode material as j, and the cathode material as i. The solvated ions in the electrolyte are indicated as + and −. (a) During discharge, j is oxidized to j^+ at the anode, and i^+ is reduced to i at the cathode. Discharge is spontaneous. (b) During charge, j^+ is reduced to j, and i is oxidized to i^+. The names of the two electrodes, anode vs. cathode, are defined for the spontaneous reaction. Charging the battery requires an applied voltage across the cell. For both charge and discharge the direction of e^- and current I flow through the external circuit is indicated.

cathode that consumes the electrons. The gain and loss of electrons is charge balanced by ions that conduct across the electronically insulating electrolyte as depicted in Figure 1.1.[3]

Key definitions

A schematic of a general battery during discharge is shown in Figure 1.1a. Chemical energy is converted into electrical energy spontaneously and current flows from the cathode to the anode. By convention, the direction of current flow I is opposite to

the flow of electrons. The electrode nomenclature is defined during the discharge when oxidation occurs at the anode and reduction occurs at the cathode. An easy way to remember this convention is the mnemonic "An Ox" and "Red Cat." Thermodynamically speaking, the potential energy of the anode is higher than that of the cathode and thus the reaction is spontaneous.

A schematic during charge is shown in Figure 1.1b. Analogously, electrical energy is converted into chemical energy upon applying a voltage across the cell to drive the uphill reaction. Now, the oxidation reaction occurs at the cathode and the reduction reaction at the anode. Although the opposite reaction is occurring at each electrode, the battery community colloquially conserves designation of the electrodes (anode vs. cathode) as it was defined for the discharge (spontaneous) reactions. The reduction and oxidation reactions that occur at the electrodes are called half reactions. The corresponding half reaction at each electrode is indicated below the electrode in Figure 1.1. If the half reactions are irreversible, the battery can only be discharged once and is called a primary battery/cell. Alternatively, if the half reactions are reversible, the battery is rechargeable and is called a secondary battery/cell. The two half reactions together give the full redox reaction of the battery. For example, the half reactions and full reaction for the battery in Figure 1.1 are:

$$\text{anode half reaction: } j \longrightarrow j^+ + \mathrm{e}^- \tag{1.1}$$

$$\text{cathode half reaction: } i^+ + \mathrm{e}^- \longrightarrow i \tag{1.2}$$

$$\text{full cell reaction: } j + i^+ \longrightarrow j^+ + i \tag{1.3}$$

Although the equations are written with cations j^+ and i^+ and indicate a single e^- transfer, j^+ and i^+ could be replaced by anions, and the e^- transfer could instead involve multiple electrons. The standard reduction potentials of many half reactions are tabulated and can be used to estimate the thermodynamic cell potential. The standard reduction potential E^0 describes a reduction reaction at standard conditions and thus the potential of the full cell described above is calculated by $E^0_{\text{cell}} = E^0_c - E^0_a$ where E^0_c is thestandard reduction potential of the cathodic half reaction and E^0_a is the standard reduction potential of the anodic half reaction. Positive cell potentials yield negative Gibbs free energy ($\Delta\, G^0$) and thus spontaneous reactions:

$$\Delta G^0 = -n\,F\,E^0_{\text{cell}}$$
$$\Delta G = -n\,F\,E_{\text{cell}} \tag{1.4}$$

where n is the number of electrons transferred and F is Faraday's constant (96485 C·mol^{-1}). In the second equation, we drop the superscript 0 implying that the same relationship holds in non-standard conditions.

The species j and i are called the electrochemically active species. That is, the electrochemically active species are the species in the anode and cathode which change oxidation state in the half reactions and store charge. Discrete changes in formal oxidation state are often used to describe the charge compensation mechanisms in battery materials, however, such a description becomes less accurate in materials with delocalized electrons or holes and/or covalent bonds. It is more accurate to say the electrochemically active species are the species on which changes in charge density are most localized during the half reactions. In other words, the electrochemically active species are the species that have occupied density of states near the Fermi level.

The ions + and − in the electrolyte in Figure 1.1 conduct the ionic component of the full cell reaction. As written above, + and − are general and could refer to any cation or anion. At least one or more of the ions in the electrolyte will also appear in the half reactions (consider, for instance, if + $=j^+$). Such ions are called working ions. The working ion can undergo reduction and oxidation itself or simply act as a charge-compensating ion, as is the case for Li^+ in a Li-ion battery.

1.2 The Li-ion battery model system

While the discussion so far applies to any type of battery, we now turn to a general Li-ion system—reflecting this thesis's central focus on multielectron redox in novel Li-ion cathodes. We can modify the half-reactions above to include a Li^+ working ion. The Li^+ is both in the electrolyte and reacts at the electrodes; the ion + in Figure 1.1 is taken to be Li^+ for this analysis. The half reactions and full cell reaction for a general Li-ion battery can be written as:

$$\text{anode half reaction: } \mathrm{Li}M_1 \longrightarrow \mathrm{Li}^+ + \mathrm{e}^- + M_1 \tag{1.5}$$

$$\text{cathode half reaction: } \mathrm{Li}^+ + \mathrm{e}^- + M_2 \longrightarrow \mathrm{Li}M_2 \tag{1.6}$$

$$\text{full cell reaction: } \mathrm{Li}M_1 + M_2 \longrightarrow M_1 + \mathrm{Li}M_2 \tag{1.7}$$

Note that the formal oxidation state of Li^+ remains unchanged and M_1 and M_2 are the electrochemically active species. In a Li-ion battery, M_1 is often graphite and M_2 is a metal oxide. We start from the general thermodynamic identity for the electrochemical Gibbs free energy.

$$d\bar{G} = -S\,dT + V\,dP + \sum_{\alpha}\sum_{\beta} \bar{\mu}^{\alpha}_{\beta}\,dN^{\alpha}_{\beta} \tag{1.8}$$

where $\bar{G}$ is the electrochemical Gibbs free energy, S is entropy, T is temperature, V is volume, P is pressure, and $\bar{\mu}^{\alpha}_{\beta}$ is the electrochemical potential of species α in phase β, and N is the number of particles. α indexes over the different phases in the system and β indexes over different charge species (e.g., multiple working ions, electrons).

Recall that the electrochemical potential $\bar{\mu}^{\alpha}_{\beta}$ is the partial molar Gibbs free energy of a given species β in phase α, composed of the sum of its chemical potential μ^{α}_{β}, which determines diffusive equilibrium, and electrostatic potential ϕ^{α}_{β}, which determines electrostatic equilibrium.[4]

$$\bar{\mu}^{\alpha}_{\beta} = \left(\frac{\partial \bar{G}^{\alpha}}{\partial N^{\alpha}_{\beta}}\right)_{T,P} = \mu^{\alpha}_{\beta} + z_{\beta} F \phi^{\alpha}_{\beta} \tag{1.9}$$

z_{β} is the signed charge number of β (e.g., +1, −1, +2, −2), and F is the Faraday constant (96485 C·mol^{-1}).

In the Li-ion battery model system, we take the temperature and pressure as constants, and we have only the Li^+ working ion and electrons e^-, so the thermodynamic identity simplifies as below:

$$(d\bar{G})_{T,P} = \sum_{\alpha} \bar{\mu}^{\alpha}_{\mathrm{Li}^+}\,dN^{\alpha}_{\mathrm{Li}^+} + \bar{\mu}^{\alpha}_{\mathrm{e}^-}\,dN^{\alpha}_{\mathrm{e}^-} \tag{1.10}$$

The derivative in the electrochemical Gibbs free energy of the cell can be written in terms of the Li^+ and e^- concentrations in all phases. The three major phases indicated in Figure 1.1 are the anode, electrolyte, and cathode.

$$
\begin{aligned}
(d\bar{G})_{T,P} = \bar{\mu}^{\text{anode}}_{\text{Li}^+}\, dN^{\text{anode}}_{\text{Li}^+} + \bar{\mu}^{\text{anode}}_{\text{e}^-}\, dN^{\text{anode}}_{\text{e}^-} \\
+ \bar{\mu}^{\text{cathode}}_{\text{Li}^+}\, dN^{\text{cathode}}_{\text{Li}^+} + \bar{\mu}^{\text{cathode}}_{\text{e}^-}\, dN^{\text{cathode}}_{\text{e}^-} \\
+ \bar{\mu}^{\text{electrolyte}}_{\text{Li}^+}\, dN^{\text{electrolyte}}_{\text{Li}^+}
\end{aligned}
\tag{1.11}
$$

Note that the electrolyte, unlike the anode and cathode, conducts only Li^+ and other dissolved ions. The electrolyte (typically an organic solvent in a Li-ion battery) is highly insulating with respect to e^- or hole (h^+) species.

We integrate to get:

$$
\begin{aligned}
\int (d\bar{G})_{T,P} = \int \bar{\mu}^{\text{anode}}_{\text{Li}^+}\, dN^{\text{anode}}_{\text{Li}^+} + \int \bar{\mu}^{\text{anode}}_{\text{e}^-}\, dN^{\text{anode}}_{\text{e}^-} \\
+ \int \bar{\mu}^{\text{cathode}}_{\text{Li}^+}\, dN^{\text{cathode}}_{\text{Li}^+} + \int \bar{\mu}^{\text{cathode}}_{\text{e}^-}\, dN^{\text{cathode}}_{\text{e}^-} \\
+ \int \bar{\mu}^{\text{electrolyte}}_{\text{Li}^+}\, dN^{\text{electrolyte}}_{\text{Li}^+}
\end{aligned}
\tag{1.12}
$$

$$
\begin{aligned}
\bar{G} = \bar{\mu}^{\text{anode}}_{\text{Li}^+}\, N^{\text{anode}}_{\text{Li}^+} + \bar{\mu}^{\text{anode}}_{\text{e}^-}\, N^{\text{anode}}_{\text{e}^-} + \bar{\mu}^{\text{cathode}}_{\text{Li}^+}\, N^{\text{cathode}}_{\text{Li}^+} + \bar{\mu}^{\text{cathode}}_{\text{e}^-}\, N^{\text{cathode}}_{\text{e}^-} \\
+ \bar{\mu}^{\text{electrolyte}}_{\text{Li}^+}\, N^{\text{electrolyte}}_{\text{Li}^+}
\end{aligned}
\tag{1.13}
$$

Equivalently:

$$
\bar{G} = G^{\text{cathode}}_{\text{Li}^+} + G^{\text{cathode}}_{\text{e}^-} + G^{\text{electrolyte}}_{\text{Li}^+} + G^{\text{anode}}_{\text{e}^-} + G^{\text{anode}}_{\text{Li}^+} \tag{1.14}
$$

One might think that $dN^{\text{electrolyte}}_{\text{Li}^+}$ is always equal to 0, so this term in Equation 1.12 could be dropped. However, we define two separate Gibbs free energies. The first is $\bar{G}$, which is the total Gibbs free energy of the battery. This term would increase if we were to (for example) increase the concentration of Li^+ in the electrolyte, as this would result in a higher chemical potential of Li^+ just by virtue of being more concentrated. Later on, we define ΔG_{cell} (Equation 1.27), which is the Gibbs free energy difference between the electrodes. This is the same ΔG as in $\Delta G = -nF\Delta E$ –Equation 1.4. In this ΔG_{cell} term, the term dN_{Li^+} indeed goes to 0 because any change in the concentration of Li^+ in the electrolyte will be cancelled out by equal and opposite effects at each electrode interface.

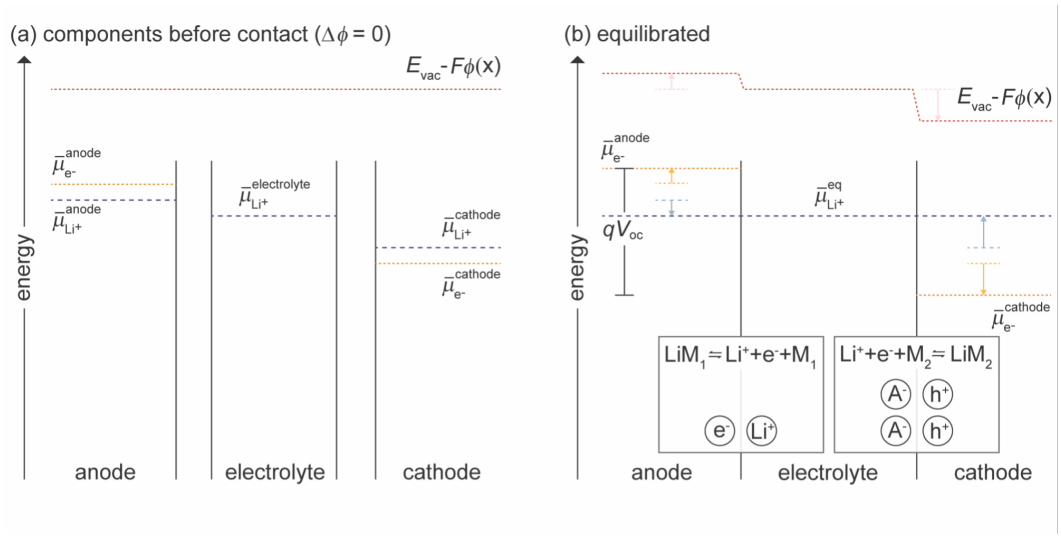

Figure 1.2: Example schematic showing the state of relevant electrochemical potentials for the cell components before assembly and at open-circuit equilibrium. (a) The pre-assembly diagram illustrates that the electrochemical potentials are located at higher energies in the anode than in the cathode. (b) The equilibrium diagram shows how the electrochemical potentials move in response to the electrostatic potential drop formed at each interface. The electrostatic potential drop forms because of the reactions shown in the insets, which produce or consume local Li^+-e^- pairs. A mismatch in the $\bar{\mu}^{\alpha}_{Li^+}$ levels across either interface is a driving force for the associated interfacial reaction; the reaction will proceed until the consequent electrostatic potential drop negates the difference in chemical potential across the interface, yielding a flat electrochemical potential profile. The measured OCV at equilibrium is given by the difference in the electrochemical potentials for the electrons. Note that because of the sign difference, the interfacial electric fields act in opposite manner on the electrochemical potentials for Li^+ vs. e^-.

The general equilibrium condition

At equilibrium, the total electrochemical Gibbs free energy for the battery must be minimized. The minimization of the electrochemical Gibbs free energy happens through changes in the electrochemical potentials for each species. In the bulk of the anode, cathode, and electrolyte, any gradient in the Li^+ electrochemical potential produces drift and diffusion of Li^+. The flux, J, of Li^+ in phase α can be written as:

$$J^{\alpha}_{Li^+} = -\left(\frac{C^{\alpha}_{Li^+} D^{\alpha}_{Li^+}}{RT}\right) \nabla \bar{\mu}^{\alpha}_{Li^+} \tag{1.15}$$

$C^{\alpha}_{Li^+}$ is the concentration, $D^{\alpha}_{Li^+}$ is the diffusion coefficient, and $\nabla \bar{\mu}^{\alpha}_{Li^+}$ is the gradient in electrochemical potential for Li^+ in α.[4] Movement of Li^+ through drift and diffusion alters the chemical potential term in Equation 1.9, thereby altering the

electrochemical potential.

At the interfaces, the Li^+ electrochemical potentials can equilibrate through changes in the interfacial electrostatic potential drop. Any initial mismatch in the electrochemical potential at the interface is equivalent to a mismatch in the electrochemical Gibbs free energy (Equation 1.9). Thus, a mismatch in electrochemical potential at the interface will spontaneously drive the relevant chemical reaction (Equations 1.5 and 1.6) to either produce or consume Li^+-e^- pairs. Note that Equations 1.5 and 1.6 not only describe the half-reactions in a closed circuit (i.e., charge or discharge) but also in open-circuit conditions, wherein the half-reactions occur at dynamic equilibrium at the electrode/electrolyte interfaces.

Without an external circuit to compensate charge, any generated Li^+-e^- pairs remain close to achieve local charge neutrality: the Li^+ in solution remains adjacent to the e^- in the electrode. Similarly, consumed Li^+-e^- pairs produce anion$--h^+$ pairs that remain proximal. The excess charges at the interfaces generate an electrostatic potential drop that counteracts any mismatch in chemical potential across the interface. The relationship between the charge density accumulated at each interface and the resulting electrostatic potential is captured by the 1D Poisson-Boltzmann equation.

$$\rho(x) = -\varepsilon\varepsilon_0 \frac{d^2\phi}{dx^2} \tag{1.16}$$

where $\rho(x)$ is the excess charge at position x, $\varepsilon\varepsilon_0$ is the permittivity, and ϕ is the electrostatic potential. Equation 1.9 depends on the electrostatic potential, indicating that the electrochemical potential can be altered through Equations 1.5 and 1.6.

While the Li^+ electrochemical potential can be altered by movement of Li^+, equilibration of the e^- electrochemical potential is constrained by the electronically insulating nature of the electrolyte. Unlike metals or semiconductors, organic electrolytes cannot support free e^- or h^+ concentrations. For a metal–metal contact, any interfacial mismatch in the e^- electrochemical potential will force charge to flow, following the drift–diffusion equation.[4] To retain local neutrality, an interfacial layer of h^+-e^- pairs will form, creating an electrostatic potential drop via the Poisson–Boltzmann relationship. However, for the electrode–electrolyte interface in a battery, no such equilibration process can take place because the interface does not support e^- or h^+ conduction. Any e^- electrochemical potential mismatch between the anode and cathode cannot be resolved at open circuit.

With the e^- electrochemical potential constrained, minimization of the electrochemical Gibbs free energy only depends on the Li^+ terms: $G^{C}_{Li^+}$, $G^{E}_{Li^+}$, and $G^{A}_{Li^+}$. The terms are related by their Li^+ concentrations, the sum of which is a constant quantity:

$$N^{\text{total}}_{Li^+} = N^{\text{cathode}}_{Li^+} + N^{\text{electrolyte}}_{Li^+} + N^{\text{anode}}_{Li^+} \tag{1.17}$$

Since any Li^+ concentration term can be written as a function of the other two, there exist only two independent variables. Thus, we can write an expression for the minimization of the electrochemical Gibbs free energy, $\min(\bar{G})$, in terms of the minimization of just two independent variables: $N^{\text{anode}}_{Li^+}$ and $N^{\text{electrolyte}}_{Li^+}$.

$$\begin{aligned}\min(\bar{G}) &\approx \min\left(G^{\text{cathode}}_{Li^+} + G^{\text{electrolyte}}_{Li^+} + G^{\text{anode}}_{Li^+}\right)\\ &= \min\Big[\bar{\mu}^{\text{anode}}_{Li^+} N^{\text{anode}}_{Li^+} + \bar{\mu}^{\text{electrolyte}}_{Li^+} N^{\text{electrolyte}}_{Li^+}\\ &\quad + \bar{\mu}^{\text{cathode}}_{Li^+}\left(N^{\text{total}}_{Li^+} - N^{\text{anode}}_{Li^+} - N^{\text{electrolyte}}_{Li^+}\right)\Big]\end{aligned} \tag{1.18}$$

Note that the e^- terms in Equation 1.13 are neglected in Equation 1.18 because they are effectively constant and will not be relevant for minimization. Only the electrons at the interfaces (a few nanometers) are involved in minimization, which is negligible relative to the number of electrons in the bulk of each electrode ($N^{\text{interfaces}}_{e^-} \ll N^{\text{bulk}}_{e^-}$).

The electrochemical Gibbs free energy is minimized when the partial gradient with respect to each independent variable is equal to 0[5] (the mathematical condition for a minimum):

$$\left(\frac{\partial \bar{G}}{\partial N^{\text{anode}}_{Li^+}}\right)_{N^{\text{electrolyte}}_{Li^+}} = 0 \tag{1.19}$$

and

$$\left(\frac{\partial \bar{G}}{\partial N^{\text{electrolyte}}_{Li^+}}\right)_{N^{\text{anode}}_{Li^+}} = 0 \tag{1.20}$$

Solving the above partial derivatives yields:

$$\left(\frac{\partial \bar{G}}{\partial N^{\text{anode}}_{Li^+}}\right)_{N^{\text{electrolyte}}_{Li^+}} = \bar{\mu}^{\text{anode}}_{Li^+} - \bar{\mu}^{\text{cathode}}_{Li^+} = 0 \tag{1.21}$$

and

$$\left(\frac{\partial \bar{G}}{\partial N_{\mathrm{Li}^+}^{\mathrm{electrolyte}}}\right)_{N_{\mathrm{Li}^+}^{\mathrm{anode}}} = \bar{\mu}_{\mathrm{Li}^+}^{\mathrm{electrolyte}} - \bar{\mu}_{\mathrm{Li}^+}^{\mathrm{cathode}} = 0 \tag{1.22}$$

By combining both results we find the equilibrium condition:

$$\bar{\mu}_{\mathrm{Li}^+}^{\mathrm{anode}} = \bar{\mu}_{\mathrm{Li}^+}^{\mathrm{electrolyte}} = \bar{\mu}_{\mathrm{Li}^+}^{\mathrm{cathode}} \tag{1.23}$$

Figure 1.2 shows schematics of the relevant electrochemical potentials across the anode, electrolyte, and cathode before (Figure 1.2a) and after equilibration (Figure 1.2b). The before state represents the situation where the cell has yet to be constructed (i.e., no contact between components). The interfacial equilibration occurs for $\bar{\mu}_{\mathrm{Li}^+}^{\alpha}$ because the interfacial reactions (Equations 1.5 and 1.6) can alter the electrostatic potential drop at the interfaces. The constant value of $\mu_{\mathrm{Li}^+}^{\mathrm{eq}}$ across the cell in Figure 1.2b reflects that the electrochemical potential of Li^+ is uniform at equilibrium, as required by the equilibrium condition (Equation 1.23). The change in the electrostatic potential is shown in the vacuum energy (E_{vac}) in Figure 1.2b.

Electrochemical origin of cell voltage

The equilibrium cell voltage can now be calculated by considering the smallest perturbation from equilibrium. We evaluate how the electrochemical Gibbs free energy changes as a single e^- is either charged or discharged. We label equations for charge with "a" and discharge with "b". Note that an e^- flowing from the cathode to the anode is accompanied by a Li^+.

For the cathode, the electrochemical Gibbs free energy change per particle charged (Equation 24a) and discharged (Equation 24b) are:

$$\begin{aligned}\Delta G_{\mathrm{cathode}}\left(\frac{\text{Joules}}{\text{particle}}\right) = {} & \bar{\mu}_{\mathrm{Li}^+}^{\mathrm{cathode}} N_{\mathrm{Li}^+}^{\mathrm{cathode}}\left(N_{\mathrm{Li}^+}^{\mathrm{cathode}} - 1\right) + \bar{\mu}_{\mathrm{e}^-}^{\mathrm{cathode}}\left(N_{\mathrm{e}^-}^{\mathrm{cathode}} - 1\right) \\ & - \bar{\mu}_{\mathrm{Li}^+}^{\mathrm{cathode}} N_{\mathrm{Li}^+}^{\mathrm{cathode}} - \bar{\mu}_{\mathrm{e}^-}^{\mathrm{cathode}} N_{\mathrm{e}^-}^{\mathrm{cathode}}\end{aligned} \tag{24a}$$

$$\begin{aligned}\Delta G_{\mathrm{cathode}}\left(\frac{\text{Joules}}{\text{particle}}\right) = {} & \bar{\mu}_{\mathrm{Li}^+}^{\mathrm{cathode}} N_{\mathrm{Li}^+}^{\mathrm{cathode}}\left(N_{\mathrm{Li}^+}^{\mathrm{cathode}} + 1\right) + \bar{\mu}_{\mathrm{e}^-}^{\mathrm{cathode}}\left(N_{\mathrm{e}^-}^{\mathrm{cathode}} + 1\right) \\ & - \bar{\mu}_{\mathrm{Li}^+}^{\mathrm{cathode}} N_{\mathrm{Li}^+}^{\mathrm{cathode}} - \bar{\mu}_{\mathrm{e}^-}^{\mathrm{cathode}} N_{\mathrm{e}^-}^{\mathrm{cathode}}\end{aligned} \tag{24b}$$

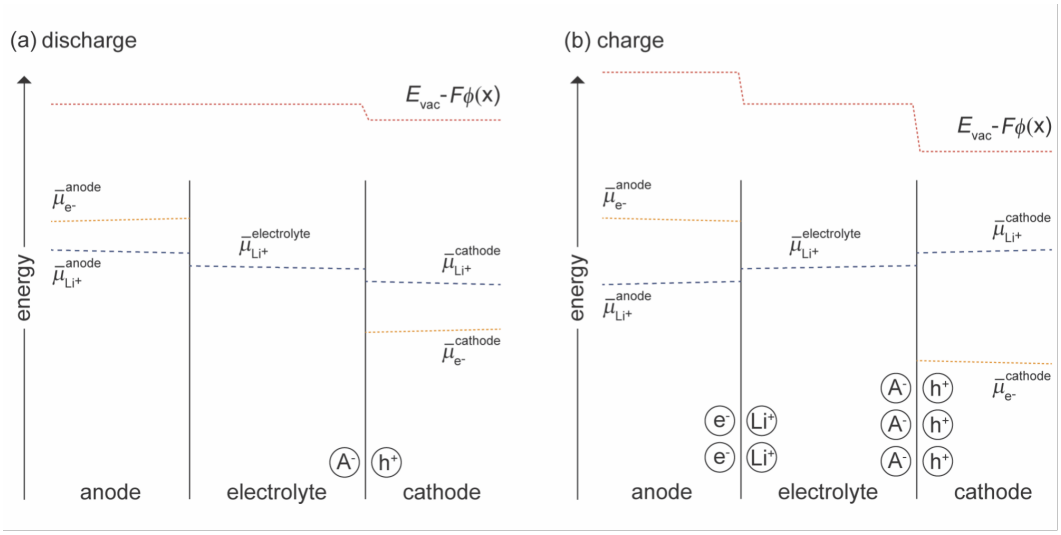

Figure 1.3: (a) During discharge, the external circuit allows electrons to move directly from the anode to cathode. The electrostatic potential drop at the anode|electrolyte interface diminishes as electrons are removed, which pushes $\bar{\mu}_{\mathrm{Li}^+}^{\mathrm{anode}}$ to higher energies. Similarly, electrons arriving at the cathode diminish the electrostatic potential drop at the electrolyte|cathode interface, which pushes $\bar{\mu}_{\mathrm{Li}^+}^{\mathrm{cathode}}$ to lower energies. Li^+ flows from left to right across the interfaces, giving rise to a concentration gradient (visualized here by the slight slope in the electrochemical potentials). (b) During charge, an external device imposes an external voltage more positive than the OCV onto the cell. The applied voltage is achieved via increases in the interfacial electrostatic potential drops. Relative to $\bar{\mu}_{\mathrm{Li}^+}^{\mathrm{electrolyte}}$, the anode and cathode's $\bar{\mu}_{\mathrm{Li}^+}^{\alpha}$ move to energies more negative and positive, respectively. Li^+ flows from right to left across the interfaces, giving rise to concentration gradients.

and for the anode are:

$$\Delta G_{\mathrm{anode}}\left(\frac{\text{Joules}}{\text{particle}}\right) = \bar{\mu}_{\mathrm{Li}^+}^{\mathrm{anode}}\left(N_{\mathrm{Li}^+}^{\mathrm{anode}}+1\right) + \bar{\mu}_{\mathrm{e}^-}^{\mathrm{anode}}\left(N_{\mathrm{e}^-}^{\mathrm{anode}}+1\right) - \bar{\mu}_{\mathrm{Li}^+}^{\mathrm{anode}} N_{\mathrm{Li}^+}^{\mathrm{anode}} - \bar{\mu}_{\mathrm{e}^-}^{\mathrm{anode}} N_{\mathrm{e}^-}^{\mathrm{anode}} \tag{25a}$$

$$\Delta G_{\mathrm{anode}}\left(\frac{\text{Joules}}{\text{particle}}\right) = \bar{\mu}_{\mathrm{Li}^+}^{\mathrm{anode}}\left(N_{\mathrm{Li}^+}^{\mathrm{anode}}-1\right) + \bar{\mu}_{\mathrm{e}^-}^{\mathrm{anode}}\left(N_{\mathrm{e}^-}^{\mathrm{anode}}-1\right) - \bar{\mu}_{\mathrm{Li}^+}^{\mathrm{anode}} N_{\mathrm{Li}^+}^{\mathrm{anode}} - \bar{\mu}_{\mathrm{e}^-}^{\mathrm{anode}} N_{\mathrm{e}^-}^{\mathrm{anode}} \tag{25b}$$

The full electrochemical Gibbs free energy change is the sum of the anode and cathode components:

$$\begin{aligned}\Delta G_{\text{cell}}\left(\frac{\text{Joules}}{\text{particle}}\right) &= \Delta G_{\text{cathode}} + \Delta G_{\text{anode}} \\ &= \Big[\bar{\mu}^{\text{cathode}}_{\text{Li}^+} N^{\text{cathode}}_{\text{Li}^+}\left(N^{\text{cathode}}_{\text{Li}^+} - 1\right) + \bar{\mu}^{\text{cathode}}_{\text{e}^-}\left(N^{\text{cathode}}_{\text{e}^-} - 1\right) \\ &\quad -\bar{\mu}^{\text{cathode}}_{\text{Li}^+} N^{\text{cathode}}_{\text{Li}^+} - \bar{\mu}^{\text{cathode}}_{\text{e}^-} N^{\text{cathode}}_{\text{e}^-}\Big] \\ &\quad + \Big[\bar{\mu}^{\text{anode}}_{\text{Li}^+}\left(N^{\text{anode}}_{\text{Li}^+} + 1\right) + \bar{\mu}^{\text{anode}}_{\text{e}^-}\left(N^{\text{anode}}_{\text{e}^-} + 1\right) \\ &\quad -\bar{\mu}^{\text{anode}}_{\text{Li}^+} N^{\text{anode}}_{\text{Li}^+} - \bar{\mu}^{\text{anode}}_{\text{e}^-} N^{\text{anode}}_{\text{e}^-}\Big]\end{aligned} \tag{26a}$$

$$\begin{aligned}\Delta G_{\text{cell}}\left(\frac{\text{Joules}}{\text{particle}}\right) &= \Delta G_{\text{cathode}} + \Delta G_{\text{anode}} \\ &= \Big[\bar{\mu}^{\text{cathode}}_{\text{Li}^+} N^{\text{cathode}}_{\text{Li}^+}\left(N^{\text{cathode}}_{\text{Li}^+} + 1\right) + \bar{\mu}^{\text{cathode}}_{\text{e}^-}\left(N^{\text{cathode}}_{\text{e}^-} + 1\right) \\ &\quad -\bar{\mu}^{\text{cathode}}_{\text{Li}^+} N^{\text{cathode}}_{\text{Li}^+} - \bar{\mu}^{\text{cathode}}_{\text{e}^-} N^{\text{cathode}}_{\text{e}^-}\Big] \\ &\quad + \Big[\bar{\mu}^{\text{anode}}_{\text{Li}^+}\left(N^{\text{anode}}_{\text{Li}^+} - 1\right) + \bar{\mu}^{\text{anode}}_{\text{e}^-}\left(N^{\text{anode}}_{\text{e}^-} - 1\right) \\ &\quad -\bar{\mu}^{\text{anode}}_{\text{Li}^+} N^{\text{anode}}_{\text{Li}^+} - \bar{\mu}^{\text{anode}}_{\text{e}^-} N^{\text{anode}}_{\text{e}^-}\Big]\end{aligned} \tag{26b}$$

Simplified:

$$\begin{aligned}\Delta G_{\text{cell}}\left(\frac{\text{Joules}}{\text{particle}}\right) &= \Delta G_{\text{cathode}} + \Delta G_{\text{anode}} \\ &= \left[-\bar{\mu}^{\text{cathode}}_{\text{Li}^+} - \bar{\mu}^{\text{cathode}}_{\text{e}^-}\right] + \left[\bar{\mu}^{\text{anode}}_{\text{Li}^+} + \bar{\mu}^{\text{anode}}_{\text{e}^-}\right]\end{aligned} \tag{27a}$$

$$\begin{aligned}\Delta G_{\text{cell}}\left(\frac{\text{Joules}}{\text{particle}}\right) &= \Delta G_{\text{cathode}} + \Delta G_{\text{anode}} \\ &= \left[\bar{\mu}^{\text{cathode}}_{\text{Li}^+} + \bar{\mu}^{\text{cathode}}_{\text{e}^-}\right] + \left[-\bar{\mu}^{\text{anode}}_{\text{Li}^+} - \bar{\mu}^{\text{anode}}_{\text{e}^-}\right]\end{aligned} \tag{27b}$$

Recall Equation 1.4, $\Delta G_{\text{cell}} = -n\ e\ \Phi$. Via Equations 1.4 and 1.27, we can express Φ in terms of the electrochemical potentials of the electroactive species (we assume $n = 1$):

$$\Phi = -\frac{\left[-\bar{\mu}^{\text{cathode}}_{\text{Li}^+} - \bar{\mu}^{\text{cathode}}_{\text{e}^-}\right] + \left[\bar{\mu}^{\text{anode}}_{\text{Li}^+} + \bar{\mu}^{\text{anode}}_{\text{e}^-}\right]}{e} \tag{28a}$$

$$\Phi = -\frac{\left[\bar{\mu}^{\text{cathode}}_{\text{Li}^+} + \bar{\mu}^{\text{cathode}}_{\text{e}^-}\right] + \left[-\bar{\mu}^{\text{anode}}_{\text{Li}^+} - \bar{\mu}^{\text{anode}}_{\text{e}^-}\right]}{e} \tag{28b}$$

In Equation 1.28, we have not applied the equilibrium condition that $\bar{\mu}^{\text{cathode}}_{\text{Li}^+} = \bar{\mu}^{\text{anode}}_{\text{Li}^+}$ (Equation 1.23). Therefore, when a battery is in a non-equilibrium, non-OCV state

(i.e., actively charging or discharging), the total electrical energy per charge is the difference in the electrochemical potential of the working ion Li^+ at the cathode versus the anode, minus the difference in the electrochemical potential of electrons e^- at the cathode versus the anode—i.e., the net electrochemical potential difference of all charge species between the cathode and the anode (Equation 1.28). Figure 1.3 shows schematics of the relevant electrochemical potentials across the anode, electrolyte, and cathode during discharge (Figure 1.3a) and charge (Figure 1.3b).

When a battery is at equilibrium in an OCV state (i.e., disconnected from an external circuit), we can simplify Equation 1.28 by invoking the equilibrium condition Equation 1.23, such that the difference in the Li^+ terms in Equation 1.28 is 0—i.e., $\bar{\mu}^{\text{anode}}_{\text{Li}^+} = \bar{\mu}^{\text{cathode}}_{\text{Li}^+}$, so $\bar{\mu}^{\text{anode}}_{\text{Li}^+} - \bar{\mu}^{\text{cathode}}_{\text{Li}^+} = 0$.

$$\Phi_{\text{OCV}} = \frac{\bar{\mu}^{\text{cathode}}_{\text{e}^-} - \bar{\mu}^{\text{anode}}_{\text{e}^-}}{e} \tag{1.29a}$$

$$\Phi_{\text{OCV}} = -\frac{\bar{\mu}^{\text{anode}}_{\text{e}^-} - \bar{\mu}^{\text{cathode}}_{\text{e}^-}}{e} \tag{1.29b}$$

Thus, at equilibrium the total electrical energy per charge is solely the difference in the electrochemical potential of electrons at the cathode versus the anode, i.e., the net electrochemical potential difference of e^- between the electrodes (Figure 1.2b). Whereas, in non-equilibrium states, the total electrical energy per charge E_{cell} is the difference in the electrochemical potential of the working ion Li^+ at the cathode versus the anode, minus the difference in electrochemical potential of electrons e^- at the cathode versus the anode—i.e., the net electrochemical potential difference of all charge species between the cathode and the anode. As an aid to the reader's intuition, the schematics in Figures 1.2 and 1.3 are quantiative. The shift you see in the vacuum energy level is the exact shift that is applied to the electrochemical potentials. The shift is also a linear function of how many charges are shown at the interface. For example, the electrolyte|cathode interface in Figure 1.3b has 3× the interfacial charge as that same interface in panel Figure 1.3a. Consequently, the electrostatic potential drop is 3× greater. Additional resources that informed this section, though not directly cited, may offer helpful further reading.[6–11]

1.3 Thesis outline

Chapter 1 has outlined the thermodynamics of Li-ion batteries. The rest of this thesis focuses on novel multielectron redox in Li-rich, industrial-element sulfide cathodes. These cathodes leverage anion redox—specifically, the formation and

cleavage of S – S bonds via local structural distortions[12]—to achieve remarkably high gravimetric capacity and thus high energy density.[13] Chapter 2 introduces $Li_{2+y}Al_yFe_{1-2y}S_2$ cathodes and characterizes their multielectron redox mechanism. Because sulfides have weaker ligand fields than the oxides used in commercial cathodes, they typically exhibit lower voltage and must rely on high gravimetric capacity to achieve competitive energy density. Chapter 3 thus addresses the key question of what determines—and how to increase—the capacity limits of $Li_{2+y}Al_yFe_{1-2y}S_2$ cathodes. Chapter 4 expands the chemical space of industrial-element cathodes to include Cu, whose unique electronic interactions with S delocalize charge compensation beyond S – S bonds, while Cu-induced structural effects alter capacity limits. Lastly, Chapter 5 offers conclusions and an outlook on industrial-element sulfide cathodes in the broader context of Li-ion fundamental research and broader technology development.

Bibliography

[1] The Nobel Prize in Chemistry 2019. https://www.nobelprize.org/prizes/chemistry/2019/summary/, 2019.

[2] Chemical Sciences Roundtable, 11/18 - Electrochemistry: Past, Present, and Future. 2019.

[3] Goodenough, J. B. *Acc. Chem. Res.* **2013**, *46*, 1053–1061.

[4] Boettcher, S. W.; Oener, S. Z.; Lonergan, M. C.; Surendranath, Y.; Ardo, S.; Brozek, C.; Kempler, P. A. *ACS Energy Lett.* **2021**, *6*, 261–266.

[5] Van der Ven, A.; Deng, Z.; Banerjee, S.; Ong, S. P. *Chem. Rev.* **2020**, *120*, 6977–7019.

[6] Gasteiger, H.; Krischer, K.; Scrosati, B. *Lithium Batteries*; John Wiley & Sons, Ltd, 2013; Chapter 1, pp 1–19.

[7] Seeber, R.; Zanardi, C.; Inzelt, G. *ChemTexts* **2015**, *1*, 18.

[8] Radin, M. D.; Hy, S.; Sina, M.; Fang, C.; Liu, H.; Vinckeviciute, J.; Zhang, M.; Whittingham, M. S.; Meng, Y. S.; Van der Ven, A. *Advanced Energy Materials* **2017**, *7*, 1602888.

[9] Schmidt-Rohr, K. *J. Chem. Educ.* **2018**, *95*, 1801–1810.

[10] Chen, L.-Q. *MRS Bulletin* **2019**, *44*, 520–523.

[11] Boettcher, S. Electrochemical Thermodynamics and Potentials: Equilibrium and the Driving Forces for Electrochemical Processes. 2020.

[12] Zak, J. J.; Kim, S. S.; Laskowski, F. A. L.; See, K. A. An Exploration of Sulfur Redox in Lithium Battery Cathodes. *J. Am. Chem. Soc.* **2022**, *144*, 10119–10132.

[13] Patheria, E. S.; Guzman, P.; Soldner, L. S.; Qian, M. D.; Morrell, C. T.; Kim, S. S.; Hunady, K.; Priesen Reis, E. R.; Dulock, N. V.; Neilson, J. R.; Nelson Weker, J.; Fultz, B.; See, K. A. High-Energy Density Li-Ion Battery Cathode Using Only Industrial Elements. *J. Am. Chem. Soc.* **2025**, *147*, 9786–9799.

Chapter 2

MULTIELECTRON REDOX MECHANISM IN $Li_{2+y}Al_yFe_{1-2y}S_2$ CATHODES

Patheria, E. S.; Guzman, P.; Soldner, L. S.; Qian, M. D.; Morrell, C. T.; Kim, S. S.; Hunady, K.; Priesen Reis, E. R.; Dulock, N. V.; Neilson, J. R.; Nelson Weker, J.; Fultz, B.; See, K. A. High-Energy Density Li-Ion Battery Cathode Using Only Industrial Elements. *J. Am. Chem. Soc.* **2025**, *147*, 9786–9799.

ABSTRACT

Li-ion batteries are crucial for the global energy transition to renewables, but their scalability is limited by the supply of key elements used in commercial cathodes (e.g., Ni, Mn, Co, P). Therefore, there is an urgent need for next-generation cathodes composed of widely available and industrially scalable elements. Here, we introduce a Li-rich cathode based on the known material Li_2FeS_2, composed of low-cost elements (Al, Fe, S) that are globally mined and refined at industrial scale. We leverage the structural similarity between Li_2FeS_2 and Li_5AlS_4 to substitute redox-inactive Al^{3+} for Fe^{2+}, forming $Li_{2+y}Al_yFe_{1-2y}S_2$ ($0 \leq y \leq 0.5$). This substitution yields high gravimetric capacity ($\approx$450 mAh·g^{-1}) and energy density ($\gtrapprox$1000 Wh·kg^{-1}). We characterize the redox mechanism and find that the high energy density arises from an unusually extensive degree of anion redox via the $2\,S^{2-}/(S_2)^{2-}$ couple.

2.1 Introduction

It is estimated that between 100 to 400 TWh of energy storage are needed to decarbonize/electrify global transport and energy sectors by 2050.[1–3] To achieve that goal with commercial Li-ion batteries with $LiNi_xMn_yCo_zO_2$ (NMCxyz) cathodes, Ni and Co production must double their respective maximum historical compound annual growth rates for every year until 2050.[2] Although Mn production is greater than Ni and Co production, limited refining capacity for 'battery-grade' Mn forecasts supply shortages by 2030.[3, 4] Even with $LiFePO_4$ (LFP), refinement bottlenecks for battery-grade P imply supply shortages by 2030.[5] Cathodes reliant only on industrial metals, or industrial elements, would alleviate the supply challenges that impede the 'net zero by 2050' goal. We classify 'industrial elements' as elements with global production of at least 10^7 metric tons in 2023 in primarily elemental form with $\gtrapprox$99.5 wt% purity. For example, Al, Fe, and S meet both criteria; Ni and Co meet neither; and Mn and P meet the production but not the purity criterion.[6, 7] While Li itself does not meet the criteria, 'beyond Li-ion' batteries (e.g., Na-ion, aqueous Zn-ion, etc.) without any Li require new infrastructure, time, and investment to reach scale.[4, 8, 9] By contrast, next-generation Li-ion battery cathodes that contain only industrial elements, except for Li, could scale faster and at lower capital expenditure (CapEx) into Li-ion batteries by using existing infrastructure, just as Si anodes have already entered the market.[4]

Fe is the most globally produced transition metal, motivating research to develop high-performance cathodes that leverage Fe redox. The resurgence of LFP in commercial applications stems from its lower cost and more industrial element-like composition compared to NMC,[10] despite LFP's low energy density (≈580 $Wh{\cdot}kg^{-1}$, ≈2068 $Wh{\cdot}L^{-1}$)[11] compared to, for example, NMC811 (≈950 $Wh{\cdot}kg^{-1}$, ≈4500 $Wh{\cdot}L^{-1}$).[12] Just over a decade ago, efforts to develop Fe-based cathodes that outperform LFP sought to increase the voltage of $Fe^{2+/3+}$ redox. By means of iono-covalency/inductive effects, the voltage can be shifted by over ≈1.1 V[13] to a maximum of 3.9 V vs. Li/Li^+ in triplite $LiFeSO_4F$.[14] However, the energy density of $LiFeSO_4F$ remained close to that of LFP, limiting its commercial viability.[15] More recently, Heo et al. over-discharged amorphous $LiFeSO_4F$, achieving 906 $Wh{\cdot}kg^{-1}$.[16] However, this required converting $LiFeSO_4F$ to Li_2O, Fe^0, and $LiSO_3F$, and also required Li^+ at the anode in the as-assembled cell – requirements incompatible with current manufacturing techniques. Overall, high voltage $Fe^{2+/3+}$ redox in Fe-based cathodes has been unable to match the energy density of NMC, and high energy density requires conversion reactions.

Multielectron transition metal and anion redox processes in Li-rich materials invoke both intercalation and bond-forming/breaking reactions,[17] surpassing capacity limits of traditional single-e$^-$ transition metal redox. However, stabilizing the delithiated, oxidized state remains a key challenge. Multielectron redox increases energy density by increasing capacity, requiring reversible redox reactions even at deep delithiation levels. Initial delithiation involves 'transition metal oxidation,' emptying associated covalent *d*-*p* states.[18, 19] Deep delithiation, however, yields under-coordinated anions, creating associated nonbonding *p* states near the Fermi level.[18, 20–23] Often, the empty *d*-*p* states lie below the filled nonbonding *p* states, triggering anion to metal charge transfers that, in oxides, create reactive O peroxides/superoxides and promote $O_{2(g)}$ release.[20, 21, 24–27] The electronic reorganization and structural changes hinder electrochemically mediated anion redox involving the nonbonding *p* states. This issue is acute in Li-rich Fe-based oxides, specifically $Li_{1.17}Ti_{0.33}Fe_{0.5}O_2$[21] and $Li_{1.33}Fe_{0.33}Sb_{0.33}O_2$,[24] where deep delithiation incurs charge transfers from O^{2-} to $Fe^{3+/4+}$, associated with large hysteresis (≈1.4 V) and capacity fade (≈20% per cycle).

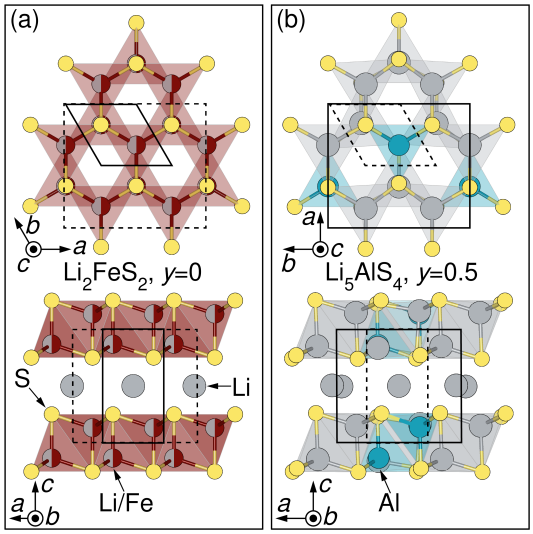

Figure 2.1: The crystal structure of (a) Li_2FeS_2 projected along the *c*-axis (top) and *b*-axis (bottom), and the crystal structure of (b) Li_5AlS_4 projected along the *c*-axis (top) and *b*-axis (bottom). In each panel, the solid black line indicates the unit cell of the structure shown, while the dashed black line indicates the unit cell of the other structure for comparison.

Here, to develop a Li-ion battery cathode entirely composed of industrial elements that achieves high energy density through multielectron redox, we target Li-rich, Fe-based sulfides derived from Li_2FeS_2. Sulfides must have extremely high capac-

ities and thus high Li content to match the energy density of NMC because S is heavier and less electronegative than O. For example, $Li_{1.13}Ti_{0.57}Fe_{0.3}S_2$ achieves only up to ≈600 Wh·kg^{-1}[28], despite having greater capacity in mole e$^-$ per f.u. than NMC cathodes. The crystal structure of Li_2FeS_2,[29] shown in Figure 2.1a along the *c* and *b* axes, adopts the P$\bar{3}$m1 trigonal space group with a hexagonal close-packed (HCP) sulfide anion framework and cations alternating between octahedral and tetrahedral sites in layers. Occupation of tetrahedral sites in the HCP sulfide anion framework enables higher Li content and thus higher capacity than typical Li-rich materials, which feature FCC anion frameworks and solely octahedral cation sites. Li_2FeS_2, studied for decades (see Supplementary Note S1), exhibits multielectron redox during charge by $Fe^{2+/3+}$ oxidation of Fe-S 3*d*-3*p* states, followed by 2 $S^{2-}/(S_2)^{2-}$ oxidation[30] of S 3*p* nonbonding states.[22] Inspired by the structural similarities between Li_2FeS_2 and the more Li-rich Li_5AlS_4, shown in Figure 2.1 and discussed in Structural characterization of $Li_{2+y}Al_yFe_{1-2y}S_2$ (vide infra), we control Fe and S contributions to multielectron redox by substituting Li^+ and Al^{3+} for 2 Fe^{2+} to yield $Li_{2+y}Al_yFe_{1-2y}S_2$ ($0 \leq y \leq 0.5$). Al is the second most industrial metal after Fe[6] and is relatively light. S is an abundant byproduct of processing fossil fuels[6] and exists as stable persulfides $(S_2)^{2-}$ in many 3*d* transition metal sulfides.[17] Together, Fe, Al, and S are highly attractive from scalability and performance perspectives. We demonstrate that $Li_{2.2}Al_{0.2}Fe_{0.6}S_2$ achieves high gravimetric capacity (≳450 mAh·g^{-1}) and energy density (≳1000 Wh·kg^{-1}) through extensive redox of ≈75% of the S, with much less capacity fade (≈1.8% per cycle) than Li-rich Fe-based oxides (≈20% per cycle).[21, 24] We compare multielectron redox in Li_2FeS_2 and $Li_{2.2}Al_{0.2}Fe_{0.6}S_2$ to understand why the latter accesses more S redox. We find that Al^{3+} stabilizes the delithiated state, suppressing internal charge transfers and structural changes, enabling electrochemically mediated anion redox over a wider capacity window. This insight creates new opportunities for developing next-generation Li-ion battery cathodes composed of scalable, industrial elements towards widespread deployment of Li-ion batteries to meet the 'net zero by 2050' goal.

2.2 Results and discussion

Structural characterization of $Li_{2+y}Al_yFe_{1-2y}S_2$

Substitution of Al^{3+} into Li_2FeS_2 is motivated by its structural similarity to Li_5AlS_4. Lim et al. first reported Li_5AlS_4 in 2018 and noted its structural similarity to Li_2FeS_2,[31] which others soon reiterated.[32–34] The crystal structure of Li_5AlS_4,[31]

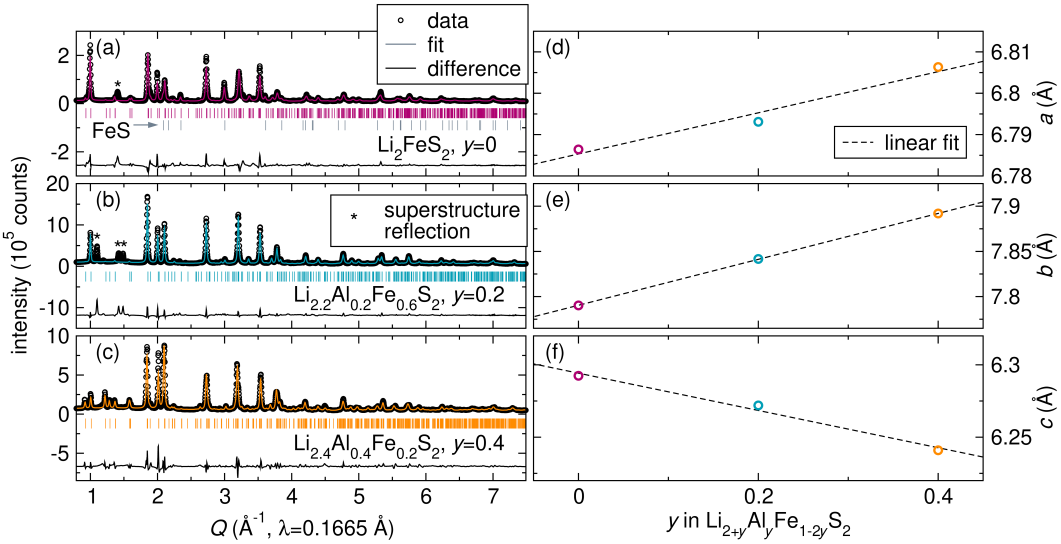

Figure 2.2: Synchrotron powder X-ray diffraction of (a) Li_2FeS_2, (b) $Li_{2.2}Al_{0.2}Fe_{0.6}S_2$, and (c) $Li_{2.4}Al_{0.4}Fe_{0.2}S_2$. The corresponding Rietveld refinement, reflection locations in Q (Å^{-1}) of each phase in the fit, and difference between fit and data are shown for each material. Superstructure reflections that are not fit by the Rietveld refinement are indicated by asterisks (*). The resulting lattice parameters (d) a, (e) b, and (f) c from each Rietveld refinement with respect to y in $Li_{2+y}Al_yFe_{1-2y}S_2$ with linear fits indicated by dashed lines. The lattice parameters follow a linear Vegard's trend, indicating that yLi$^+$ and yAl^{3+} successfully substitute for $2y$Fe^{2+} in $Li_{2.2}Al_{0.2}Fe_{0.6}S_2$ (y = 0.2) and $Li_{2.4}Al_{0.4}Fe_{0.2}S_2$ (y = 0.4).

shown in Figure 2.1b along the c and b axes, adopts the P2$_1$/m monoclinic space group with a unit cell that is a supercell of the primitive unit cell in P$\bar{3}$m1 if β were allowed to deviate slightly to equal 90° from 90.333°. The primary difference between Li_2FeS_2 and Li_5AlS_4 lies in the tetrahedral cation site occupancy. Li_2FeS_2 has disordered Li/Fe at a 1:1 ratio (Figure 2.1a), while Li_5AlS_4 has ordered Li/Al at a 3:1 ratio (Figure 2.1b). The ordering in Li_5AlS_4 slightly distorts its anion framework, yet we anticipate that yLi$^+$ and yAl^{3+} can be substituted for $2y$Fe^{2+} in Li_2FeS_2, to yield $Li_{2+y}Al_yFe_{1-2y}S_2$ ($0 \leq y \leq 0.5$).

We synthesize Li_2FeS_2 (y=0), $Li_{2.2}Al_{0.2}Fe_{0.6}S_2$ (y=0.2), and $Li_{2.4}Al_{0.4}Fe_{0.2}S_2$ (y=0.4) by solid-state synthesis from Li_2S, FeS, and Al_2S_3 at 900 °C. To confirm the substitution, we analyze synchrotron X-ray diffraction (sXRD) patterns for Li_2FeS_2, $Li_{2.2}Al_{0.2}Fe_{0.6}S_2$, and $Li_{2.4}Al_{0.4}Fe_{0.2}S_2$ shown in Figure 2.2a, b, and c, respectively, with the corresponding Rietveld refinements (Table S1), reflections associated with each phase in the fit, and the difference between the fit and data. We use the larger P2$_1$/m unit cell to fit all materials, comparing their lattice parameters. Site occupancy is determined by a linear combination of the two end-members, weighted

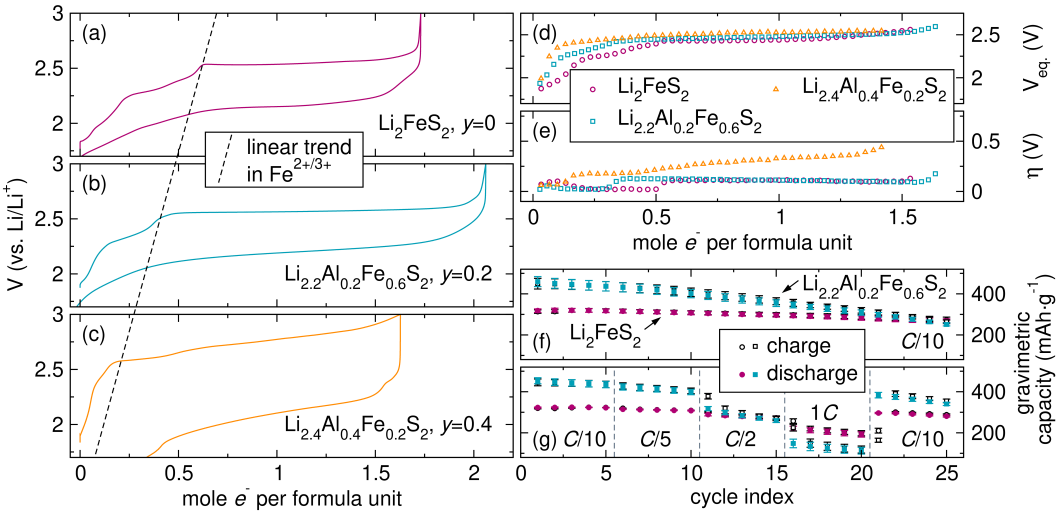

Figure 2.3: First cycle galvanostatic charge and discharge curves of (a) Li_2FeS_2, (b) $Li_{2.2}Al_{0.2}Fe_{0.6}S_2$, and (c) $Li_{2.4}Al_{0.4}Fe_{0.2}S_2$ cycled at $C/10$ based on 1 e^- per formula unit. The dashed line across panels (a), (b), and (c) indicates the linear trend in Fe oxidation capacity with y. (d) The equilibrium voltage $V_{eq.}$ and (e) overpotential η during the first charge extracted from GITT. (f) The cycling of Li_2FeS_2 and $Li_{2.2}Al_{0.2}Fe_{0.6}S_2$ at $C/10$. (g) Rate capability tests of Li_2FeS_2 and $Li_{2.2}Al_{0.2}Fe_{0.6}S_2$ for 5 cycles each at $C/10$, $C/5$, $C/2$, 1C, and again at $C/10$. All C rates are based on 1 e^- per formula unit. The data points in (f) and (g) are the average of three replicate cells and error bars indicate the standard deviations.

according to the target stoichiometry. We detect 5.9 wt% FeS[35] in Li_2FeS_2, but fit both $Li_{2.2}Al_{0.2}Fe_{0.6}S_2$ and $Li_{2.4}Al_{0.4}Fe_{0.2}S_2$ to single phases. The lattice parameters a, b, and c from the fits, plotted vs. Al content in Figure 2.2d, e, and f, respectively, follow linear Vegard trends, confirming the substitution. The refined phases deviate more from HCP symmetry as y increases (Figure S2), corroborating the Vegard trend. We also verify the stoichiometries of Li_2FeS_2 and $Li_{2.2}Al_{0.2}Fe_{0.6}S_2$ by inductively coupled plasma mass spectrometry (ICP-MS) and combustion analysis (Table S2). We mark certain unfit reflections between 1 to 2 $Å^{-1}$ for Li_2FeS_2 and $Li_{2.2}Al_{0.2}Fe_{0.6}S_2$ with asterisks (*), identifying them as likely superstructure reflections after ruling out several possible impurities (see Table S3) and considering historical discrepancies regarding superstructure in Li_2FeS_2 (see Supplementary Note S2).

Electrochemical characterization of $Li_{2+y}Al_yFe_{1-2y}S_2$

The electrochemical performance is evaluated with galvanostatic cycling. The first cycles of Li_2FeS_2, $Li_{2.2}Al_{0.2}Fe_{0.6}S_2$, and $Li_{2.4}Al_{0.4}Fe_{0.2}S_2$ at $C/10$ based on 1 e^- per formula unit are shown in Figure 2.3a, b, and c, respectively. All materials exhibit

the sloping $Fe^{2+/3+}$ oxidation region followed by the $2\,S^{2-}/(S_2)^{2-}$ plateau during charge.[30] A dashed line across Figure 2.3a, b, and c indicates a linear decrease in Fe oxidation capacity with y, confirming its proportionality to Fe content. We find that ≈60% to 75% of the Fe is oxidized during charge, suggesting an oxidation state limit between $Fe^{\approx 2.60+}$ to $Fe^{\approx 2.75+}$. The S oxidation capacity is greater for $Li_{2.2}Al_{0.2}Fe_{0.6}S_2$ (1.52 ±0.09 e^-) than Li_2FeS_2 (1.09 ±0.01 e^-), but does not increase much further for $Li_{2.4}Al_{0.4}Fe_{0.2}S_2$ (1.63 ±0.21 e^-). Three replicate cells from separate reaction batches for each material are shown in Figure S3, with tabulated capacities provided in Table S4.

We use the galvanostatic intermittent titration technique (GITT) to assess how kinetic properties change with y. The equilibrium voltage and overpotential during charge for Li_2FeS_2, $Li_{2.2}Al_{0.2}Fe_{0.6}S_2$, and $Li_{2.4}Al_{0.4}Fe_{0.2}S_2$, extracted from GITT, are shown in Figure 2.3d and e. Full GITT charge/discharge curves and representative relaxation curves are shown in Figure S4. $Li_{2.4}Al_{0.4}Fe_{0.2}S_2$ exhibits higher S oxidation overpotentials than Li_2FeS_2 and $Li_{2.2}Al_{0.2}Fe_{0.6}S_2$, which have identical overpotentials despite different Al^{3+} contents. The high Al^{3+} content of 0.4 heavily distorts the anion framework (Figure S2), likely hindering structural distortions required for facile S redox.

Due to the low capacity, large hysteresis, and sluggish kinetics in $Li_{2.4}Al_{0.4}Fe_{0.2}S_2$, we now focus on Li_2FeS_2 and $Li_{2.2}Al_{0.2}Fe_{0.6}S_2$. We show the capacity fade of Li_2FeS_2 and $Li_{2.2}Al_{0.2}Fe_{0.6}S_2$ at $C/10$ over 25 cycles in Figure 2.3f. Each data point and error bar represent the average and standard deviation of three replicate cells (Figure S5 shows individual cell data and coulombic efficiencies). We find that the capacity of Li_2FeS_2 fades more slowly, at ≈0.64% per cycle, compared to $Li_{2.2}Al_{0.2}Fe_{0.6}S_2$, which fades at ≈1.76% per cycle. Despite the fade, the galvanostatic curves of both materials retain their shape over multiple cycles (see Figure S6). The greater capacity fade of $Li_{2.2}Al_{0.2}Fe_{0.6}S_2$ is unsurprising, given that 76.9±1.5% of the total capacity comes from S redox, which incurs structural distortions, relative to only ≈65±1.5% in Li_2FeS_2 (Table S4). We also compare the rate capabilities of Li_2FeS_2 and $Li_{2.2}Al_{0.2}Fe_{0.6}S_2$ in Figure 2.3g (Figure S7 shows individual cell data). While Li_2FeS_2 retains more capacity at $1C$ compared to $Li_{2.2}Al_{0.2}Fe_{0.6}S_2$, both exhibit larger hysteresis at $1C$ (see Figure S8), and $Li_{2.2}Al_{0.2}Fe_{0.6}S_2$ retains its greater capacity upon returning to $C/10$. We note, however, that we use free standing electrodes (see Freestanding cathode preparation), which are poorly suited for extended cycling. We are optimizing cast electrodes to better assess the ca-

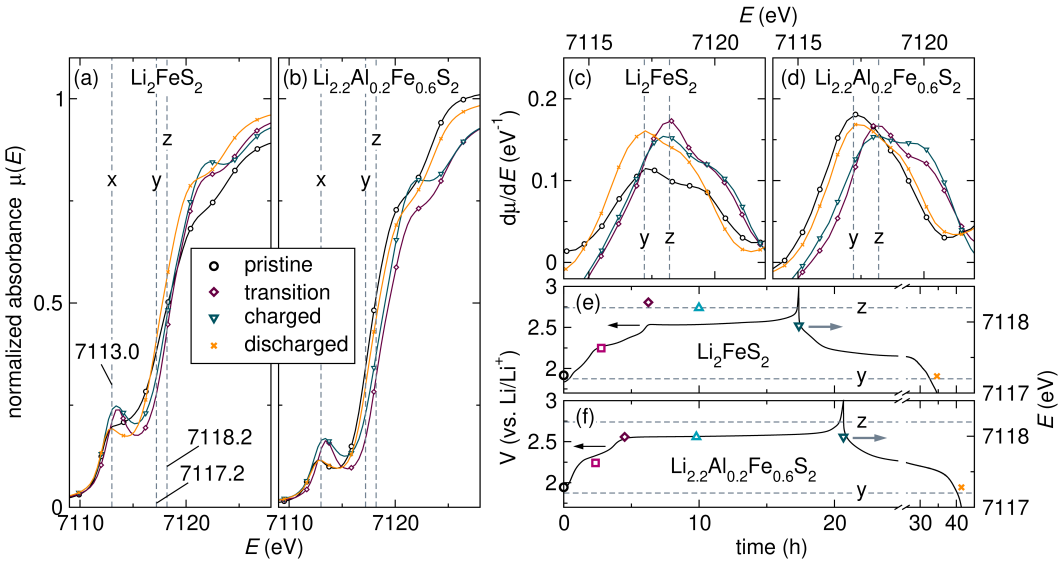

Figure 2.4: *Ex-situ* Fe K-edge XAS spectra of (a) Li_2FeS_2 and (b) $Li_{2.2}Al_{0.2}Fe_{0.6}S_2$. The first derivative of the rising edge regions for (c) Li_2FeS_2 and (d) $Li_{2.2}Al_{0.2}Fe_{0.6}S_2$. The energies of the maxima of the first derivatives at each of the SOCs are overlaid with the corresponding galvanostatic cycling data for (e) Li_2FeS_2 and (f) $Li_{2.2}Al_{0.2}Fe_{0.6}S_2$. The dashed lines in all panels indicate the approximate positions of the pre-edge x, at 7113.0 eV, and the two rising edges observed at different SOCs, y and z, at 7117.2 eV and 7118.2 eV, respectively.

pacity fade and rate capability. Regardless, $Li_{2.2}Al_{0.2}Fe_{0.6}S_2$ achieves extremely high initial charge/discharge capacities of 449±20 mAh·g^{-1}/446±24 mAh·g^{-1} and energy densities of 1125±49/1024±55 Wh·kg^{-1} (see Table S5 for the gravimetric capacities, average voltages, and energy densities of Li_2FeS_2 and $Li_{2.2}Al_{0.2}Fe_{0.6}S_2$).

Spectroscopic characterization of the multielectron redox mechanism

We spectroscopically characterize Li_2FeS_2 and $Li_{2.2}Al_{0.2}Fe_{0.6}S_2$ to evaluate charge compensation and check assignments of features in the galvanostatic data. We measure *ex-situ* Fe and S K-edge X-ray absorption spectroscopy (XAS) at six states of charge (SOCs) for both materials: (1) pristine, (2) mid-slope (halfway through the sloping region), (3) transition (at the transition point between the sloping and plateau regions), (4) mid-plateau (halfway through the plateau region), (5) charged, and (6) discharged.

First, we discuss the Fe K-edge XAS in Figure 2.4. The Fe K-edge near-edge regions for Li_2FeS_2 and $Li_{2.2}Al_{0.2}Fe_{0.6}S_2$ at the various SOCs are shown in Figure 2.4a and b. The spectra exhibit common features: a pre-edge at ≈7113.0 eV (labeled x), and a rising edge at ≈7117.2 eV (y) or ≈7118.2 eV (z), depending on the SOC. For both

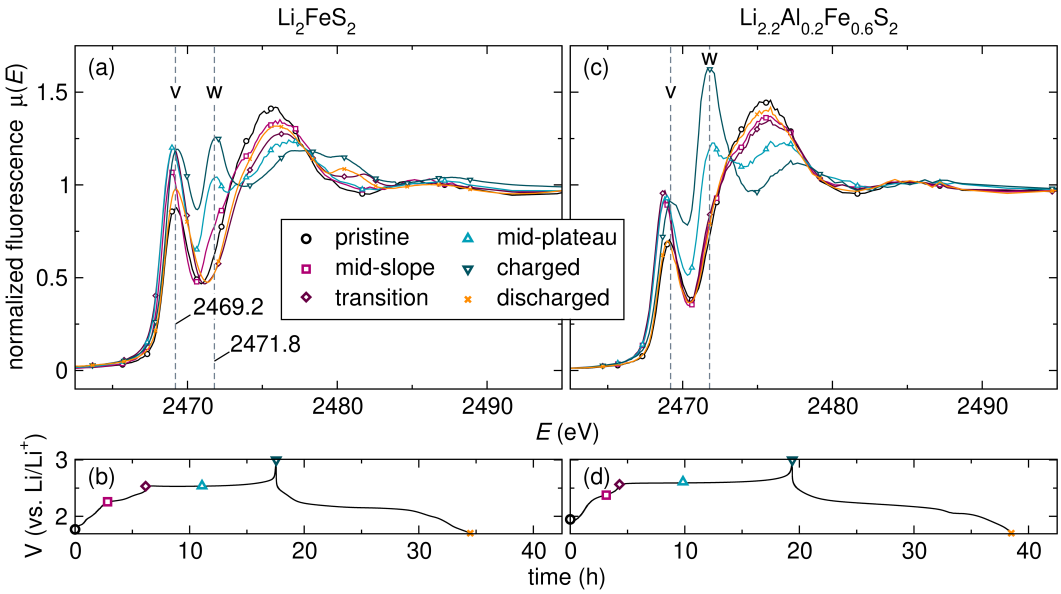

Figure 2.5: (a) *Ex-situ* S K-edge XAS and (b) a representative first cycle curve indicating the SOCs at which the XAS data was collected for Li_2FeS_2. The corresponding data for $Li_{2.2}Al_{0.2}Fe_{0.6}S_2$ are in (c) and (d), respectively. The dashed lines in (a) and (c) indicate the two pre-edge features *v* and *w*, at 2469.2 eV and 2471.8 eV, respectively.

materials, the pre-edge intensity increases at the transition SOC and stays constant at the charged state, suggesting that S oxidation does not affect Fe-S covalency or the Fe coordination environment.[36] The maxima of the first derivatives of the rising edge, shown in Figure 2.4c and d for Li_2FeS_2 and $Li_{2.2}Al_{0.2}Fe_{0.6}S_2$, increase by ≈1 eV from ≈7117.2 eV in the pristine state to ≈7118.2 eV at the transition SOC, and stay constant at the charged state. This confirms that Fe oxidation ceases after the transition SOC despite the majority of electron removal occurring during the plateau. The data from intermediate mid-slope and mid-plateau SOCs, shown in Figure S9, further support this finding. We summarize this result in Figure 2.4e,f, overlaying the rising edge positions with the galvanostatic data. For both Li_2FeS_2 and $Li_{2.2}Al_{0.2}Fe_{0.6}S_2$, the rising edge position increases during the sloping region indicating oxidation, and stays constant during the plateau.

Next, we discuss the S K-edge XAS in Figure 2.5. The Li_2FeS_2 spectra and corresponding galvanostatic data, shown in Figure 2.5a and b, is reproduced from Hansen et al.[30] with two new data points at the mid-slope and mid-plateau SOCs. During the sloping region, the pre-edge feature labeled *v* at 2469.2 eV grows in intensity, indicating greater Fe-S covalency.[30, 37] During the plateau, a new pre-edge feature labeled *w* at 2471.8 eV emerges that indicates persulfide formation,[30]

peaking in intensity at the charged state and vanishing at the discharged state. The appearance of the pre-edge feature *w* marks a switch from increasing Fe-S covalency to forming S-S bonds. The $Li_{2.2}Al_{0.2}Fe_{0.6}S_2$ spectra and corresponding galvanostatic data in Figure 2.5c and d exhibit the same trends as Li_2FeS_2, with pre-edge features *v* and *w* labeled at the same energies. The greater S oxidation capacity of $Li_{2.2}Al_{0.2}Fe_{0.6}S_2$ is confirmed by the much greater intensity of the pre-edge feature *w* at the charged state. The S oxidation is structurally reversible in both materials, as confirmed by *ex-situ* XRD (Supplementary Note S4 and Figures S10 and S11).

2.3 Conclusion

The materials presented in this work offer new pathways towards next-generation Li-ion battery cathodes. Figure S24 compares the volumetric and gravimetric energy densities of various commercial and emerging state-of-the-art lithiated cathode materials with Li_2FeS_2 and $Li_{2.2}Al_{0.2}Fe_{0.6}S_2$. While $Li_{2.2}Al_{0.2}Fe_{0.6}S_2$ has a lower volumetric energy density than state-of-the-art oxides due to its larger sulfide anions, its gravimetric energy density surpasses all reported lithiated cathode materials. A recent report shows that even highly optimized oxides, dubbed "integrated rocksalt-polyanion cathodes," can only match the energy density of $Li_{2.2}Al_{0.2}Fe_{0.6}S_2$ through overdischarge,[38] which, as we explain in the Introduction, is not scalable with current manufacturing techniques. $Li_{2.2}Al_{0.2}Fe_{0.6}S_2$ achieves this primarily through reversible redox of ≈80% of its anions with ≈100% Coulombic efficiency – the highest reported level of anion redox in a cathode material, exceeded only by conversion cathodes. The electrochemical performance of $Li_{2.2}Al_{0.2}Fe_{0.6}S_2$ paves the way for sulfides capable of high degrees of anion redox as high-performance cathodes composed of only the most industrial/scalable elements. Important next steps towards real-world energy impact include synthesizing $Li_{2+y}Al_yFe_{1-2y}S_2$ materials using industrial precursors like Li_2CO_3,[39] optimizing performance metrics through electrode and cell engineering, cost modeling, and examining drop-in compatibility with existing Li-ion battery manufacturing techniques.

2.4 Experimental

Materials preparation

All materials and precursors were handled inside an Ar-filled glovebox (H_2O and $O_2 \lessapprox 1$ ppm). All $Li_{2+y}Al_yFe_{1-2y}S_2$ ($0 \leq y \leq 0.5$) materials were prepared by solid-state synthesis. Powders of Li_2S (Thermo Fisher Scientific, 99.9%), FeS (Sigma

Aldrich, 99.9%), and Al_2S_3 (Thermo Fisher Scientific, 99+%) were weighed to an accuracy of ±0.1 mg to give total 250 mg of a desired stoichiometry (i.e., value of y) and then hand-mixed in an agate mortar and pestle. The mixed precursor powders were pressed into $\frac{1}{4}$ inch diameter cylindrical pellets with a hand-operated arbor press. The mixed precursor pellets were light gray in color. Pellets were placed inside carbon-coated vitreous silica ampules (10 mm i.d., 12 mm o.d.), evacuated to $\leq$ 50 mTorr, and sealed with a methane-oxygen torch without exposure to air. The ampules were coated by first rinsing the inside of the empty ampule with acetone, and then pyrolyzing residual acetone with a methane-oxygen torch. This was repeated at least twice for conformal, continuous coating. The evacuated and sealed ampule was then placed inside a box furnace and heated at 1 °C/min to 900 °C with a dwell time of 12 h. After ambient cooling to room temperature (approximately 1 °C/min), the ampules were opened inside the glovebox and the pellets were ground into fine powders in agate mortar and pestles for further characterization. Only the Li_2FeS_2 pellet melts into a polycrystalline boule when heated to 900 °C. The rest of the materials mostly retained the shape of the original pressed pellet. All products were black in both pellet and powder forms, except for $Li_{2.4}Al_{0.4}Fe_{0.2}S_2$ which is dark brown/red in powder form.

Synchrotron X-ray diffraction (sXRD) sample preparation

As prepared materials were packed into individual 1.0 mm (outer diameter) glass capillaries in an Ar-filled glovebox. Each capillary was evacuated to $\leq$ 50 mTorr and sealed with a methane-oxygen torch without exposing the sample to air. High-resolution sXRD patterns were collected on the sample-loaded capillaries at beam line 28-ID-1 (λ=0.1665 Å) at the National Synchrotron Light Source II at Brookhaven National Laboratory. The diffraction patterns were fit using the Rietveld method with the General Structure Analysis System II,[40] and crystal structures were visualized with VESTA.[41]

Inductively coupled plasma mass spectrometry (ICP-MS) and combustion analysis

ICP-MS was conducted at the Resnick Environmental Analysis Center at Caltech with an Agilent 8800 ICP-MS and argon plasma source. Roughly 3 mg of each synthesized batch of material was digested in 2 to 3 mL of concentrated HNO_3 (70 vol%) at 80 °C for 4 h. After the initial digestion, the solutions were twice diluted in dilute HNO_3 (5 vol%) to reach x2500 dilution. Final sample volumes were 25 mL.

Standard solutions were prepared by diluting stock solutions of Li, Al, and Fe to the desired concentrations with dilute HNO_3 (5 vol%) to create a calibration curve.

Combustion analysis to quantify S content was conducted in duplicate for each sample by Atlantic Microlab (atlanticmicrolab.com). In an Ar-filled glovebox, roughly 10-15 mg of each sample was put into a 5 or 10 mL glass scintillation vial and the cap was sealed with electrical tape. The sample-loaded vials were sealed under Ar in aluminized mylar pouches (2 to 3 layers) using an impulse heat sealer (Uline) for shipping to Atlantic Microlab.

Freestanding cathode preparation

Freestanding cathodes were prepared by mixing 60/20/20 (wt%) active material, carbon (Super P, Alfa Aesar, >99%), and PTFE binder (Sigma, 1 μm powder), respectively, in agate mortar and pestles. The active material and carbon were mixed first, then binder was added to evenly distribute the active material and carbon in the binder framework. The hand grinding with binder creates small flakes ($\approx$1 mm^2) that were broken into smaller pieces/a powder by hand with a stainless steel spatula. Roughly 6 to 10 mg of the composite fragmented mix was weighed and pressed into a 6 mm diameter electrode under ca. 2 tons of force using a manual hydraulic press (Vivtek), resulting in a freestanding cathode with a thickness of approximately 100 μm and an areal loading of roughly 12.7 to 21.2 mg·cm^{-2} of active material.

Electrochemical characterization

All electrochemical cells were assembled in an Ar-filled glovebox. Li-foil anodes with a diameter of $\frac{1}{2}$ inch were punched from either Li ribbon (Sigma, 99.9%, 0.75 mm) or Li chips (AOT Battery, 99.9%), both first mechanically cleaned with an Xacto blade immediately prior to cell assembly. Each Li anode, $\approx$0.75 mm thick, weighed $\approx$45 mg before cleaning, with minimal loss in both mass and thickness afterward, as the cleaning primarily removed the surface passivation layer. The electrolyte, 1 M LP30, was a 1 M solution of $LiPF_6$ (Oakwood chemical, battery grade) in a 1/1 (by volume) mixture of ethylene carbonate (EC) and dimethyl carbonate (DMC), both Sigma, $\geq$99%.[42] The electrolyte was made (and stored) in an HDPE bottle by combining the carbonates and the salt, and was first stored at least overnight before use to ensure all components dissolved/mixed well. All electrochemistry was performed in 2032 coin cells (MTI) assembled with a $\approx$0.88 g stainless steel top cap, $\approx$0.18 g stainless steel spring (MTI), $\approx$0.73 g stainless steel spacer (MTI), Li anode on the spacer, $\approx$17 mg $\frac{1}{2}$ inch diameter glass-fiber separator (Whatman,

GF/D), 100 μL of LP30 electrolyte (30 μL on the anode, 40 μL on the separator, 30 μL on the cathode), freestanding cathode, and ≈0.90 g stainless steel bottom can. The typical total mass of the as-assembled was ≈2.9 g. All stainless steel coin cell components were sonicated in roughly 1/1 acetone/isopropyl alcohol for 30 minutes and then dried overnight in a vacuum oven at 60 °C prior to use in the glovebox. The glass fiber separators were dried overnight in a vacuum oven at 60 °C prior to use in the glovebox. The coin cells were crimped shut with a manual crimper (Pred Materials). All electrochemical experiments were performed at room temperature (≈25 °C) with a BCS 805 battery cycler (Bio-Logic). For continuous galvanostatic cycling experiments, all materials were charged at a $C/10$ rate based on 1 e^- per f.u. up to 3 V, and discharged at the same rate to 1.7 V. For GITT experiments, currents were applied at the same $C/10$ rate for 20 minutes at a time separated by 4 hour rest periods. The equilibrium potential $V_{eq.}$ and overpotential η was extracted from the GITT using Python. The capacity fade rate (in % per cycle) for cycling at $C/10$ over 25 cycles was determined by calculating linear fits of the average charge and discharge capacities versus cycle number of three replicate cells, then taking the slope over the value of the fit function at x=1 (cycle 1), and finally averaging this value for the charge and discharge fits. For the rate capability tests, the same charge/discharge voltage cut-offs of 3/1.7 V were used, and the cells were cycled for 5 cycles each, sequentially, at $C/10$, $C/5$, $C/2$, $1C$, and back to $C/10$ (25 cycles total).

All *ex-situ* samples

All *ex-situ* samples were prepared in 2032 coin cells (MTI) with freestanding cathodes as previously described. Samples are first cycled to one of the following SOCs: mid-slope, transition, mid-plateau, charged, and discharged. For mid-slope samples, voltage cutoffs of ≈2.25 V for Li_2FeS_2 and ≈2.38 V for $Li_{2.2}Al_{0.2}Fe_{0.6}S_2$ were used. For transition samples, voltage cutoffs of ≈2.53 V for Li_2FeS_2 and ≈2.56 V for $Li_{2.2}Al_{0.2}Fe_{0.6}S_2$ were used. For mid-plateau samples, time cutoffs of ≈9.8 h for Li_2FeS_2 and ≈11.1 h for $Li_{2.2}Al_{0.2}Fe_{0.6}S_2$ were used. Due to slight cell-to-cell variation, cutoffs for these intermediate SOCs varied slightly and so for clarity are always shown with the full corresponding galvanostatic charge and discharge curves. For charged and discharged samples, voltage cutoffs of 3 V and 1.7 V, respectively, were used. After cycling to one of the above-defined cutoffs, the cells were de-cripmed and opened with a manual disassembling tool (Pred Materials) in an Ar-filled glovebox. The *ex-situ* cathodes were gently scraped off the current collector by hand

using a stainless steel spatula, keeping the cathode intact. Any visible glass fiber separator stuck on the cathode was manually scraped off the cathode surface with a stainless steel spatula. The cathodes were then rinsed with ≈300 μL of DMC for 2-3 minutes to wash away residual electrolyte. Any residual DMC was dabbed with a dry Kim wipe, and then the cathode was dried under vacuum for roughly 30 min. The dry intact cathodes were then either kept intact or broken into smaller pieces/a powder by hand with a stainless steel spatula, depending on the requirements of the subsequent characterization.

X-ray absorption spectroscopy (XAS)

Samples for *ex-situ* XAS were prepared in 2032 coin cells as previously described for *ex-situ* samples. The intact *ex-situ* cathodes, treated as previously described, were broken up into loose powders with a stainless steel spatula. All sample preparation described below was conducted in an Ar-filled glovebox. Prepared sample holders were sealed in Ar in aluminized mylar pouches (2 to 3 layers) using an impulse heat sealer (Uline) for transport to the respective synchrotrons. Calibration, background correction, and data processing of X-ray absorption near-edge structure was done in Athena from the IFEFIT suite.[43]

For Fe K-edge XAS, the loose powders were loaded into aluminum sample holders provided by the Stanford Synchrotron Radiation Lightsource (SSRL) at SLAC National Accelerator Laboratory, encapsulated between two pieces of Kapton tape (1 mil film thickness, 2.5 mil total thickness, Uline). All Fe K-edge XAS was measured in transmission mode at the SSRL at SLAC National Accelerator Laboratory. The Li_2FeS_2 data for the mid-slope and mid-plateau SOCs was measured at beam line 2-2. The rest of the data presented here was measured at beam line 4-3. In all cases, during measurement, the sample holder was placed in a continuous He-flushed chamber to minimize air exposure, and O_2 levels were measured to be ≈500 ppm with an O_2 sensor. Fe K-edge data were calibrated to a collinear Fe foil present for each sample. The data shown are three averaged sweeps of each sample, with each sweep taking roughly 20 minutes.

For S K-edge XAS, the loose powders were mixed by hand with agate mortar and pestles with boron nitride (BN) (Alfa Aesar, 99.5%) so that the total sample concentration was ≤5% by mass. Roughly 10 to 15 mg of each composite BN-sample mix was pressed into $\frac{1}{4}$ inch diameter pellets using a hand-operated arbor press. The pellets were then loaded into plastic sample holders provided by the

National Synchrotron Light Source II (NSLS-II) at Brookhaven National Laboratory (BNL), sandwiched between a polypropylene layer and Kapton tape and adhered to the sample holder using Kapton tape. S K-edge XAS was measured in fluorescence mode at beam line 8-BM at NSLS-II at BNL. During measurement, the sample holder was placed in a continuous He-flushed chamber to minimize air exposure. S K-edge data were calibrated to a gypsum, i.e., sulfate S^{6+}, standard (1 wt% $CaSO_4 \cdot 2\,H_2O$ in polyethylene glycol). The data shown are three averaged sweeps of each sample, with each sweep taking roughly 15 minutes.

CuK$_\alpha$ XRD

CuK$_\alpha$ XRD patterns were collected on a Rigaku SmartLab diffractometer. To prevent air exposure during measurement, samples were loaded inside an Ar-filled glovebox into a Rigaku-built air-free sample holder with a low background silicon sample platform. For synthesized materials, roughly 10 mg of sample powder was placed and compressed (by hand using a stainless steel spatula) onto the sample platform. For *ex-situ* cathodes, the cathode was kept intact and gently placed onto the sample platform. The diffraction patterns were fit using the Rietveld method with the General Structure Analysis System II (GSAS-II)[40] and crystal structures were visualized with VESTA.[41]

2.5 Funding and user-facility acknowledgments

This material is based upon work supported by the National Science Foundation (NSF) under Award No. DMR-2340864. K.A.S. acknowledges support from the Packard Fellowship for Science and Engineering, the Alfred P. Sloan Foundation, and the Camille and Henry Dreyfus Foundation. E.S.P. acknowledges support from the Robert and Patricia Switzer Foundation. E.S.P., M.D.Q., and C.T.M. acknowledge NSF Graduate Research Fellowship support under Award No. DGE-2139433. Initial work on this material was partially supported by the Center for Synthetic Control Across Length-scales for Advancing Rechargeables (SCALAR), an Energy Frontier Research Center funded by the U.S. Department of Energy, Office of Science, Basic Energy Sciences under award no. DE-SC0019381. This research used beam lines 2-2 and 4-3 at the Stanford Synchrotron Radiation Lightsource (SSRL). Use of SSRL, SLAC National Accelerator Laboratory, is supported by the U.S. Department of Energy, Office of Science, Office of Basic Energy Sciences under Contract No. DE-AC02-76SF00515. This research used beam lines 8-BM and 28-ID-1 of the National Synchrotron Light Source II (NSLS-II), a U.S. Department of Energy

(DOE) Office of Science User Facility operated for the DOE Office of Science by Brookhaven National Laboratory (BNL) under Contract No. DE-SC0012704. The authors thank the Resnick Environmental Analysis Center at Caltech for ICP-MS and the Beckman Institute and Caltech X-ray Crystallography Facility for CuK_α XRD. The authors also thank Dr. Yonghua Du and Dr. Sarah Nicholas at 8-BM (NSLS-II) for their assistance with S K-edge XAS, Dr. Gihan Kwon at 28-ID-1 (NSLS-II) for his help with sXRD, and Dr. Erik Nelson and Dr. Matthew Latimer at 2-2 and 4-3 (SSRL) for their help with Fe K-edge XAS.

Bibliography

[1] *Net Zero by 2050 – A Roadmap for the Global Energy Sector*; 2021.

[2] Armstrong, R.; Chiang, Y.-M.; Gruenspecht, H. *The Future of Energy Storage*; MIT Future Of; 2022.

[3] *Net Zero 2050 and the Battery Arms Race*; 2023.

[4] Frith, J. T.; Lacey, M. J.; Ulissi, U. A non-academic perspective on the future of lithium-based batteries. *Nat. Commun.* **2023**, *14*, 420.

[5] More Phosphoric Acid Refining Capacity Needed as LFP Demand Increases. https://source.benchmarkminerals.com/article/more-phosphoric-acid-refining-capacity-needed-as-lfp-demand-increases, 2023.

[6] *Mineral Commodity Summaries 2024*; USGS Numbered Series 2024, 2024.

[7] Putsche, V. L.; Pattany, J.; Ghosh, T.; Atnoorkar, S.; Zuboy, J.; Carpenter, A.; Takeuchi, E. S.; Marschilok, A. C.; Takeuchi, K. J.; Burrell, A.; Mann, M. K. A Framework for Integrating Supply Chain, Environmental, and Social Justice Factors during Early Stationary Battery Research. *Front. Sustain.* **2023**, *4*.

[8] Duffner, F.; Kronemeyer, N.; Tübke, J.; Leker, J.; Winter, M.; Schmuch, R. Post-lithium-ion battery cell production and its compatibility with lithium-ion cell production infrastructure. *Nat. Energy* **2021**, *6*, 123–134.

[9] Degen, F.; Winter, M.; Bendig, D.; Tübke, J. Energy consumption of current and future production of lithium-ion and post lithium-ion battery cells. *Nat. Energy* **2023**, *8*, 1284–1295.

[10] LFP 2.0 is not about the price of lithium, here's what's driving demand. https://source.benchmarkminerals.com/article/lfp-2-0-is-not-about-the-price-of-lithium-heres-whats-driving-demand, 2020.

[11] Yamada, A.; Chung, S. C.; Hinokuma, K. Optimized $LiFePO_4$ for Lithium Battery Cathodes. *J. Electrochem. Soc.* **2001**, *148*, A224.

[12] Manthiram, A.; Song, B.; Li, W. A perspective on nickel-rich layered oxide cathodes for lithium-ion batteries. *Energy Storage Mater.* **2017**, *6*, 125–139.

[13] Melot, B. C.; Scanlon, D. O.; Reynaud, M.; Rousse, G.; Chotard, J.-N.; Henry, M.; Tarascon, J.-M. Chemical and Structural Indicators for Large Redox Potentials in Fe-Based Positive Electrode Materials. *ACS Appl. Mater. Interfaces* **2014**, *6*, 10832–10839.

[14] Ati, M.; Melot, B. C.; Chotard, J. N.; Rousse, G.; Reynaud, M.; Tarascon, J. M. Synthesis and electrochemical properties of pure $LiFeSO_4F$ in the triplite structure. *Electrochem. Commun.* **2011**, *13*, 1280–1283.

[15] Rousse, G.; Tarascon, J. M. Sulfate-Based Polyanionic Compounds for Li-Ion Batteries: Synthesis, Crystal Chemistry, and Electrochemistry Aspects. *Chem. Mater.* **2014**, *26*, 394–406.

[16] Heo, J.; Jung, S.-K.; Hwang, I.; Cho, S.-P.; Eum, D.; Park, H.; Song, J.-H.; Yu, S.; Oh, K.; Kwon, G.; Hwang, T.; Ko, K.-H.; Kang, K. Amorphous iron fluorosulfate as a high-capacity cathode utilizing combined intercalation and conversion reactions with unexpectedly high reversibility. *Nat. Energy* **2023**, *8*, 30–39.

[17] Zak, J. J.; Kim, S. S.; Laskowski, F. A. L.; See, K. A. An Exploration of Sulfur Redox in Lithium Battery Cathodes. *J. Am. Chem. Soc.* **2022**, *144*, 10119–10132.

[18] Zhang, M.; Kitchaev, D. A.; Lebens-Higgins, Z.; Vinckeviciute, J.; Zuba, M.; Reeves, P. J.; Grey, C. P.; Whittingham, M. S.; Piper, L. F. J.; Van der Ven, A.; Meng, Y. S. Pushing the limit of 3*d* transition metal-based layered oxides that use both cation and anion redox for energy storage. *Nat. Rev. Mater.* **2022**, *7*, 522–540.

[19] Ogley, M. J. W. et al. Metal–Ligand Redox in Layered Oxide Cathodes for Li-ion Batteries. 2024.

[20] Hong, J. et al. Metal–oxygen decoordination stabilizes anion redox in Li-rich oxides. *Nat. Mater.* **2019**, *18*, 256–265.

[21] Li, B.; Sougrati, M. T.; Rousse, G.; Morozov, A. V.; Dedryvère, R.; Iadecola, A.; Senyshyn, A.; Zhang, L.; Abakumov, A. M.; Doublet, M.-L.; Tarascon, J.-M. Correlating ligand-to-metal charge transfer with voltage hysteresis in a Li-rich rock-salt compound exhibiting anionic redox. *Nat. Chem.* **2021**, *13*, 1070–1080.

[22] Kim, S. S.; Agyeman-Budu, D. N.; Zak, J. J.; Andrews, J. L.; Li, J.; Melot, B. C.; Nelson Weker, J.; See, K. A. Effect of Metal *d* Band Position on Anion Redox in Alkali-Rich Sulfides. *Chem. Mater.* **2024**, *36*, 6454–6463.

[23] Kim, S. S.; Kitchaev, D. A.; Patheria, E. S.; Morrell, C. T.; Qian, M. D.; Andrews, J. L.; Yan, Q.; Ko, S.-T.; Luo, J.; Melot, B. C.; Van der Ven, A.; See, K. A. Cation Vacancies Enable Anion Redox in Li Cathodes. *J. Am. Chem. Soc.* **2024**, *146*, 20951–20962.

[24] McCalla, E.; Sougrati, M. T.; Rousse, G.; Berg, E. J.; Abakumov, A.; Recham, N.; Ramesha, K.; Sathiya, M.; Dominko, R.; Van Tendeloo, G.; Novák, P.; Tarascon, J.-M. Understanding the Roles of Anionic Redox and Oxygen Release during Electrochemical Cycling of Lithium-Rich Layered Li_4FeSbO_6. *J. Am. Chem. Soc.* **2015**, *137*, 4804–4814.

[25] House, R. A.; Marie, J.-J.; Pérez-Osorio, M. A.; Rees, G. J.; Boivin, E.; Bruce, P. G. The role of O_2 in O-redox cathodes for Li-ion batteries. *Nat. Energy* **2021**, *6*, 781–789.

[26] Li, B.; Kumar, K.; Roy, I.; Morozov, A. V.; Emelyanova, O. V.; Zhang, L.; Koç, T.; Belin, S.; Cabana, J.; Dedryvère, R.; Abakumov, A. M.; Tarascon, J.-M. Capturing dynamic ligand-to-metal charge transfer with a long-lived cationic intermediate for anionic redox. *Nat. Mater.* **2022**, 1–10.

[27] Zak, J. J.; Zuba, M.; Lebens-Higgins, Z. W.; Huang, H.; Crafton, M. J.; Dalleska, N. F.; McCloskey, B. D.; Piper, L. F. J.; See, K. A. Irreversible Anion Oxidation Leads to Dynamic Charge Compensation in the Ru-Poor, Li-Rich Cathode $Li_2Ru_{0.3}Mn_{0.7}O_3$. *ACS Energy Lett.* **2023**, *8*, 722–730.

[28] Saha, S.; Assat, G.; Sougrati, M. T.; Foix, D.; Li, H.; Vergnet, J.; Turi, S.; Ha, Y.; Yang, W.; Cabana, J.; Rousse, G.; Abakumov, A. M.; Tarascon, J.-M. Exploring the bottlenecks of anionic redox in Li-rich layered sulfides. *Nat. Energy* **2019**, *4*, 977–987.

[29] Batchelor, R. J.; Einstein, F. W. B.; Jones, C. H. W.; Fong, R.; Dahn, J. R. Crystal structure of Li_2FeS_2. *Phys. Rev. B* **1988**, *37*, 3699–3702.

[30] Hansen, C. J.; Zak, J. J.; Martinolich, A. J.; Ko, J. S.; Bashian, N. H.; Kaboudvand, F.; Van der Ven, A.; Melot, B. C.; Nelson Weker, J.; See, K. A. Multielectron, Cation and Anion Redox in Lithium-Rich Iron Sulfide Cathodes. *J. Am. Chem. Soc.* **2020**, *142*, 6737–6749.

[31] Lim, H.; Kim, S.-C.; Kim, J.; Kim, Y.-I.; Kim, S.-J. Structure of Li_5AlS_4 and comparison with other lithium-containing metal sulfides. *J. Solid State Chem.* **2018**, *257*, 19–25.

[32] Leube, B. T.; Inglis, K. K.; Carrington, E. J.; Sharp, P. M.; Shin, J. F.; Neale, A. R.; Manning, T. D.; Pitcher, M. J.; Hardwick, L. J.; Dyer, M. S.; Blanc, F.; Claridge, J. B.; Rosseinsky, M. J. Lithium Transport in $Li_{4.4}M_{0.4}M'_{0.6}S_4$ (M = Al^{3+}, Ga^{3+}, and M' = Ge^{4+}, Sn^{4+}): Combined Crystallographic, Conductivity, Solid State NMR, and Computational Studies. *Chem. Mater.* **2018**, *30*, 7183–7200.

[33] Gamon, J.; Duff, B. B.; Dyer, M. S.; Collins, C.; Daniels, L. M.; Surta, T. W.; Sharp, P. M.; Gaultois, M. W.; Blanc, F.; Claridge, J. B.; Rosseinsky, M. J. Computationally Guided Discovery of the Sulfide Li_3AlS_3 in the Li–Al–S Phase Field: Structure and Lithium Conductivity. *Chem. Mater.* **2019**, *31*, 9699–9714.

[34] Gamon, J.; Dyer, M. S.; Duff, B. B.; Vasylenko, A.; Daniels, L. M.; Zanella, M.; Gaultois, M. W.; Blanc, F.; Claridge, J. B.; Rosseinsky, M. J. $Li_{4.3}AlS_{3.3}Cl_{0.7}$: A Sulfide–Chloride Lithium Ion Conductor with Highly Disordered Structure and Increased Conductivity. *Chem. Mater.* **2021**, *33*, 8733–8744.

[35] Fasiska, E. J. Some defect structures of iron sulfide. *Phys. Status Solidi A* **1972**, *10*, 169–173.

[36] Baker, M. L.; Mara, M. W.; Yan, J. J.; Hodgson, K. O.; Hedman, B.; Solomon, E. I. *K*- and *L*-edge X-ray absorption spectroscopy (XAS) and resonant inelastic X-ray scattering (RIXS) determination of differential orbital covalency (DOC) of transition metal sites. *Coord. Chem. Rev.* **2017**, *345*, 182–208.

[37] Glaser, T.; Hedman, B.; Hodgson, K. O.; Solomon, E. I. Ligand *K*-Edge X-ray Absorption Spectroscopy: A Direct Probe of Ligand-Metal Covalency. *Acc. Chem. Res.* **2000**, *33*, 859–868.

[38] Huang, Y. et al. Integrated rocksalt–polyanion cathodes with excess lithium and stabilized cycling. *Nat. Energy* **2024**, 1–9.

[39] Barker, J.; Kendrick, E. Lithium-Containing Transition Metal Sulphide Compounds. 2010.

[40] Toby, B. H.; Von Dreele, R. B. GSAS-II: the genesis of a modern open-source all purpose crystallography software package. *J. Appl. Crystallogr.* **2013**, *46*, 544–549.

[41] Momma, K.; Izumi, F. VESTA 3 for three-dimensional visualization of crystal, volumetric and morphology data. *J. Appl. Crystallogr.* **2011**, *44*, 1272–1276.

[42] Tarascon, J. M.; Guyomard, D. New electrolyte compositions stable over the 0 to 5 V voltage range and compatible with the $Li_{1+x}Mn_2O_4$/carbon Li-ion cells. *Solid State Ion.* **1994**, *69*, 293–305.

[43] Ravel, B.; Newville, M. ATHENA, ARTEMIS, HEPHAESTUS: data analysis for X-ray absorption spectroscopy using IFEFFIT. *J. Synchrotron Radiat.* **2005**, *12*, 537–541.

Chapter 3

CAPACITY LIMIT DETERMINANTS OF $Li_{2+y}Al_yFe_{1-2y}S_2$ CATHODES

Patheria, E. S.; Guzman, P.; Soldner, L. S.; Qian, M. D.; Morrell, C. T.; Kim, S. S.; Hunady, K.; Priesen Reis, E. R.; Dulock, N. V.; Neilson, J. R.; Nelson Weker, J.; Fultz, B.; See, K. A. High-Energy Density Li-Ion Battery Cathode Using Only Industrial Elements. *J. Am. Chem. Soc.* **2025**, *147*, 9786–9799.

ABSTRACT

While the previous chapter described the multielectron redox mechanism in $Li_{2+y}Al_yFe_{1-2y}S_2$ cathodes, it remains unclear how redox-inactive Al^{3+} promotes greater extents of anion redox. Here, we show that Al^{3+} enables deeper delithiation by stabilizing the delithiated state. In the case of Li_2FeS_2, the thermodynamically favored state of the hypothetically fully oxidized material is pyrite FeS_2, which consists entirely of Fe^{2+} and persulfides $(S_2)^{2-}$. This suggests that S^{2-} can reduce $Fe^{>2+}$, thereby destabilizing delithiated $Li_{2-x}FeS_2$, which contains some $Fe^{>2+}$. Consistent with this, annealing $Li_{2-x}FeS_2$ leads to pyrite formation. In contrast, Al^{3+} substitution suppresses this phase transition by introducing Al_2FeS_4, a phase structurally similar to the pristine fully lithiated material, into the phase space of the hypothetically fully oxidized system. This alternative phase transition suppresses FeS_2 formation, thereby stabilizing deep delithiation and greater degrees of oxidation. This mechanistic insight offers a design principle for stabilizing deep anion redox and thus developing scalable, next-generation Li-ion battery cathodes.

3.1 Introduction

While the Fe and S K-edge XAS confirm greater S redox capacity in $Li_{2.2}Al_{0.2}Fe_{0.6}S_2$ than in Li_2FeS_2, the critical question of *why* remains unanswered. We rule out the higher Li^+ content of $Li_{2.2}Al_{0.2}Fe_{0.6}S_2$ as the reason, since $Li_{2.4}Al_{0.4}Fe_{0.2}S_2$ has even more Li^+ but no greater S redox capacity. Moreover, this reasoning would imply a higher total cation content in the charged state for $Li_{2.2}Al_{0.2}Fe_{0.6}S_2$ than Li_2FeS_2, which is not the case (see Supplementary Note S5). As previously discussed, a key challenge in developing cathodes that access anion redox is stabilizing the delithiated, oxidized state. When evaluating the capacity limits of multielectron redox cathodes, considering the most thermodynamically stable structure of the fully oxidized/delithiated material offers insights into the relative stability of the electrochemically oxidized/delithiated state. Hypothetically, fully delithiated Li_2FeS_2 would yield FeS_2, which has the thermodynamically stable pyrite structure that features octahedral Fe^{2+} and all $(S_2)^{2-}$.[1] Thus, we hypothesize that as deep delithiation approaches the FeS_2 stoichiometry, electrochemically oxidized $Fe^{2+/3+}$ becomes unstable alongside remaining S^{2-} compared to Fe^{2+} and $(S_2)^{2-}$. However, the phase transition to FeS_2 requires major structural changes, kinetically trapping the electrochemically oxidized material. As more persulfides form during charge, the stoichiometry and overall oxidation states approach pyrite FeS_2, and we hypothesize that the kinetic stabilization eventually fails, causing the voltage to polarize before full delithiation.

3.2 Results and discussion

Stability of $Li_{2-x}FeS_2$ and $Li_{2.2-x}Al_{0.2}Fe_{0.6}S_2$

We now consider the thermodynamically stable structure of fully delithiated $Li_{2.2}Al_{0.2}Fe_{0.6}S_2$, i.e., '$Al_{0.2}Fe_{0.6}S_2$'. There is no reported Al-Fe-S ternary material with the composition $Al_{0.2}Fe_{0.6}S_2$ (i.e., '$AlFe_3S_{10}$'). Thus, to determine the thermodynamically stable configuration of $Al_{0.2}Fe_{0.6}S_2$, we attempt the solid state reaction of Al, Fe, and S in the stoichiometric ratio of $Al_{0.2}Fe_{0.6}S_2$ at 900 °C. We quantify the phases in the reaction product by XRD and Rietveld analysis, shown in Figure S12. The pattern is well described by a fit to three separate phases: pyrite FeS_2[1] (51.1 wt%), 'Fe-deficient' FeS Fe_7S_8[2] (10.6 wt%), and the Al-Fe-S ternary Al_2FeS_4[3–5] (38.3 wt%). Although the majority phase is still FeS_2, the formation of Al_2FeS_4 shows that the thermodynamic state of hypothetical fully delithiated $Li_{2.2}Al_{0.2}Fe_{0.6}S_2$ includes an Al-Fe-S ternary, rather than separate Fe-S and Al-S binaries. We hypothesize that as $Fe^{2+/3+}$ with S^{2-} becomes increasingly unstable upon deep delithiation of

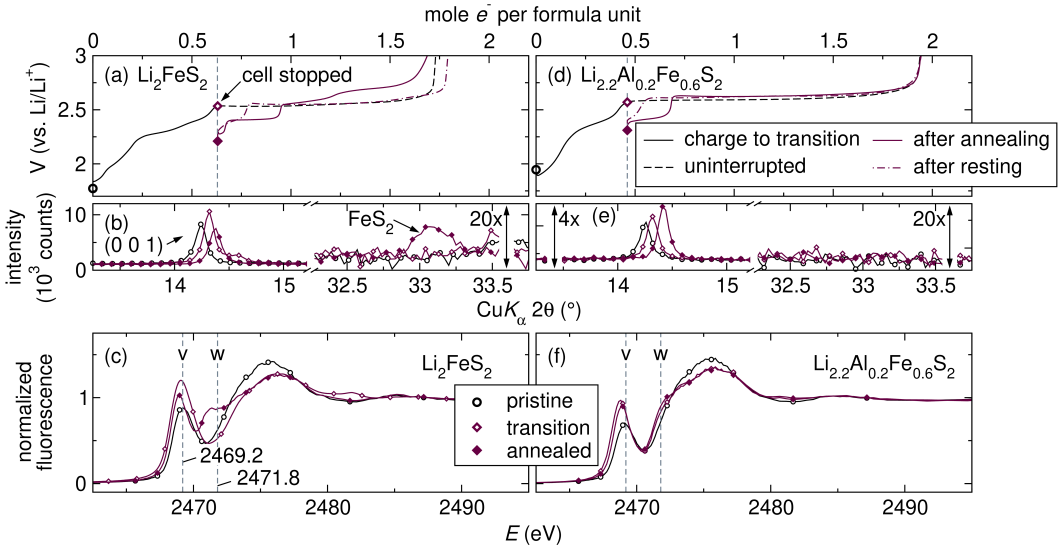

Figure 3.1: (a) Charge curves of Li_2FeS_2 up to the transition point, after which the cell is stopped, disassembled, the cathode is rinsed in DMC, dried in vacuum, annealed at 200 °C under static vacuum (≈50 mTorr) for 2 hours, or rested under the same vacuum conditions for ≈1 week, and then assembled in a new cell for galvanostatic cycling. The standard galvanostatic cycling charge curve for uninterrupted cycling is indicated by the black, dashed line in panel (a). (b) *Ex-situ* XRD of Li_2FeS_2 focused on the 2θ ranges for the (0 0 1) reflection, and the (2 0 0) reflection of pyrite FeS_2 in the pristine, transition, and annealed states. (c) S K-edge XAS spectra of Li_2FeS_2 in the pristine, transition, and annealed states. As before in Figure 2.5, the dashed lines in panel (c) indicate the two pre-edge features v and w, at 2469.2 eV and 2471.8 eV, respectively. Panels (d), (e), and (f), respectively, indicate the same corresponding data for $Li_{2.2}Al_{0.2}Fe_{0.6}S_2$.

$Li_{2.2}Al_{0.2}Fe_{0.6}S_2$, phase transitions to both FeS_2 and Al_2FeS_4 co-exist and compete. Importantly, Al_2FeS_4 crystallizes in the $P\bar{3}m1$ trigonal space group with an HCP sulfide anion framework and cations in octahedral edge-sharing and tetrahedral corner-sharing sites,[3–5] similar to $Li_{2+y}Al_yFe_{1-2y}S_2$ materials with HCP-like anion frameworks and analogous cation sites (Figure S13). Thus, the hypothetical phase transition to Al_2FeS_4 requires far less structural reorganization than converting to pyrite. We hypothesize that this stabilizes $Fe^{2+/3+}$ alongside S^{2-} by suppressing the phase transition to FeS_2, delaying the associated voltage polarization capacity limit and enabling greater anion oxidation in $Li_{2.2}Al_{0.2}Fe_{0.6}S_2$.

To assess the relative thermodynamic and kinetic stabilities of delithiated $Li_{2-x}FeS_2$ and $Li_{2.2-x}Al_{0.2}Fe_{0.6}S_2$, we conduct annealing and resting experiments. For both experiments, we charge the cathode to the transition SOC, stop the cell, remove and rinse the cathode, then either anneal it in an evacuated ampule (≈50 mTorr) at

200 °C for 2 hours or rest it at room temperature under the same static vacuum for ≈1 week, and finally reassemble a new cell with the annealed or rested cathode. At the transition point, 'exposed' S $3p$ nonbonding states would have been oxidized if charging had continued. Thus, annealing/resting at the transition SOC reveals the thermodynamic/kinetic stability of these exposed S $3p$ nonbonding states relative to empty Fe-S $3d$-$3p$ states (or vice versa).

The galvanostatic data from the annealing and resting experiments, along with XRD and S K-edge XAS are shown in Figure 3.1. The charge curves after annealing and resting Li_2FeS_2 charged to the transition point are shown in Figure 3.1a. After annealing, the OCV decreases by ≈0.32 V from the transition SOC, with new, distinct plateaus in the charge curve. After resting, the OCV decreases by ≈0.26 V, and the charge curve of the rested cathode shows a new Fe oxidation-like slope followed by a S oxidation plateau, suggesting $Fe^{2+/3+}$ can be reduced by S^{2-} even without heat. Combustion analysis (Table S6) shows S loss of ≈0.6 wt% after annealing, which is negligible and too low to explain the changes in the electrochemistry. To check for structural changes and FeS_2 formation after annealing, we compare *ex-situ* XRD of Li_2FeS_2 in the pristine, transition, and annealed states (Figure 3.1b). After annealing, we observe reduced (0 0 1) intensity for Li_2FeS_2, indicating lower crystallinity, and ≈17 wt% FeS_2 determined by Rietveld refinement (Figure S14a). The formation of FeS_2 is evident from its (2 0 0) reflection at ≈33.1 2θ. The FeS_2 formation shows that the S $3p$ nonbonding states are unstable relative to empty Fe-S $3d$-$3p$ states. We confirm the presence of $(S_2)^{2-}$ by S K-edge XAS of the annealed cathode, observing intensity at the previously noted pre-edge feature w (Figure 3.1c). Thus, electrochemically oxidized $Li_{2-x}FeS_2$ ($x \approx 0.58 \pm 0.05$) is a kinetically stabilized, metastable phase. During annealing, it loses crystallinity, converts to FeS_2, and forms persulfides. After resting at room temperature, Fe appears reduced but without incurring structural changes.

We now discuss the same experiments for $Li_{2.2}Al_{0.2}Fe_{0.6}S_2$. The charge curves after annealing and resting $Li_{2.2}Al_{0.2}Fe_{0.6}S_2$ charged to the transition point are shown in Figure 3.1d. After annealing, the OCV decreases by ≈0.26 V, a smaller decrease than in Li_2FeS_2, with the S oxidation plateau unaltered except for a small initial Fe oxidation-like feature. After resting, the OCV decreases by ≈0.23 V, almost matching the OCV after annealing, again with the S oxidation plateau unaltered and an even smaller initial Fe oxidation-like feature. This similarity suggests that the 200 °C relaxation process is an accelerated version of the room temperature process.

Combustion analysis shows no S loss (Table S6). XRD (Figure 3.1e) shows that in the annealed state, unlike Li_2FeS_2, the (0 0 1) intensity increases, indicating higher crystallinity, with no impurities in the Rietveld refinement (Figure S14b). S K-edge XAS confirms the absence of persulfides in the annealed cathode, with no new intensity at the pre-edge feature *w* (Figure 3.1f). Although $Li_{2.2-x}Al_{0.2}Fe_{0.6}S_2$ ($x \approx 0.46 \pm 0.02$) is kinetically stabilized, conversion to FeS_2 is suppressed during annealing, with similar changes after both annealing and resting. Thus, the annealed and relaxed states of $Li_{2.2-x}Al_{0.2}Fe_{0.6}S_2$ ($x \approx 0.46 \pm 0.02$) are much more similar than in $Li_{2-x}FeS_2$ ($x \approx 0.58 \pm 0.05$).

Electronic and local structure of Fe in $Li_{2-x}FeS_2$ and $Li_{2.2-x}Al_{0.2}Fe_{0.6}S_2$

The annealing experiments strongly suggest that the instability of the delithiated materials is associated with empty Fe-S $3d$-$3p$ states. Li_2FeS_2 undergoes formal charge transfer from S^{2-} to $Fe^{\gtrapprox 2.6+}$, yielding Fe^{2+} and $(S_2)^{2-}$ in FeS_2, while $Li_{2.2}Al_{0.2}Fe_{0.6}S_2$ shows an Fe oxidation-like voltage response, suggesting Fe is reduced during annealing and re-oxidized during charge. Fe K-edge XAS confirms formal Fe reduction in both annealed materials (Supplementary Note S3 and Figure S9). For $Li_{2.2}Al_{0.2}Fe_{0.6}S_2$, this raises the question of the electron source for Fe reduction since persulfide formation is not observed. We suggest that the charge compensation is similar to that in Fe-deficient Fe_7S_8 relative to FeS, where it's unclear whether the extra positive charge in Fe_7S_8 is Fe-based ($Fe_2^{3+}Fe_5^{2+}S_8^{2-}$),[6] S-based ($Fe_7^{2+}S_6^{2-}S_2^{-}$),[7] or some combination of both.[8, 9]

We use Mössbauer spectrometry and Fe K-edge extended X-ray absorption fine structure (EXAFS) analysis, which are sensitive probes of the electronic and local structure of Fe, to evaluate the stability of Li_2FeS_2 and $Li_{2.2}Al_{0.2}Fe_{0.6}S_2$ at all SOCs, including materials annealed after charging to the transition point. In Figure 3.2, the Mössbauer isomer shift, reflecting Fe $3d$ state occupancy, and the first shell coordination number *N* from Fe K-edge EXAFS, representing the average number of nearest S atoms coordinating Fe, are plotted because they show the greatest differences between Li_2FeS_2 and $Li_{2.2}Al_{0.2}Fe_{0.6}S_2$, elucidating the role of Al^{3+}. The Mössbauer isomer shifts and quadrupole splittings can be found in Figure S15, with each fitted spectrum in Figures S16 and S17, and all fit parameters in Table S7. Each Mössbauer spectrum is fit with four distinct Fe sites, and the weighted average isomer shift and its weighted standard deviation for each spectrum are plotted in Figure 3.2a,d. A larger weighted standard deviation in the isomer shift reflects a wider spread among the four Fe sites used to fit each spectrum. The EXAFS first

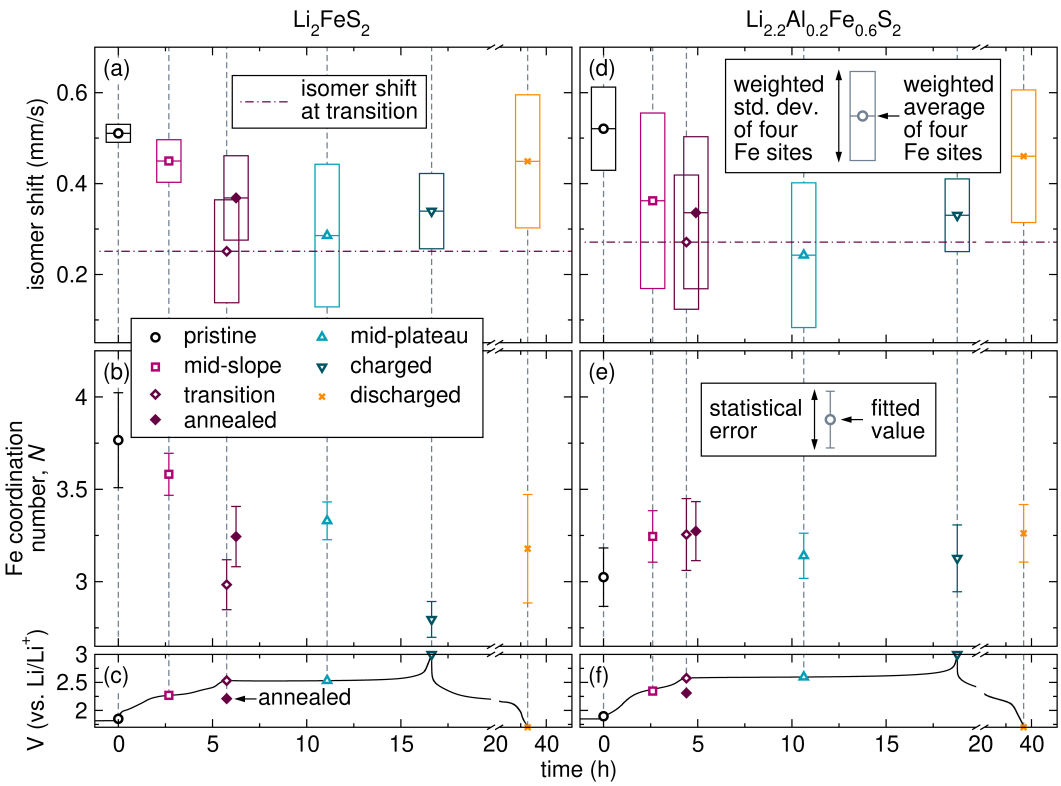

Figure 3.2: (a) The weighted averages and corresponding weighted standard deviations of the isomer shifts of the four Lorentzian doublets used to fit *ex-situ* Mössbauer spectra of Li_2FeS_2 at various SOCs. (b) The coordination number N of the first shell correlations, representing the average number of nearest S atoms coordinating Fe, extracted from EXAFS fits for Li_2FeS_2 at various SOCs. (c) The representative galvanostatic data showing the SOC for each data point. Panels (d), (e), and (f) indicate the same corresponding data, respectively, for $Li_{2.2}Al_{0.2}Fe_{0.6}S_2$. In panels (a) and (d), the weighted average is indicated by the symbol, and the weighted standard deviation is indicated by height of the box accompanying the symbol. The dotted/dashed dark purple horizontal line in panels (a) and (d) indicates the weighted average isomer shift at the transition SOC.

and second shell $r_{\text{eff.}}$ and N are shown in Figure S18, with the fitted $\chi(k)$ and $|\chi(R)|$ in Figures S19 and S20 and Figures S21 and S22, respectively, and all fit parameters in Table S8.

First, we discuss the Li_2FeS_2 isomer shifts and N in Figure 3.2a and b, with corresponding galvanostatic data (Figure 3.2c). The weighted average isomer shift decreases during the sloping region, which is consistent with Fe oxidation, and increases during discharge, consistent with Fe reduction. However, the average isomer shift unexpectedly increases during the S oxidation plateau, which is highlighted by the dotted/dashed line marking the average isomer shift at the transition point. The increase, confirmed by the spectral centroids (Figure S23a,b), indicates a counterintuitive global Fe 'reduction' despite the $\approx 1.09 \pm 0.01$ e^- oxidation. A Mössbauer study in 1987 also observed this increase but did not explain it.[10] Covalency differences between $(S_2)^{2-}$ and S^{2-} cannot explain the increase, as $(S_2)^{2-}$, being more covalent (see Supplementary Note S6), would decrease, not increase, the isomer shift. Fe^{3+} reduction can occur when S^{2-} is present, even without formal $2\,S^{2-}/(S_2)^{2-}$ oxidation, as shown by the annealing experiment with $Li_{2.2}Al_{0.2}Fe_{0.6}S_2$, and suggested by the resting experiments with both materials. Thus, we deduce that the increase indicates genuine Fe^{3+} reduction in the *ex-situ* samples, which Mössbauer spectrometry is sensitive enough to detect.[11–13] Simultaneously, N decreases during charge, with $N \lessapprox 3$ indicating Fe distorts towards the basal face of the FeS_4 tetrahedron in the charged state, before tending towards the pristine state in the discharged state. The data in the annealed state are shown, but conclusions are avoided due to convolution from FeS_2. The samples are measured *ex-situ* ≈24 hours after cell disassembly and thus have time to relax, and so effectively represent the "rested" state discussed previously. Thus, the Fe reduction and distortion towards the FeS_4 tetrahedron basal face together characterize the kinetic relaxation mechanism at deep delithiation levels. The greater relaxation – that is, increasingly reduced and distorted Fe – with deeper delithiation, shows that empty Fe-S $3d$-$3p$ states indeed become increasingly unstable.

Next, we discuss the $Li_{2.2}Al_{0.2}Fe_{0.6}S_2$ isomer shifts and N in Figure 3.2d and e, with corresponding galvanostatic data (Figure 3.2f). The isomer shift largely mirrors Li_2FeS_2, with a notable difference at the mid-plateau SOC. Instead of the continuous increase during the S oxidation plateau observed for Li_2FeS_2, the isomer shift decreases slightly at the mid-plateau before increasing again at the charged state. This non-monotonicity, confirmed by the spectral centroids (Figure S23c,d),

is highlighted by the dotted/dashed line once again marking the average isomer shift at the transition point. In Li_2FeS_2, the continuous increase reveals that empty Fe-S $3d$-$3p$ states grow more unstable with delithiation. Conversely, the decrease at the mid-plateau in $Li_{2.2}Al_{0.2}Fe_{0.6}S_2$ reveals that the empty states have slightly greater stability at this SOC than in Li_2FeS_2. Correspondingly, N stays mostly constant, with Fe near the base at all SOCs, even in the annealed state. The similarity of N in the annealed and transition states extends the previously observed similarity of these states in $Li_{2.2}Al_{0.2}Fe_{0.6}S_2$ from bulk probes to the local structure of Fe. We suggest that Al^{3+} stabilizes N by exerting electrostatic forces on the anion framework, preventing Fe from distorting within the FeS_4 tetrahedron. In the charged state, the isomer shift of $Li_{2.2}Al_{0.2}Fe_{0.6}S_2$ (0.330 ±0.080 mm/s) closely matches that of Li_2FeS_2 (0.339 ±0.083 mm/s), with N also showing slight distortion towards the base. This suggests that, once the capacity limit is reached at full charge, empty Fe-S $3d$-$3p$ states in both materials become similarly unstable.

3.3 Conclusion

Substituting Al^{3+} into Li_2FeS_2 not only makes the material lighter, increasing gravimetric capacity, but also increases anion oxidation capacity in mole e^- per f.u. Anion oxidation capacity increases because Al^{3+} stabilizes the electrochemically oxidized material, which requires kinetic stabilization to prevent the formation of more thermodynamically stable products like pyrite FeS_2. We assess kinetic stability from electronic and structural perspectives. Electronically, we evaluate how Al^{3+} alters the propensity for S^{2-} to reduce $Fe^{\gtrapprox 2.6+}$ in the electrochemically oxidized material. Upon annealing, oxidized Li_2FeS_2 shows Fe^{2+} formation through ligand to metal charge transfer that forms persulfides and pyrite FeS_2, whereas $Li_{2.2}Al_{0.2}Fe_{0.6}S_2$ shows Fe^{3+} reduction that preserves crystallinity without forming persulfides. This difference translates to more stable empty Fe-S $3d$-$3p$ states in deeply delithiated $Li_{2.2}Al_{0.2}Fe_{0.6}S_2$ than Li_2FeS_2, revealed by Mössbauer spectrometry. Structurally, Al^{3+} stabilizes the Fe local structure. Importantly, the introduction of Al expands the phase space of thermodynamically stable phases of the oxidized stoichiometries. Al_2FeS_4, for instance, is structurally very similar to $Li_{2.2}Al_{0.2}Fe_{0.6}S_2$ and therefore likely aids in the stability against conversion to pyrite. Thus, incorporating Al^{3+} addresses one of the key challenges in developing multielectron redox cathodes: stabilizing the highly delithiated state against phase transitions to more stable phases.

3.4 Experimental

All methods are identical to those in the previous chapter, except for additional methods described below.

Synthesis of $Al_{0.2}Fe_{0.6}S_2$

The material and precursors were handled in an Ar-filled glovebox. Powders of Al (Alfa Aesar, 99.5%), Fe (Acros Organics, 99.0%), and S_8 (Acros Organics, >99.5%) were weighed to an accuracy of ±0.1 mg to give total 250 mg of $Al_{0.2}Fe_{0.6}S_2$ and then hand-mixed in an agate mortar and pestle. The mixed precursor powders were pressed into $\frac{1}{4}$ inch diameter cylindrical pellets with a hand-operated arbor press. The mixed precursor pellet was gray in color. The pellet was placed inside a vitreous silica ampule (10 mm i.d., 12 mm o.d.), evacuated to ≤ 50 mTorr, and sealed with a methane-oxygen torch without exposure to air. The evacuated and sealed ampule was then placed inside a box furnace and heated at 1 °C/min to 900 °C with a dwell time of 12 h. After ambient cooling to room temperature (roughly at a rate of 1 °C/min), the ampule was opened inside the glovebox. The pellet after heating was a glittery dark gray color and fully melted, conforming to the shape of the ampule with slight bright yellow S residue stuck to the sides of the ampule.

Ex-situ annealing and resting

For annealing and resting experiments, the cathode was first charged to the transition SOC. The cell was then stopped and disassembled in an Ar-filled glovebox, and the cathode was removed and rinsed as previously described. The intact cathode was then placed in vitreous silica ampules (10 mm i.d., 12 mm o.d.), evacuated to ≤ 50 mTorr, and sealed with a methane-oxygen torch without exposure to air. For annealing experiments, the cathode in the evacuated ampule was placed inside a box furnace and then heated at 1 °C/min to 200 °C, then annealed at 200 °C for 2 hours, and then ambiently cooled to room temperature by shutting off the furnace. For resting experiments, the cathode in the evacuated ampule was kept at room temperature for ≈1 week. The ampule containing the annealed or rested cathode was then opened inside an Ar-filled glovebox, and a new cell was assembled as previously described with the annealed or rested cathode.

Mössbauer sample preparation and measurement

Ex-situ samples for Mössbauer spectrometry were initially prepared as previously described. The cathode was kept intact and placed on a small piece of Kapton tape

(1 mil film thickness, 2.5 mil total thickness, Uline). The Kapton tape was adhered to the inside of a static shielding bag (3 mil thickness, Uline) and sealed in Ar with an impulse heat sealer (Uline). The cathode itself is ≈100 μm thick. The sample, sealed in the bag, was encapsulated between Pb apertures with 5.5 mm openings to prevent excess background γ rays from reaching the Mössbauer detector, and held in place with Scotch tape such that the 5.5 mm hole revealed only the cathode. The Mössbauer spectra were acquired at room temperature, in transmission geometry, in the constant acceleration mode of a Wissel 1200 spectrometer and with a ^{57}Co(Rh) γ-ray source (Ritverc MCo7.123) with an activity of ≈19 mCi. The thickness of the samples (in mg of natural Fe per cm^2) was about 3 to 4.4 mg·cm^{-2}. The velocity scale (±3 mm/s) was calibrated at room temperature with a 30 μm thick α-Fe foil (99.99+% purity). Each spectrum was acquired for ≈24 hours.

Mössbauer fitting

We use the MossA program to fit the Mössbauer spectra.[15] We show the Mössbauer spectra of Li_2FeS_2 and $Li_{2.2}Al_{0.2}Fe_{0.6}S_2$ at each SOC in Figure S16 and Figure S17, respectively. Each spectrum is shown with the accompanying fit, each fit component/Fe site, and difference between the fit and the data. Each spectrum is fit with four symmetric Lorentzian doublets representing four separate Fe sites. Each doublet has four fit parameters: (1) the isomer shift , the center point between the two peaks of the doublet, (2) the quadrupole splitting, the separation between the peaks, (3) the peak full width half maximum/the linewidth (Γ), and (4) the percent area value (related to the peak intensity scaled by $\pi\Gamma$). The fitted values of all parameters for each spectrum are tabulated in Table S7. We use 4 separate Fe sites to achieve realistic linewidths for each Lorentzian doublet fit component and to reflect the actual variety of the possible coordination environments of Fe in the materials. We use a nested configuration of the Lorentzian doublets in our fits where possible, over a staggered configuration, as the nested fit better reflects the electron delocalization we expect in the materials.[16] In every fit, we constrain the linewidths of all doublets to be equal in order to reduce free parameters and simplify interpretation. We verify the isomer shift trends from our fits using spectral centroid analysis. The centroids of the spectra in Figures S16 and S17 are calculated as: centroid = $\frac{\sum_i I(v_i)\cdot v_i}{\sum_i I(v_i)}$, where $I(v_i)$ is the normalized absorption intensity, v_i is the velocity, and i indexes the data points. The centroids are shown in Figure S23 with the isomer shift data. Since the centroids are calculated directly from the raw data without fitting parameters, they provide direct access to the isomer shift. They fol-

low the same trend as the weighted average isomer shifts from our fits, confirming that the fits accurately represent the data and are unbiased.

Fe K-edge EXAFS fitting

We use the Athena and Artemis software from the IFEFIT suite for Fe K-edge EXAFS fitting.[14] In Fe K-edge XAS, oscillations at energies beyond the primary electronic transition arise from the interference of the excited photoelectron with itself after scattering off neighboring atoms.[17] The oscillations are converted to a function of the wave number, $\chi(k)$, which is then Fourier transformed to real space ($|\chi(R)|$). The $\chi(k)$ are fit within a k window of roughly ≈3.0±0.1 to ≈10±1 Å^{-1} (sample dependent), with dk=2 Å^{-1}. The $|\chi(R)|$ are fit within an R window of roughly ≈1.1±0.1 to ≈10 Å (sample dependent), with dR=0.2 Å. The amplitude reduction factor S_0^2 is held fixed for all *ex-situ* samples and is determined by fitting the first shell of the $\chi(k)$ and $|\chi(R)|$ of the Fe calibration foil, using a k window of 5 to 11 Å^{-1} (dk = 2 Å^{-1}) and R window of 1 to 3 Å (dR = 2 Å). The intensity of the Fourier transform, $|\chi(R)|$, represents the oscillation intensity in real space, corresponding to correlation shells, with Fe located at 0 Å. We fit the first and second shell correlations with defined scattering paths and determine the correlation distance, $r_{\text{eff.}}$ (Å), and the coordination number N. The first shell describes the immediate coordination of Fe by S, and the second shell describes the nearest neighbor cations at the edge-sharing tetrahedral sites closest to a given Fe. For Li_2FeS_2, we model the second shell with only Fe, as the scattering probability off of Li^+ is very low because of its small electron cloud. For $Li_{2.2}Al_{0.2}Fe_{0.6}S_2$, although the Al^{3+} electron cloud is nonnegligible, we still model the second shell with only Fe because the low Al content (0.2 mole Al^{3+} per f.u.) minimizes the scattering probability. The EXAFS analysis is conducted at all of the previously described SOCs. The resolution of our EXAFS data (the oscillations $\gtrsim$50 eV above the rising edge), limits us to fitting both the first and second shells using only single scattering paths. This captures overall changes but not specific atomic positions or heterogeneity thereof. For example, the first shell actually includes 4 separate S atoms, each with its own scattering path, but we fit the first shell with a single scattering path, capturing the average effect of the multiple S atoms through the coordination number N. The EXAFS first and second shell $r_{\text{eff.}}$ and N are shown in Figure S18, with the fitted $\chi(k)$ and $|\chi(R)|$ in Figures S19 and S20 and Figures S21 and S22, respectively, and all fit parameters in Table S8.

3.5 Funding and user-facility acknowledgments

This material is based upon work supported by the National Science Foundation (NSF) under Award No. DMR-2340864. K.A.S. acknowledges support from the Packard Fellowship for Science and Engineering, the Alfred P. Sloan Foundation, and the Camille and Henry Dreyfus Foundation. E.S.P. acknowledges support from the Robert and Patricia Switzer Foundation. E.S.P., M.D.Q., and C.T.M. acknowledge NSF Graduate Research Fellowship support under Award No. DGE-2139433. B.F. and P.G. acknowledge support from NSF Award No. DMR-1904714. Initial work on this material was partially supported by the Center for Synthetic Control Across Length-scales for Advancing Rechargeables (SCALAR), an Energy Frontier Research Center funded by the U.S. Department of Energy, Office of Science, Basic Energy Sciences under award no. DE-SC0019381. This research used beam lines 2-2 and 4-3 at the Stanford Synchrotron Radiation Lightsource (SSRL). Use of SSRL, SLAC National Accelerator Laboratory, is supported by the U.S. Department of Energy, Office of Science, Office of Basic Energy Sciences under Contract No. DE-AC02-76SF00515. This research used beam lines 8-BM and 28-ID-1 of the National Synchrotron Light Source II (NSLS-II), a U.S. Department of Energy (DOE) Office of Science User Facility operated for the DOE Office of Science by Brookhaven National Laboratory (BNL) under Contract No. DE-SC0012704. The authors thank the Resnick Environmental Analysis Center at Caltech for ICP-MS and the Beckman Institute and Caltech X-ray Crystallography Facility for CuK_α XRD. The authors also thank Dr. Yonghua Du and Dr. Sarah Nicholas at 8-BM (NSLS-II) for their assistance with S K-edge XAS, Dr. Gihan Kwon at 28-ID-1 (NSLS-II) for his help with sXRD, and Dr. Erik Nelson and Dr. Matthew Latimer at 2-2 and 4-3 (SSRL) for their help with Fe K-edge XAS.

Bibliography

[1] Tokuda, M.; Yoshiasa, A.; Mashimo, T.; Arima, H.; Hongu, H.; Tobase, T.; Nakatsuka, A.; Sugiyama, K. Crystal structure refinement of $MnTe_2$, $MnSe_2$, and MnS_2: cation-anion and anion–anion bonding distances in pyrite-type structures. *Z. Kristallogr. Cryst. Mater.* **2019**, *234*, 371–377.

[2] Fleet, M. E. The crystal structure of a pyrrhotite (Fe_7S_8). *Acta Crystallogr. B* **1971**, *27*, 1864–1867.

[3] Nishida, K.; Narita, T. Some Experiments on the Formation of an Fe-Al Double Sulfide Compound. *Bull. Fac. Eng. Hokkaido Univ.* **1976**, *81*, 99–109.

[4] Menard, M. C.; Ishii, R.; Higo, T.; Nishibori, E.; Sawa, H.; Nakatsuji, S.; Chan, J. Y. High-Resolution Synchrotron Studies and Magnetic Properties of Frustrated Antiferromagnets MAl_2S_4 (M = Mn^{2+}, Fe^{2+}, Co^{2+}). *Chem. Mater.* **2011**, *23*, 3086–3094.

[5] Verchenko, V. Y.; Kanibolotskiy, A. V.; Bogach, A. V.; Znamenkov, K. O.; Shevelkov, A. V. Ferromagnetic correlations in the layered van der Waals sulfide $FeAl_2S_4$. *Dalton Trans.* **2022**, *51*, 8454–8460.

[6] Bin, M.; Pauthenet, R. Magnetic Anisotropy in Pyrrhotite. *J. Appl. Phys.* **1963**, *34*, 1161–1162.

[7] Gosselin, J. R.; Townsend, M. G.; Tremblay, R. J.; Webster, A. H. Mössbauer investigation of synthetic single crystal monoclinic Fe_7S_8. *Mater. Res. Bull.* **1975**, *10*, 41–49.

[8] Levinson, L. M.; Treves, D. Mössbauer study of the magnetic structure of Fe_7S_8. *J. Phys. Chem. Solids* **1968**, *29*, 2227–2231.

[9] Shimada, K.; Mizokawa, T.; Mamiya, K.; Saitoh, T.; Fujimori, A.; Ono, K.; Kakizaki, A.; Ishii, T.; Shirai, M.; Kamimura, T. Spin-integrated and spin-resolved photoemission study of Fe chalcogenides. *Phys. Rev. B* **1998**, *57*, 8845–8853.

[10] Blandeau, L.; Ouvrard, G.; Calage, Y.; Brec, R.; Rouxel, J. Transition-metal dichalcogenides from disintercalation processes. Crystal structure determination and Mossbauer study of Li_2FeS_2 and its disintercalates $Li_{2-x}FeS_2$ ($0.2 \leq x \leq 2$). *J. Phys. C: Solid State Phys.* **1987**, *20*, 4271.

[11] Goodenough, J. B.; Fatseas, G. Mössbauer ^{57}Fe isomer shift as a measure of valence in mixed-valence iron sulfides. *J. Solid State Chem.* **1982**, *41*, 1–22.

[12] Parish, R. V. In *Mössbauer Spectroscopy*; Dickson, D. P. E., Berry, F. J., Eds.; Cambridge University Press: Cambridge, 1986; pp 17–69.

[13] Fultz, B. *Characterization of Materials*; John Wiley & Sons, Ltd: New York, NY, 2011.

[14] Ravel, B.; Newville, M. ATHENA, ARTEMIS, HEPHAESTUS: data analysis for X-ray absorption spectroscopy using IFEFFIT. *J. Synchrotron Radiat.* **2005**, *12*, 537–541.

[15] Prescher, C.; McCammon, C.; Dubrovinsky, L. MossA: A Program for Analyzing Energy-Domain Mössbauer Spectra from Conventional and Synchrotron Sources. *J. Appl. Crystallogr.* **2012**, *45*, 329–331.

[16] Brown, A. C.; Thompson, N. B.; Suess, D. L. M. Evidence for Low-Valent Electronic Configurations in Iron–Sulfur Clusters. *J. Am. Chem. Soc.* **2022**, *144*, 9066–9073.

[17] Newville, M. Fundamentals of XAFS. *Rev. Mineral. Geochem.* **2014**, *78*, 33–74.

Chapter 4

$Cu^{>1+}$ DELOCALIZES MULTIELECTRON REDOX AND DETERMINES CAPACITY LIMITS IN $Li_{2.2-z}Cu_zAl_{0.2}Fe_{0.6}S_2$ CATHODES

Soldner, L. S.; Ramakrishnan, N. R.; Patheria, E. S.; Morrell, C. T.; Qian, M. D.; Davis, V. K.; See, K. A. $Cu^{>1+}$ Delocalizes Multielectron Redox and Determines Capacity Limits in Industrial Element Li-Ion Cathodes. *In preparation*.

This chapter is temporarily embargoed.

Chapter 5

CONCLUSION AND OUTLOOK FOR MULTIELECTRON REDOX INDUSTRIAL-ELEMENT LI-ION CATHODES

This thesis develops a thermodynamic and electronic framework for understanding energy storage in Li-ion cathodes and applies it to a new class of high-capacity, industrial-element sulfides. Beginning with a first-principles treatment of electrochemical potentials across battery components, Chapter 1 establishes the energetic basis for cell voltage, interfacial charge transfer, and charge compensation in electrochemical redox reactions. Chapter 2 introduces novel Li-rich sulfide cathodes, $Li_{2+y}Al_yFe_{1-2y}S_2$, which operate via multielectron redox and exhibit high extents of anion redox through the reversible formation and cleavage of S – S bonds associated with local structural distortions. Chapter 3 demonstrates that the stability of the delithiated phase is a key determinant of electrochemical redox capacity limits. Accordingly, it presents a core design framework. First, it hypothesizes that electrochemical delithiation competes with phase transitions to thermodynamically stable phases. Second, it establishes that these competing phase transitions are well-described by the thermodynamic configuration of the hypothetically fully delithiated phase. Consequently, it shows that the pristine material can be rationally designed to reflect the structural and electronic properties of the thermodynamic delithiated configuration, suppressing competing transitions and making deep delithiation electrochemically accessible. Chapter 4 expands the chemical space to include Cu in $Li_{2.2-z}Cu_zAl_{0.2}Fe_{0.6}S_2$, where unique Cu–S electronic interactions delocalize anion redox charge compensation beyond localized S – S bonds, improving reversibility. However, Cu also destabilizes the delithiated phase, limiting accessible capacity. As noted in the Conclusion of Chapter 4, these results establish a broad compositional space for future exploration with accompanying guiding design principles. This space is spanned by $Li_{2+y-z}Cu_zAl_yFe_{1-2y}S_2$, where $0 \leq y \leq 0.5$ and $0 \leq z \leq 1+y$, and may be even more broadly defined by structurally related end members: Li_2FeS_2, Li_5AlS_4, Al_2FeS_4, and $LiCuFeS_2$.

The cathodes presented in this thesis, despite their lower voltage, achieve gravimetric capacities and energy densities far beyond those of commercial oxides, and rely exclusively on industrially abundant elements with already-scaled, battery-grade supply chains. This raises a natural, important question: can these materials make

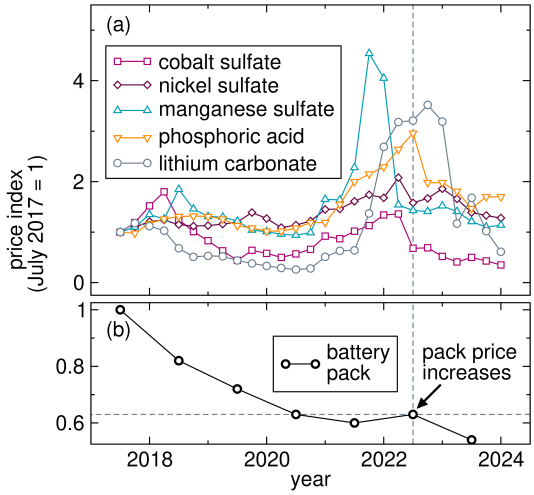

Figure 5.1: Indexed prices of Li-ion (a) key cathode raw materials and (b) battery packs from 2017 to 2024. All prices are normalized to July 2017. The spike in raw material costs in 2022 caused Li-ion pack prices to increase for the first time ever that same year, marked by the dashed gray lines.

a translational impact? As discussed in the introductions to Chapters 2 and 4, a $\gtrapprox$ 100× increase in deployed energy storage capacity is required by 2050 to meet net-zero targets. The biggest bottleneck is cathode raw material cost, which now accounts for over 40% of total Li-ion cell cost.[2, 3] Recent spikes in cathode raw material prices (Figure 5.1a) triggered the first-ever increase in Li-ion battery pack prices in 2022 (Figure 5.1b).[1] This marks a new era for Li-ion technology: manufacturing is now sufficiently advanced that raw materials costs can dominate finished-product battery pricing. Thus, cathodes composed of significantly cheaper and more scalable industrial elements could deliver a step-function drop in the cost of Li-ion batteries. Of course, well-established applications of Li-ion batteries in transport and energy infrastructure require competitive performance metrics beyond just high energy density, such as low capacity fade and high rate capability. However, while energy density is primarily an intrinsic materials property, many other performance metrics—especially those measured over many charge/discharge cycles—are optimized via electrode and electrolyte engineering techniques. Decades of optimizing commercial cathodes have yielded a mature toolbox of such techniques,[4] which can be applied to the materials presented in this thesis, as early efforts already suggest.[5] Thus, the cathodes in this thesis offer a compelling foundation: their intrinsic energy density is nearly unmatched, and with appropriate engineering, they could be developed into high-performance, scalable alternatives. This is precisely the kind of work I am most excited—and most grateful—to pursue as I defend this

thesis. It is my life's dream to live the words of Dr. Faulkner quoted in the Introduction to Chapter 1: to leverage electrochemistry to connect electrical energy and the material world, at both atomic and societal scales, in service of a more sustainable future and the eradication of energy poverty.

Bibliography

[1] Gül, T. Global EV Outlook 2024. *International Energy Agency* **2024**, https://www.iea.org/reports/global-ev-outlook-2024.

[2] Battery cathode prices rise for first time this year as lithium costs increase. *Benchmark Source* **2023**, https://source.benchmarkminerals.com/article/battery-cathode-prices-rise-for-first-time-this-year-as-lithium-costs-increase.

[3] The battery cell component opportunity in Europe and North America. *McKinsey & Company* **2024**, https://www.mckinsey.com/industries/automotive-and-assembly/our-insights/the-battery-cell-component-opportunity-in-europe-and-north-america.

[4] Xiao, J. et al. From laboratory innovations to materials manufacturing for lithium-based batteries. *Nat. Energy* **2023**, 329–339.

[5] Barker, J.; Kendrick, E. Lithium-Containing Transition Metal Sulphide Compounds. 2010.

SUPPLEMENTARY INFORMATION–CHAPTERS 2 AND 3

Supplementary Note S1: Previous work on Li_2FeS_2

Li_2FeS_2 has been studied for decades, first reported by Sharma in 1976[1] and then characterized as a cathode[2–7] and spectroscopically interrogated by Mössbauer[6–9], infrared[10], and X-ray absorption[7] all in the 1980s. Later, in 2008, Kendrick and coworkers revisited Li_2FeS_2 to develop a synthesis using the industrial Li precursor Li_2CO_3 rather than air-sensitive Li_2S used for traditional air-free solid state synthesis.[11] They then evaluated how Li_2FeS_2 performs versus a commercial graphite anode, showing an energy density of ≈740 Wh·kg^{-1} with a capacity fade of ≈1% per cycle over 70 cycles at $C/5$[12], and investigated the rate capability versus Li metal.[13] All prior mechanistic studies support distinct, sequential Fe^{2+} oxidation to $Fe^{2+/3+}$ followed by S^{2-} oxidation during charge. The mechanism of S^{2-} oxidation was suggested to be formation of $(S_2)^{2-}$ using IR data as evidence.[10] Later, we showed S K-edge X-ray absorption spectroscopy (XAS) data that definitively shows formation of $(S_2)^{2-}$ upon oxidation.[14] We refer to these processes henceforth as 'Fe oxidation' and 'S oxidation'. The electrochemical data suggests that the Fe and S oxidation capacities are ≈30 to 40% and ≈70 to 60% of the total multielectron redox capacity, respectively.[11–14] We also note that what we refer to as just 'Fe oxidation' actually involves removing electrons from covalent, mixed Fe-S electronic states, with clear involvement of S-based states that we previously showed computationally and experimentally.[14] We also determined that the Fe oxidation capacity is limited by an intrinsic stability limit of removing ≈0.5 to 0.6e$^-$ per formula unit from the mixed Fe-S states, after which anion redox proceeds from S-localized nonbonding $3p$ states, removing another ≈1 to 1.1 e$^-$ per formula unit (i.e., only ≈50% of the total S content participates in anion redox).[14, 15]

Table S1: Rietveld refinement results for sXRD patterns of Li_2FeS_2, $Li_{2.2}Al_{0.2}Fe_{0.6}S_2$, and $Li_{2.4}Al_{0.4}Fe_{0.2}S_2$ using the $P2_1/m$ monoclinic space group unit cell, corresponding to Figure 2.2a, b, and c, respectively.

All Rietveld refinement results														
	lattice parameters							atomic parameters						
	R_{wp} (%)	reduced χ^2	a (Å)	b (Å)	c (Å)	β (°)	V (Å^3)	atom label	Wyckoff site	x	y	z	occu-pancy	U_{iso}
Li_2FeS_2	16.8	549	6.786	7.790	6.292	89.97	332.669	S1	2e	-0.180	0.750	0.743	1.00	0.026
								S2	2e	0.162	0.750	0.257	1.00	0.009
								S3	4f	0.332	0.499	0.748	1.00	0.020
								Fe1	2e	0.189	0.750	0.638	0.56	0.020
								Fe2	4f	0.338	0.011	0.363	0.33	0.020
								Fe3	2e	0.147	0.250	0.620	0.78	0.020
								Li1	2e	0.189	0.750	0.638	0.44	0.015
								Li2	4f	0.338	0.011	0.363	0.67	0.014
								Li3	2e	0.147	0.250	0.620	0.22	0.018
								Li4	2e	0.500	0.750	0.000	1.00	0.027
								Li5	2a	0.000	0.000	0.000	1.00	0.028

continued on next page

continued from previous page

	lattice parameters							atomic parameters						
	R_{wp} (%)	reduced χ^2	a (Å)	b (Å)	c (Å)	β (°)	V (Å^3)	atom label	Wyckoff site	x	y	z	occu-pancy	U_{iso}
$Li_{2.2}Al_{0.2}Fe_{0.6}S_2$	15.0	2710	6.793	7.842	6.272	90.00	334.098	S1	2e	-0.140	0.750	0.756	1.00	0.018
								S2	2e	0.179	0.750	0.265	1.00	0.009
								S3	4f	0.316	0.504	0.750	1.00	0.016
								Al1	2e	0.169	0.750	0.628	0.40	0.000
								Fe1	2e	0.175	0.750	0.624	0.20	0.011
								Fe2	4f	0.343	0.006	0.372	0.33	0.018
								Fe3	2e	0.187	0.250	0.660	0.34	0.019
								Li1	2e	0.175	0.750	0.624	0.40	0.011
								Li2	4f	0.343	0.006	0.372	0.67	0.018
								Li3	2e	0.187	0.250	0.660	0.66	0.019
								Li4	2e	0.500	0.750	0.000	1.00	0.027
								Li5	2a	0.000	0.000	0.000	1.00	0.028

continued on next page

continued from previous page

	lattice parameters							atomic parameters						
	R_{wp} (%)	reduced χ^2	a (Å)	b (Å)	c (Å)	β (°)	V (Å^3)	atom label	Wyckoff site	x	y	z	occu-pancy	U_{iso}
$Li_{2.4}Al_{0.4}Fe_{0.2}S_2$	12.1	1332	6.806	7.892	6.241	89.85	335.229	S1	2e	-0.155	0.750	0.761	1.00	0.020
								S2	2e	0.187	0.750	0.264	1.00	0.026
								S3	4f	0.323	0.521	0.748	1.00	0.011
								Al1	2e	0.168	0.750	0.634	0.80	0.000
								Fe1	2e	0.165	0.750	0.634	0.16	0.014
								Fe2	4f	0.280	-0.002	0.377	0.06	0.087
								Fe3	2e	0.176	0.250	0.666	0.13	0.001
								Li1	2e	0.165	0.750	0.634	0.04	0.014
								Li2	4f	0.280	-0.002	0.377	0.94	0.087
								Li3	2e	0.176	0.250	0.666	0.87	0.001
								Li4	2e	0.500	0.750	0.000	1.00	0.027
								Li5	2a	0.000	0.000	0.000	1.00	0.028

Supplementary Note S2: Unfit reflections and superstructure in Li_2FeS_2 and $Li_{2.2}Al_{0.2}Fe_{0.6}S_2$

Some reflections for Li_2FeS_2 and $Li_{2.2}Al_{0.2}Fe_{0.6}S_2$ between 1 to 2 $Å^{-1}$ in Figure 2.2a and b are not described by the fits and are highlighted by asterisks (*). After checking many possible impurities (see Table S3), we suggest that the unfit reflections are likely superstructure peaks and/or indicative of multiple polymorphs present in our Li_2FeS_2 and $Li_{2.2}Al_{0.2}Fe_{0.6}S_2$ reaction products. The reflections in the same Q range for the highest Al content material $Li_{2.4}Al_{0.4}Fe_{0.2}S_2$ are all fit by the $P2_1/m$ unit cell, ostensibly because the Al^{3+} site ordering in $Li_{2.4}Al_{0.4}Fe_{0.2}S_2$ closely resembles that in Li_5AlS_4. The refined phases for Li_2FeS_2, $Li_{2.2}Al_{0.2}Fe_{0.6}S_2$, and $Li_{2.4}Al_{0.4}Fe_{0.2}S_2$, and the crystal structure of Li_5AlS_4 reported by Lim et al. are shown in Figure S2, projected along the a-axis. As y increases, the anion frameworks appear more distorted, and the anion frameworks of $Li_{2.4}Al_{0.4}Fe_{0.2}S_2$ and Li_5AlS_4 (i.e., $Li_{2.5}Al_{0.5}S_2$) are very similar, indicating that the Al^{3+} site ordering in $Li_{2.4}Al_{0.4}Fe_{0.2}S_2$ closely resembles that in Li_5AlS_4. Hence, the unfit reflections in the same Q range for Li_2FeS_2 and $Li_{2.2}Al_{0.2}Fe_{0.6}S_2$ could be due to ordering of Li^+, Fe^{2+}, and Al^{3+} on the tetrahedral sites that extends beyond the $P2_1/m$ unit cell of Li_5AlS_4 that we use for Rietveld analysis. In fact, the reflections at ≈1.4 and ≈1.6 Q in the pattern of Li_2FeS_2 are partially described by our model, whereas they are not fit at all by the $P\bar{3}m1$ unit cell[14], suggesting that some aspects of the superstructure are captured by the monoclinic unit cell.

There is a history of disagreement about Li_2FeS_2 having a possible superstructure from ordering of cation occupancy on the tetrahedral sites. Some papers report just the primitive $P\bar{3}m1$ unit cell and no superstructure[2, 4, 5], while others report superstructures that vary from two times that of the primitive cell[7, 9], to up to five[9] or even ten times[3] that of the primitive cell. Further complicating the matter, the first report of Li_2FeS_2 in 1976 by Sharma described two closely related polymorphs that form at 885°C and 840°C, which were later observed by others, too.[1, 4, 10] The existence of multiple polymorphs is not uncommon in alkali-Fe-chalcogenide materials. For example, multiple polymorphs of $K_xFe_{2-y}Se_2$ and $K_xFe_2Se_2$ are known and often co-exist; phase pure synthesis of any individual polymorph is difficult.[16] Thus, we propose that the unfit reflections arise from superstructure and/or polymorphs not accounted for by the $P2_1/m$ unit cell model.

target stoichiometry	measured composition			
	Li	Al	Fe	S
Li_2FeS_2	1.970 ± 0.010	-	1.000 ± 0.002	1.914 ± 0.001
	2.023 ± 0.036	-	1.000 ± 0.009	1.928 ± 0.002
$Li_{2.2}Al_{0.2}Fe_{0.6}S_2$	2.112 ± 0.007	0.186 ± 0.021	0.600 ± 0.001	1.883 ± 0.002
	2.297 ± 0.011	0.178 ± 0.022	0.600 ± 0.003	1.853 ± 0.003

Table S2: The composition of four separate reaction batches, two each of Li_2FeS_2 and $Li_{2.2}Al_{0.2}Fe_{0.6}S_2$, measured by ICP-MS for Li, Al, and Fe, and by combustion analysis for S. The data are normalized to the target Fe content.

precursors	other sulfides	reaction with tube	air exposure
Li_2S	FeS_2		
Al_2S_3	Al_2FeS_4		
FeS	Fe_7S_8		
	Fe_3S_4	$C_tLi_uAl_vFe_wSi_xS_yO_z$	$C_tLi_uAl_vFe_wSi_xS_yO_z \cdot n\ H_2O$
	Li_5AlS_4		
	Li_3AlS_3		
	Li_2FeS_2		

Table S3: The possible impurities that we check for the unfit reflections in the sXRD patterns for Li_2FeS_2 and $Li_{2.2}Al_{0.2}Fe_{0.6}S_2$ in Figure 2.2a and b, respectively. We check all polymorphs of each listed impurity, e.g., for FeS_2 we check the pyrite and marcasite polymorphs. The lists of possible impurities for reaction with the quartz tube and air exposure are summarized by chemical formulae that account for all possible combinations. We check all possible polymorphs/combinations that are in the Inorganic Crystal Structure Database under "experimental inorganic structures".

Table S4: The averages and standard deviations of the first cycle charge capacities of the three replicates of Li_2FeS_2, $Li_{2.2}Al_{0.2}Fe_{0.6}S_2$, and $Li_{2.4}Al_{0.4}Fe_{0.2}S_2$ in Figure S3.

	first cycle charge capacities (mole e^- per formula unit)		
	Fe oxidation sloping region	S oxidation plateau	total oxidation
Li_2FeS_2	0.58 ± 0.05	1.09 ± 0.01	1.67 ± 0.06
$Li_{2.2}Al_{0.2}Fe_{0.6}S_2$	0.46 ± 0.02	1.52 ± 0.09	1.98 ± 0.09
$Li_{2.4}Al_{0.4}Fe_{0.2}S_2$	0.14 ± 0.05	1.63 ± 0.21	1.77 ± 0.16

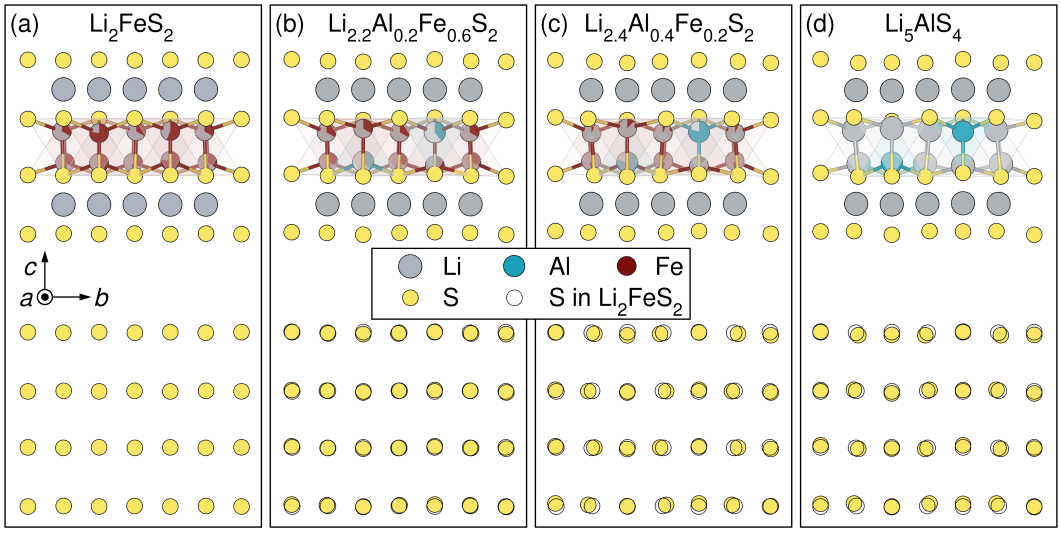

Figure S2: The refined phases (top) and only anion frameworks (bottom) of (a) Li_2FeS_2, (b) $Li_{2.2}Al_{0.2}Fe_{0.6}S_2$, (c) $Li_{2.4}Al_{0.4}Fe_{0.2}S_2$, from our sXRD data, and (d) Li_5AlS_4. The axes in (a) apply to all panels. The anion framework of Li_2FeS_2 has near perfect HCP symmetry. To easily observe changes to the anion framework with y in $Li_{2+y}Al_yFe_{1-2y}S_2$, we superimpose the S atoms in Li_2FeS_2, as transparent black circles, on top of the S atoms in $Li_{2.2}Al_{0.2}Fe_{0.6}S_2$, $Li_{2.4}Al_{0.4}Fe_{0.2}S_2$, and Li_5AlS_4. Qualitatively, the anion frameworks become more distorted from HCP symmetry with larger y. We hypothesize that the high charge density of Al^{3+} causes the distortions.

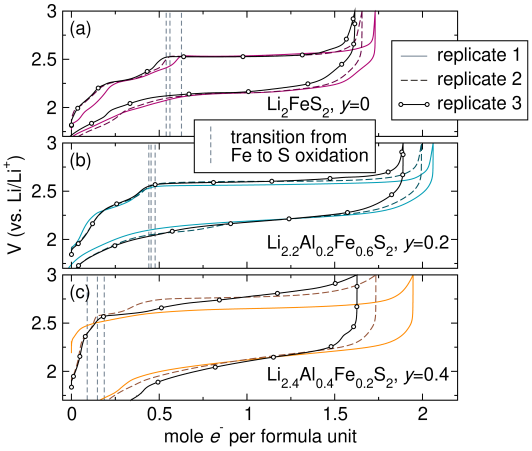

Figure S3: The first cycles of three replicate cells from three separate reaction batches of (a) Li_2FeS_2, (b) $Li_{2.2}Al_{0.2}Fe_{0.6}S_2$, and (c) $Li_{2.4}Al_{0.4}Fe_{0.2}S_2$, all cycled at $C/10$ based on 1 e^- per formula unit. We mark the transition point from the sloping region associated with Fe oxidation to the S oxidation plateau during charge for each replicate with a dashed vertical gray line. The corresponding average capacity and standard deviations associated with the two regions are in Table S4.

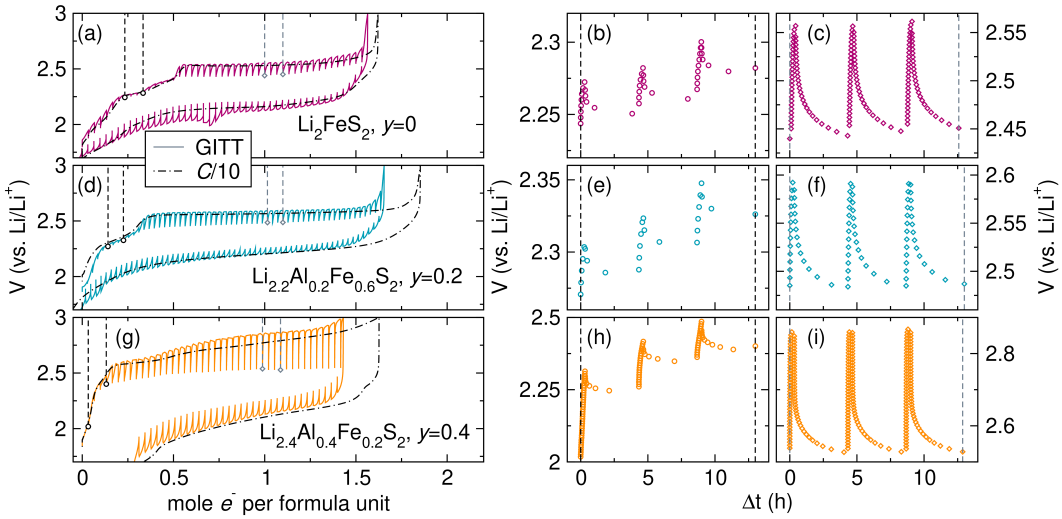

Figure S4: GITT curve and accompanying galvanostatic curve at $C/10$ of the first cycle of (a) Li_2FeS_2, and three representative time-relaxation profiles from the (b) Fe oxidation sloping region and (c) S oxidation plateau. Panels (d), (e), and (f) show the same corresponding data for $Li_{2.2}Al_{0.2}Fe_{0.6}S_2$, and panels (g), (h), and (i) show the same corresponding data for $Li_{2.4}Al_{0.4}Fe_{0.2}S_2$. GITT was obtained at $C/10$ based on 1 mole e^- per f.u. for 20 min separated by 4 h rest periods at open-circuit. The sections of the GITT curves for which the time-relaxation profiles are plotted are marked in panels (a), (d), and (g). Black dashed lines and circular data points mark the section limits of the sloping region, also used in panels (b), (e), and (h). Gray dashed lines and diamond-shaped data points mark the limits for the plateau, again used in panels (c), (f), and (i).

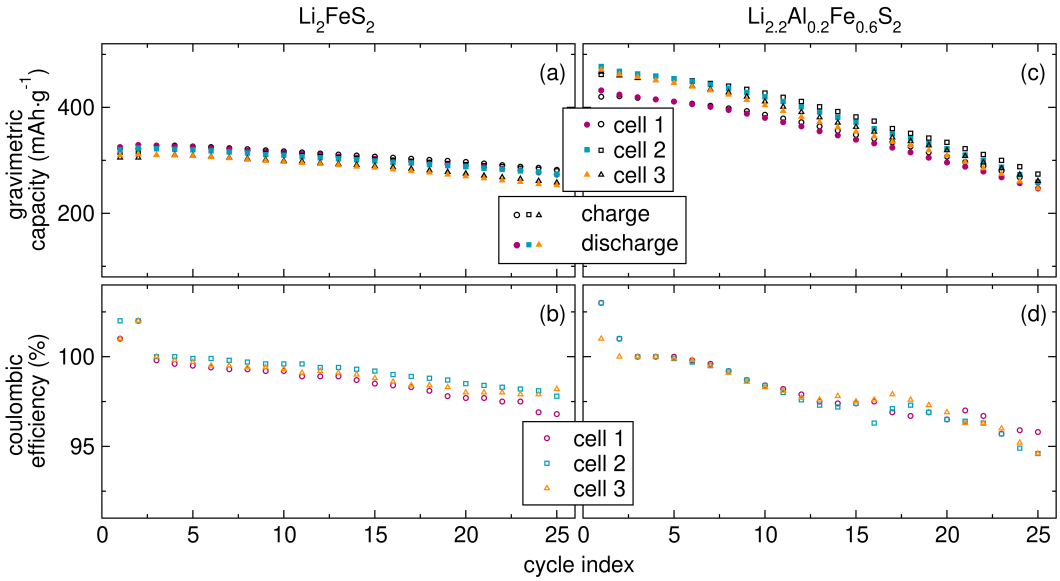

Figure S5: (a) The gravimetric charge and discharge capacities and (b) the coulombic efficiencies of three replicate cells of Li_2FeS_2 cycled at $C/10$ based on 1 mole e^- per f.u. for 25 cycles. Panels (c) and (d) show the same corresponding data for $Li_{2.2}Al_{0.2}Fe_{0.6}S_2$. The average and standard deviation of the three replicates in (a) and (c) are shown in Figure 2.3f in the main text.

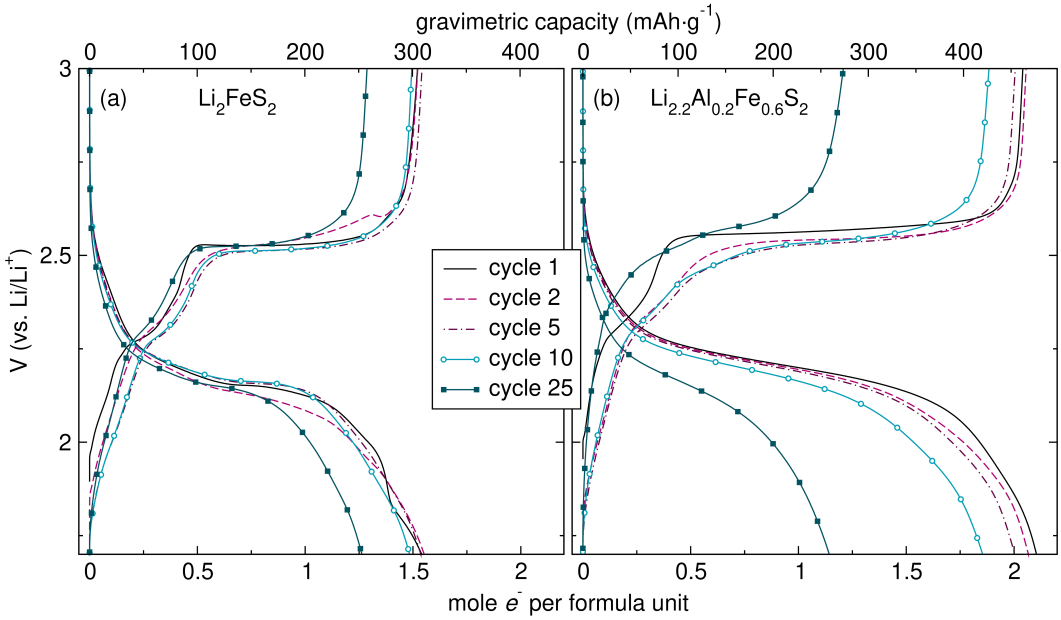

Figure S6: Representative galvanostatic cycles 1, 5, 10, and 25 of (a) Li_2FeS_2 and (b) $Li_{2.2}Al_{0.2}Fe_{0.6}S_2$, both cycled at $C/10$ based on 1 mole e^- per formula unit.

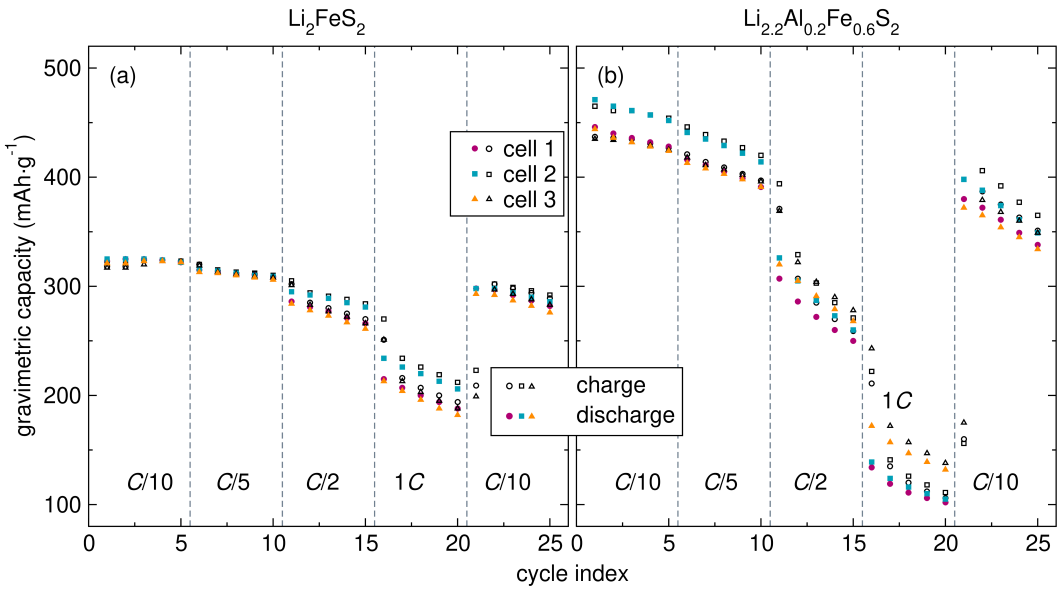

Figure S7: The gravimetric charge and discharge capacities of three replicate cells of (a) Li_2FeS_2 and (b) $Li_{2.2}Al_{0.2}Fe_{0.6}S_2$ subjected to rate capability tests of 5 cycles each at $C/10$, $C/5$, $C/2$, 1C, and again at $C/10$. All C rates are based on 1 e^- per formula unit. The average and standard deviation of these replicates are shown in Figure 2.3g in the main text.

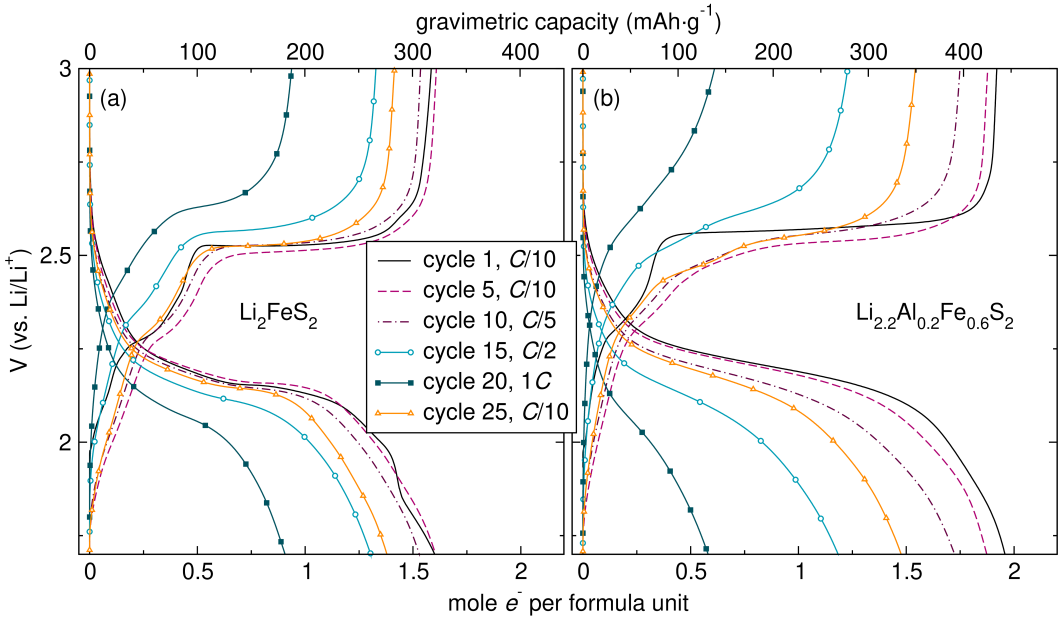

Figure S8: Representative galvanostatic cycles 1 (at $C/10$), 5 (at $C/10$), 10 (at $C/5$), 15 (at $C/2$), 20 (at $1C$), and 25 (again at $C/10$) of (a) Li_2FeS_2 and (b) $Li_{2.2}Al_{0.2}Fe_{0.6}S_2$ from the rate capability tests shown in Figure S7. All C rates are based on 1 mole e^- per formula unit.

Table S5: The averages and standard deviations of the first cycle charge and discharge gravimetric capacities, average voltages, and energy densities of the three replicates of Li_2FeS_2 and $Li_{2.2}Al_{0.2}Fe_{0.6}S_2$ in Figure S3.

	first cycle performance metrics					
	charge			discharge		
	gravimetric capacity ($mAh \cdot g^{-1}$)	average voltage (V)	energy density ($Wh \cdot kg^{-1}$)	gravimetric capacity ($mAh \cdot g^{-1}$)	average voltage (V)	energy density ($Wh \cdot kg^{-1}$)
Li_2FeS_2	334±12	2.452±0.004	819±28	331±12	2.295±0.004	760±26
$Li_{2.2}Al_{0.2}Fe_{0.6}S_2$	449±20	2.505±0.007	1125±49	446±24	2.294±0.004	1024±55

Supplementary Note S3: Additional Fe K-edge XAS data and its limitations

We measure Fe K-edge XAS of both materials at various SOCs and after annealing at the transition point to examine changes in the Fe-S $3d$-$3p$ states. The spectra of both materials, shown in Figure S9a and b, exhibit a decrease in the intensity of the pre-edge feature x after annealing, to a level similar to the mid-slope spectra. For Li_2FeS_2, the decrease can be partially attributed to the formation of FeS_2, where the centrosymmetric octahedral Fe coordination produces a less intense pre-edge than the original non-centrosymmetric tetrahedral Fe coordination.[17] However, for $Li_{2.2}Al_{0.2}Fe_{0.6}S_2$, the annealed material remains a single phase with only tetrahedrally coordinated Fe (Figure S14b). Hence, the decrease in pre-edge intensity for $Li_{2.2}Al_{0.2}Fe_{0.6}S_2$ suggests greater occupancy of Fe-S $3d$-$3p$ states in the annealed material, i.e., formal Fe reduction. The first derivatives of the spectra for both materials, shown in Figure S9c and d, indicate that the rising edge positions of the annealed and mid-slope states are identical, confirming formal Fe reduction by annealing the cathode at the transition point in both materials. The discrepancy between the annealed and mid-slope states of Li_2FeS_2 is clear, as the first derivative of the annealed state differs in shape from that of the mid-slope. Remarkably, both the original spectra (Figure S9b) and first derivatives (Figure S9d) of $Li_{2.2}Al_{0.2}Fe_{0.6}S_2$ in the annealed and mid-slope states almost completely overlap, indicating that Fe is very similar in both states.

We summarize the data in Figure S9e,f by overlaying the rising edge positions with the galvanostatic data. Notably, the position of the Fe K-edge of both materials remains similar across the transition, mid-plateau, and charged states. However, the energy resolution at the rising edge ($\approx$1 eV for $3d$ metals) is limited by the short lifetime of the 1s core hole.[17] Kowalska et al. encountered this limitation in Fe-S clusters, where the rising edges of mixed-valent (Fe^{2+}/Fe^{3+}) and formally reduced diferrous (only Fe^{2+}) clusters were "effectively superimposable." Accordingly, they note: "This observation highlights the fact that caution must be exercised in using the rising edges as an isolated measure of oxidation state."[18] Thus, to better evaluate the Fe electronic structure, we use a more sensitive probe of the occupancy of Fe-S $3d$-$3p$ states (Mössbauer spectroscopy).

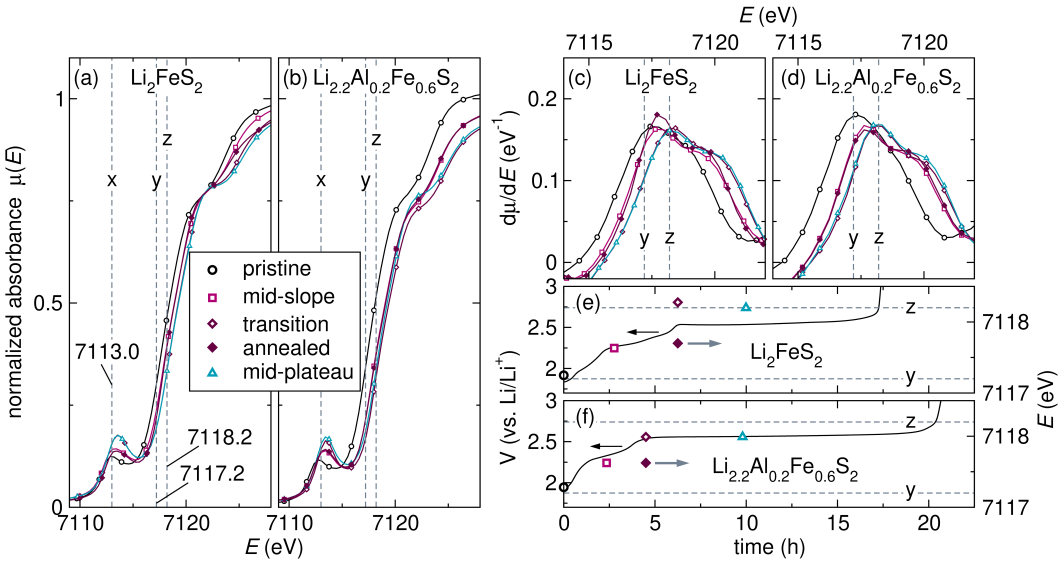

Figure S9: *Ex-situ* Fe K-edge XAS spectra of (a) Li_2FeS_2 and (b) $Li_{2.2}Al_{0.2}Fe_{0.6}S_2$ at the pristine, mid-slope, transition, annealed, and mid-plateau SOCs. The first derivative of the rising edge regions for (c) Li_2FeS_2 and (d) $Li_{2.2}Al_{0.2}Fe_{0.6}S_2$. The energies of the maxima of the first derivatives at each of the SOCs are overlaid with the corresponding galvanostatic cycling data for (e) Li_2FeS_2 and (f) $Li_{2.2}Al_{0.2}Fe_{0.6}S_2$. The dashed lines in all panels labeled x, y, and z indicate the same features as in Figure 2.4: the pre-edge x, at 7113.0 eV, and the two rising edges observed at different SOCs, y and z, at 7117.2 eV and 7118.2 eV, respectively.

Supplementary Note S4: Long-range structural changes in Li_2FeS_2 and $Li_{2.2}Al_{0.2}Fe_{0.6}S_2$

In our previous work on Li_2FeS_2, we found that the long-range order is maintained during the initial sloping region associated with Fe oxidation, and that there is a gradual loss of long-range order during the S oxidation plateau.[14] Here, in Figure S10, we report *ex-situ* XRD of Li_2FeS_2 and $Li_{2.2}Al_{0.2}Fe_{0.6}S_2$ in the pristine, transition, charged, and discharged SOCs, focused on the 2θ range for the (0 0 1) reflection as an indicator of overall structural changes. We also show the full patterns in Figure S11 for completeness, but primarily discuss the (0 0 1) reflection. The Li_2FeS_2 data supports our previous findings. Relative to the pristine state, the (0 0 1) reflection of the transition SOC shifts to higher 2θ by $\approx 0.1°$, and becomes more intense, indicating that the material is contracted along the c-axis, and more crystalline, respectively. In the charged state, the (0 0 1) reflection loses most of its intensity, indicating the loss of long-range order. In the discharged state, the (0 0 1) reflection recovers the full intensity of the pristine state, shifted to slightly lower 2θ by $\approx 0.05°$ relative to the pristine state.

The $Li_{2.2}Al_{0.2}Fe_{0.6}S_2$ data is similar to Li_2FeS_2. However, the transition SOC of Li_2FeS_2, in addition to the contraction, exhibits a new shoulder at slightly higher ($\approx 0.3°$) 2θ, which is absent in $Li_{2.2}Al_{0.2}Fe_{0.6}S_2$. This slight discrepancy suggests that the long-range structural response to the Fe oxidation in Li_2FeS_2 is less single-phase in nature compared to that in $Li_{2.2}Al_{0.2}Fe_{0.6}S_2$. Importantly, both materials recover the full intensity of the (0 0 1) reflection in the discharged state. This indicates that the original long-range structure of the pristine state is restored during discharge, despite greater degrees of structurally burdensome anion redox in $Li_{2.2}Al_{0.2}Fe_{0.6}S_2$ compared to Li_2FeS_2, highlighting the reversibility of the multi-electron redox mechanism. The recovery of long-range order is also evident in the full XRD patterns (Figure S11).

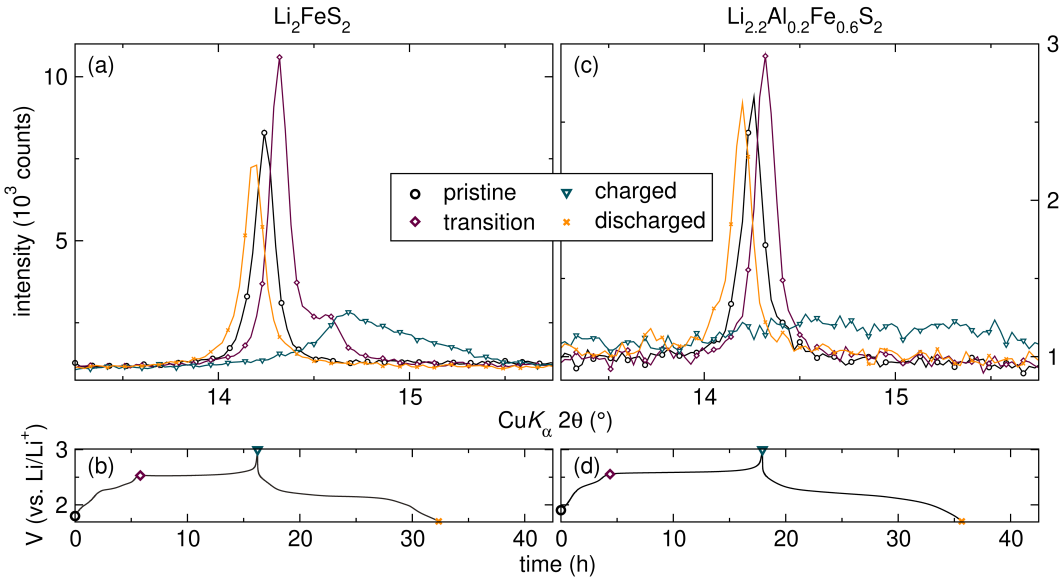

Figure S10: *Ex-situ* XRD, focused on the (0 0 1) reflection between ≈13° to 16° 2θ, of (a) Li_2FeS_2 in the pristine, transition, charged, and discharged states with (b) accompanying galvanostatic data. The same corresponding data for $Li_{2.2}Al_{0.2}Fe_{0.6}S_2$ is shown in panels (c) and (d), respectively.

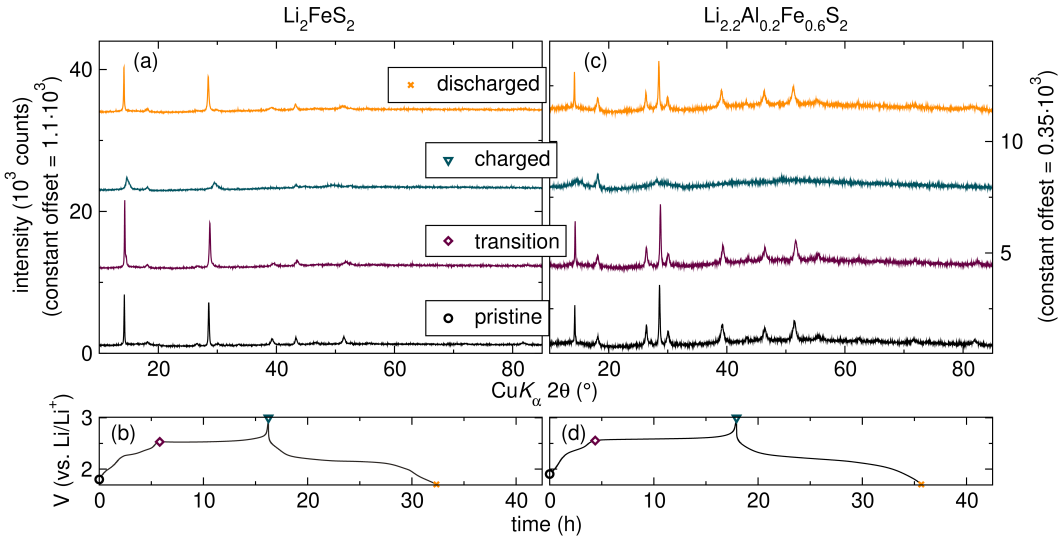

Figure S11: Full *ex-situ* XRD patterns between 10 to 85 2θ (°) of (a) Li_2FeS_2 in the pristine, transition, charged, and discharged states with (b) accompanying galvanostatic data. The same corresponding data for $Li_{2.2}Al_{0.2}Fe_{0.6}S_2$ is shown in panels (c) and (d), respectively. Figure S10 suggests that long-range order is restored in the discharged state by showing the recovery of the layer spacing associated with the (0 0 1) reflection. The near-identical full XRD patterns in the pristine and discharged states shown here confirm that this structural restoration extends to the entire long-range order, not just the layer spacing.

Supplementary Note S5: Cation inventory and capacity limits of Li_2FeS_2 and $Li_{2.2}Al_{0.2}Fe_{0.6}S_2$

In Li_2FeS_2, the anion redox capacity is limited to only ≈55±1% of the S content before the voltage polarizes and additional capacity is inaccessible. At the end of charge, not only does some of the S remain as S^{2-} but ≈0.33±0.06 mole Li^+ per f.u. remain in the material. In $Li_{2.2}Al_{0.2}Fe_{0.6}S_2$, ≈76±5% of the S is oxidized and ≈0.22±0.11 mole Li^+ per f.u. remains. One could attribute the differences in capacity to the Li^+ inventory, arguing that the anion framework collapses/converts below a critical Li^+ content, noticing that the remnant Li^+ contents in the fully charged Li_2FeS_2 and $Li_{2.2}Al_{0.2}Fe_{0.6}S_2$ are within ≈0.1 Li^+ per f.u. of each other. However, we note in Section 2.2 that $Li_{2.4}Al_{0.4}Fe_{0.2}S_2$, despite having even greater Li^+ content than $Li_{2.2}Al_{0.2}Fe_{0.6}S_2$, has lower capacity (Figure 2.3c). We also show in Figure S10 that the long-range order, or overall anion framework, is anyway not preserved beyond the transition SOC in both Li_2FeS_2 and $Li_{2.2}Al_{0.2}Fe_{0.6}S_2$, which is also supported by *operando* XRD measurements in our previous work on Li_2FeS_2.[14]

Further, an argument that cites residual Li^+ in the charged state should look at the total cation content, rather than just Li^+, as arguably the higher charge density $Fe^{2+/3+}$ and Al^{3+} cations would play a bigger role than Li^+ in supporting the anion framework against collapse/conversion. In considering total remnant cation content in fully charged Li_2FeS_2 and $Li_{2.2}Al_{0.2}Fe_{0.6}S_2$, we find Li_2FeS_2 has ≈1.33±0.06 cations per f.u. left, whereas $Li_{2.2}Al_{0.2}Fe_{0.6}S_2$ has only ≈1.02±0.11 cations per f.u. Thus, if the total remaining cation content at full charge was responsible for oxidation capacity limits, we would expect $Li_{2.2}Al_{0.2}Fe_{0.6}S_2$ to have lower capacity (in mole e^- per f.u.) because it would require additional Li^+ in the charged state to compensate for having lower non-Li^+ cation content. Thus, another mechanism is responsible for limiting the capacity of Li_2FeS_2 relative to $Li_{2.2}Al_{0.2}Fe_{0.6}S_2$, as limits cannot be accounted for by Li^+ inventory or total cation content in the charged state in both materials.

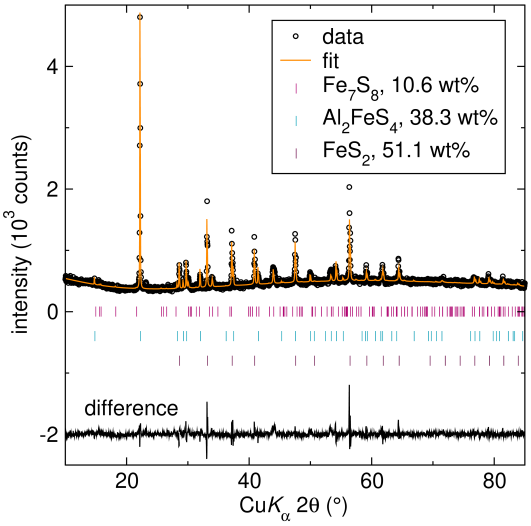

Figure S12: XRD of the attempted synthesis of $Al_{0.2}Fe_{0.6}S_2$. The Rietveld refinement (fit), reflection locations of each phase in the fit, the weight percent contribution of each phase, and the difference between the fit and data are all shown. All observed reflections are accounted for by a three phase fit to Fe_7S_8 (10.6 wt%), Al_2FeS_4 (38.3 wt%), and FeS_2 (51.1 wt%).

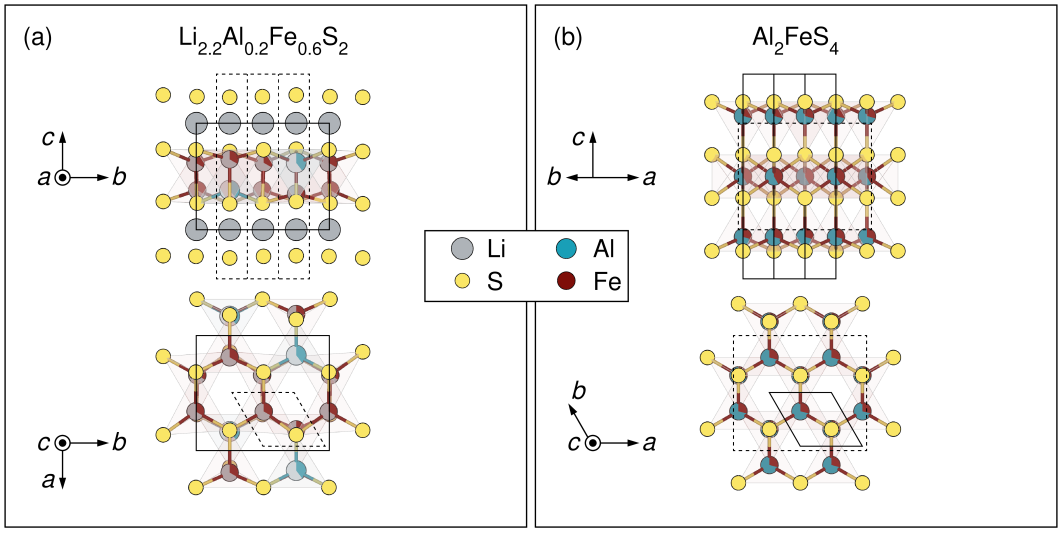

Figure S13: The crystal structure of (a) $Li_{2.2}Al_{0.2}Fe_{0.6}S_2$ from Rietveld refinement of the sXRD data in Figure 2.2 projected along the *a*-axis (top) and *c*-axis (bottom), and the crystal structure of (b) Al_2FeS_4 projected along the *a*-*c* plane (top) and *c*-axis (bottom). To show how the structures are related, the unit cell of the material being shown is indicated with a solid, black line, and the unit cell of the other material is indicated with a dashed, black line. The Li^+-only layers perpendicular to the *c*-axis in $Li_{2.2}Al_{0.2}Fe_{0.6}S_2$ contain octahedrally coordinated Li^+, while the corresponding layers in Al_2FeS_4 have only tetrahedrally coordinated Fe^{2+} or Al^{3+}. To easily compare tetrahedral sites, we omit all octahedrally coordinated cations in the bottom projections along the *c*-axis for both materials. This further highlights the possible structural similarity between delithiated $Li_{2.2}Al_{0.2}Fe_{0.6}S_2$ and Al_2FeS_4.

Table S6: Detected S content in wt% before and after annealing by combustion analysis. We also show the S loss in wt% and convert this to mole S per f.u. based on approximate molar masses of 129.7 g·mole^{-1} of $Li_{2-x}FeS_2$ ($x \approx 0.6$) and 115.5 g·mole^{-1} of $Li_{2.2-x}Al_{0.2}Fe_{0.6}S_2$ ($x \approx 0.4$). The results show that S loss cannot explain the changes we observe after annealing –$Li_{2.2}Al_{0.2}Fe_{0.6}S_2$ shows no S loss and Li_2FeS_2 shows very minimal S loss.

	S content (wt%)		S loss	
	before annealing	after annealing	(wt%)	mole S per f.u.
Li_2FeS_2	26.9±0.1	26.2±0.1	0.7	0.04
$Li_{2.2}Al_{0.2}Fe_{0.6}S_2$	29.7±0.1	29.7±0.1	0.0	0.00

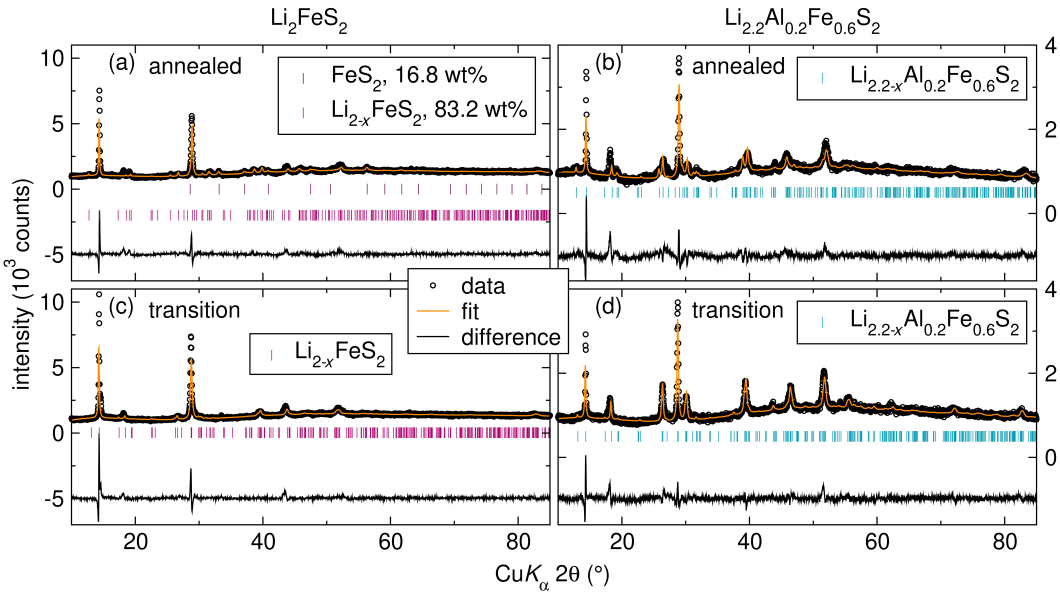

Figure S14: *Ex-situ* XRD of the annealed states of (a) Li_2FeS_2 and (b) $Li_{2.2}Al_{0.2}Fe_{0.6}S_2$, and the transition states of (c) Li_2FeS_2 and (d) $Li_{2.2}Al_{0.2}Fe_{0.6}S_2$. Each panel shows the Rietveld refinement (fit), reflection locations of each phase in the fit, and the difference between the fit and data. All patterns are described by a single phase, except Li_2FeS_2 in the annealed state, which is fit to two phases: pyrite FeS_2 (16.8 wt%), and $Li_{2-x}FeS_2$ (83.2 wt%). While we label the phases in the fits as Li_{2-x} in (a) and (c) or $Li_{2.2-x}$ in (b) and (d) to indicate delithiated samples, the crystallographic information files used for the refinements are those of pristine (fully lithiated) Li_2FeS_2 and $Li_{2.2}Al_{0.2}Fe_{0.6}S_2$.

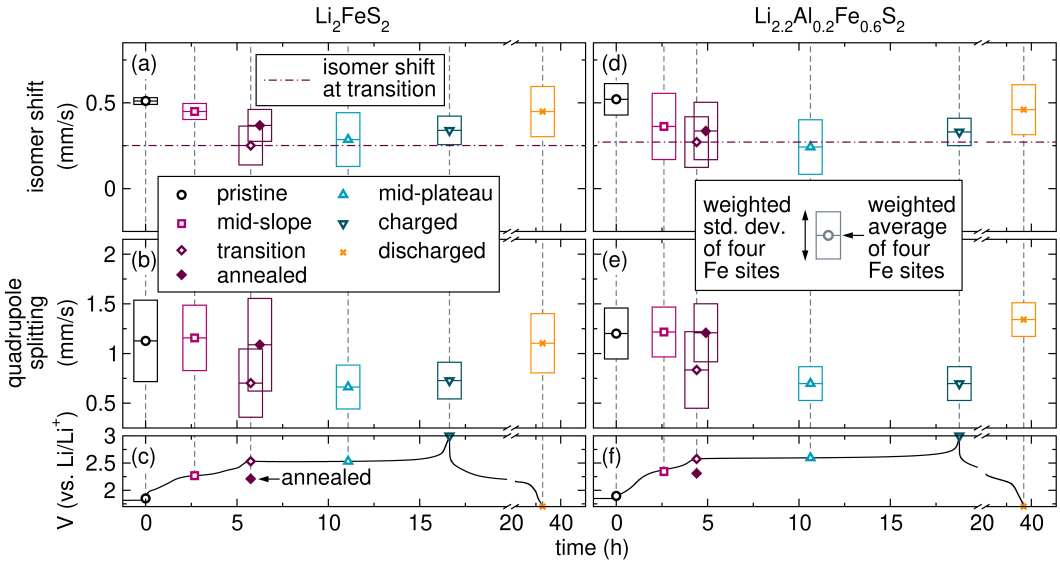

Figure S15: The weighted averages and corresponding weighted standard deviations of the isomer shifts (a) and quadrupole splittings (b) of the Lorentzian doublets used to fit *ex-situ* Mössbauer spectra of Li_2FeS_2, with the corresponding galvanostatic data (c) showing the SOCs at which the spectra are measured. Panels (d), (e), and (f), respectively, indicate the same corresponding data for $Li_{2.2}Al_{0.2}Fe_{0.6}S_2$. In panels (a), (b), (d), and (e), the weighted average is indicated by the symbol, and the weighted standard deviation is indicated by height of the box accompanying the symbol. The dotted/dashed dark purple horizontal line in panels (a) and (d) indicates the weighted average isomer shift at the transition SOC. The isomer shift data is discussed in the main text. The quadrupole splitting is similar in both materials. After annealing, the quadrupole splitting broadens for Li_2FeS_2 but narrows for $Li_{2.2}Al_{0.2}Fe_{0.6}S_2$, supporting that the former undergoes conversion while the latter does not.

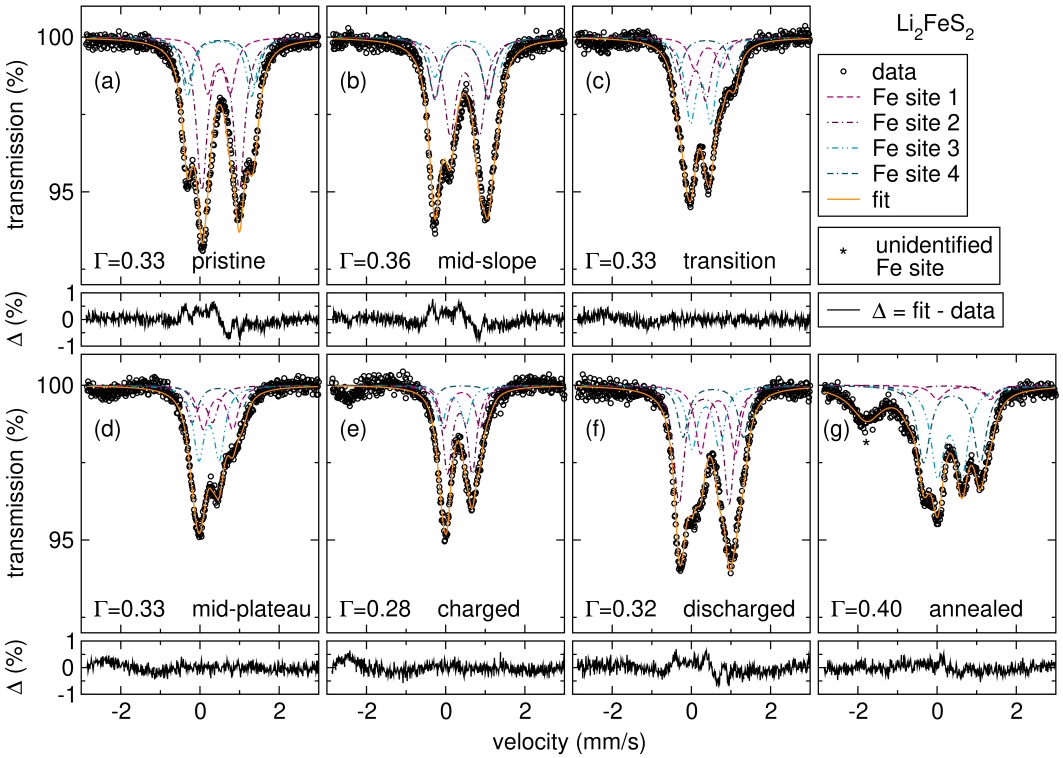

Figure S16: Mössbauer spectrum, four Fe sites in each fit, fit (sum of the Fe sites), and fit-data difference (Δ) of the (a) pristine, (b) mid-slope, (c) transition, (d) mid-plateau, (e) charged, (f) discharged, and (g) annealed states of Li_2FeS_2. The linewidth (Γ) of the four Fe sites is constrained to be equal in each fit and is shown in each panel. A single unidentified Fe site (peak) in annealed sample is indicated by an asterisk.

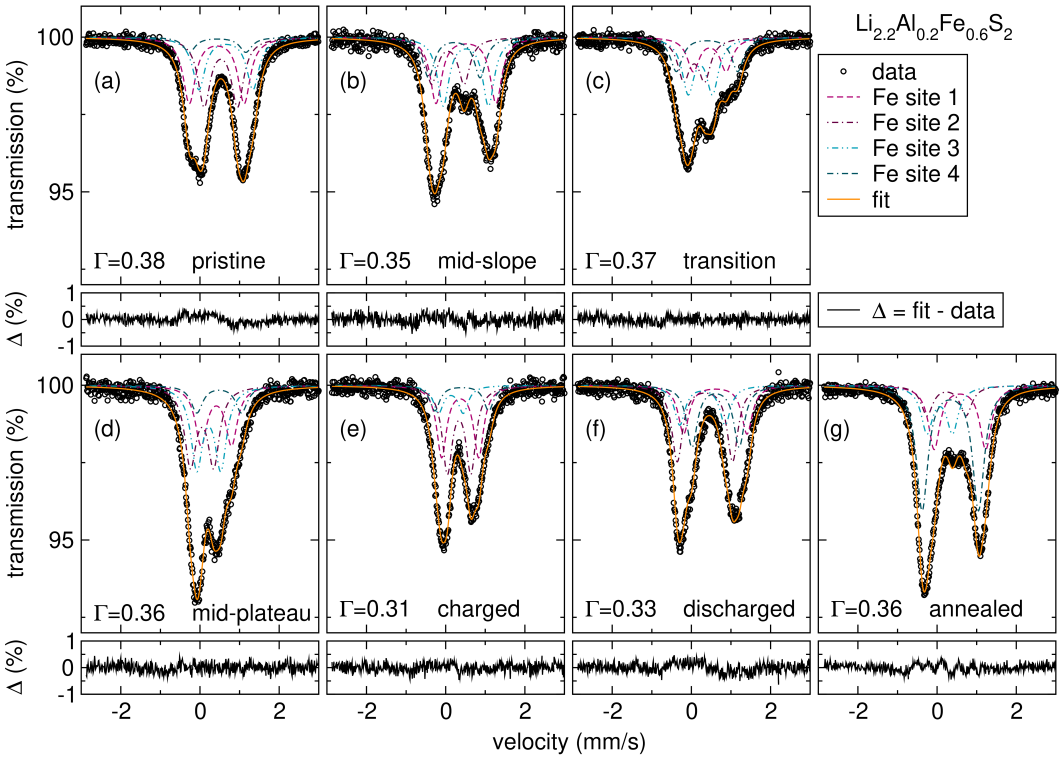

Figure S17: Mössbauer spectrum, four Fe sites in each fit, fit (sum of the Fe sites), and fit-data difference (Δ) of the (a) pristine, (b) mid-slope, (c) transition, (d) mid-plateau, (e) charged, (f) discharged, and (g) annealed states of $Li_{2.2}Al_{0.2}Fe_{0.6}S_2$. The linewidth (Γ) of the four Fe sites is constrained to be equal in each fit and is shown in each panel.

Table S7: All Mössbauer fit parameters of each spectrum in Figures S16 and S17.

Li_2FeS_2				
state	linewidth Γ (mm·s^{-1})	isomer shift (mm·s^{-1})	quadrupole splitting (mm·s^{-1})	area (%)
pristine	0.33	0.48	0.57	17.2
		0.52	0.95	48.3
		0.49	1.62	19.1
		0.53	1.70	15.4
mid-slope	0.36	0.40	1.35	23.4
		0.48	0.74	36.9
		0.51	1.57	15.6
		0.40	1.35	24.1
transition	0.33	0.42	0.70	14.7
		0.11	0.52	28.7
		0.24	0.51	39.0
		0.37	1.43	17.6
mid-plateau	0.33	0.46	0.74	25.2
		0.06	0.52	20.4
		0.23	0.52	41.2
		0.48	1.17	13.3
charged	0.28	0.42	0.90	24.1
		0.36	0.62	48.4
		0.19	0.62	22.5
		0.44	1.33	5.1
discharged	0.32	0.67	0.88	22.5
		0.32	1.26	39.4
		0.36	0.69	20.7
		0.55	1.52	17.4
annealed	0.40	0.68	1.33	7.5
		0.30	2.08	6.2
		0.32	0.61	45.7

continued on next page

continued from previous page

state	linewidth Γ (mm·s^{-1})	isomer shift (mm·s^{-1})	quadrupole splitting (mm·s^{-1})	area (%)
		0.38	1.43	40.6

$Li_{2.2}Al_{0.2}Fe_{0.6}S_2$

state	linewidth Γ (mm·s^{-1})	isomer shift (mm·s^{-1})	quadrupole splitting (mm·s^{-1})	area (%)
pristine	0.38	0.42	1.39	32.9
		0.53	0.84	33.7
		0.66	1.36	25.9
		0.44	1.43	7.5
mid-slope	0.35	0.51	1.52	30.0
		0.05	0.82	20.8
		0.51	1.14	30.9
		0.22	1.30	18.3
transition	0.37	0.46	0.83	20.5
		0.07	0.53	25.3
		0.23	0.61	33.1
		0.40	1.55	21.1
mid-plateau	0.36	0.41	0.77	23.9
		0.05	0.59	31.9
		0.22	0.61	33.0
		0.48	1.13	11.2
charged	0.31	0.37	0.94	34.2
		0.34	0.59	40.7
		0.13	0.63	12.9
		0.41	1.36	12.3
discharged	0.33	0.60	1.60	21.6
		0.34	1.40	33.7
		0.28	1.15	17.5
		0.61	1.19	27.3

continued on next page

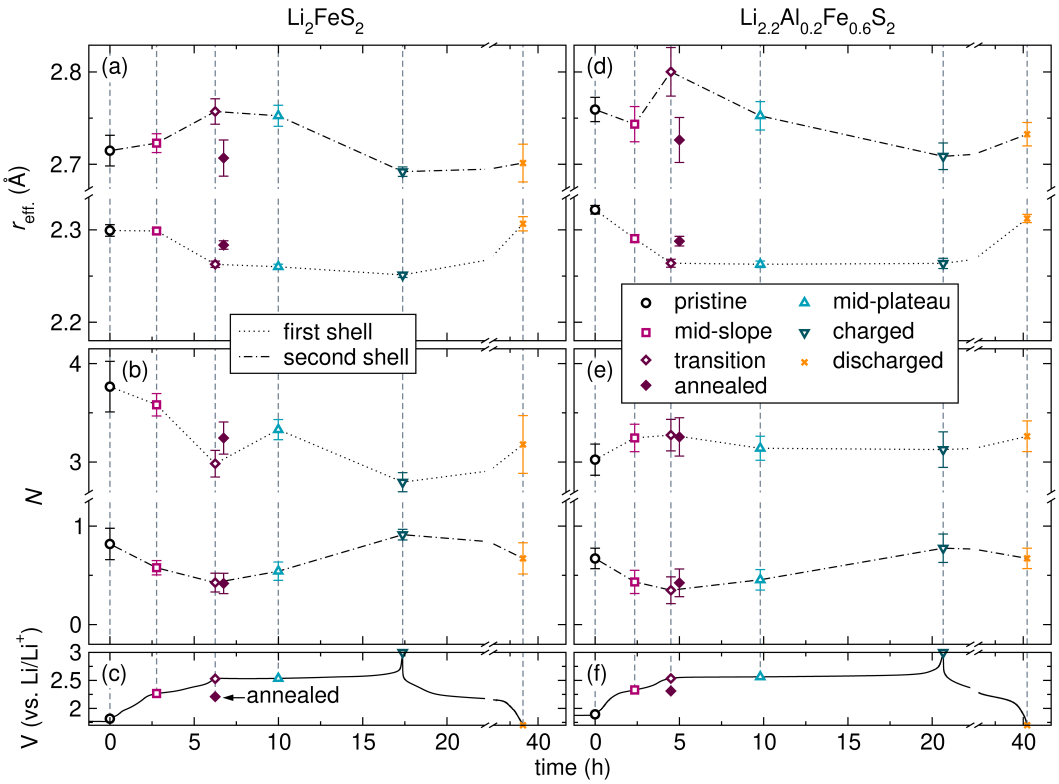

Figure S18: The first and second shell values of (a) $r_{\text{eff.}}$ and (b) N for Li_2FeS_2, with accompanying galvanostatic data (c) indicating the SOCs at which the EXAFS analysis is conducted. Panels (d), (e), and (f), respectively, indicate the same corresponding data for $Li_{2.2}Al_{0.2}Fe_{0.6}S_2$. All $r_{\text{eff.}}$ and N values are shown with statistical error bars. The first shell data is discussed in the main text. The second shell data shows similar trends for Li_2FeS_2 and $Li_{2.2}Al_{0.2}Fe_{0.6}S_2$.

continued from previous page

state	linewidth Γ (mm·s^{-1})	isomer shift (mm·s^{-1})	quadrupole splitting (mm·s^{-1})	area (%)
annealed	0.36	0.58	1.30	24.1
		0.24	0.99	11.3
		0.07	0.65	17.4
		0.33	1.42	47.2

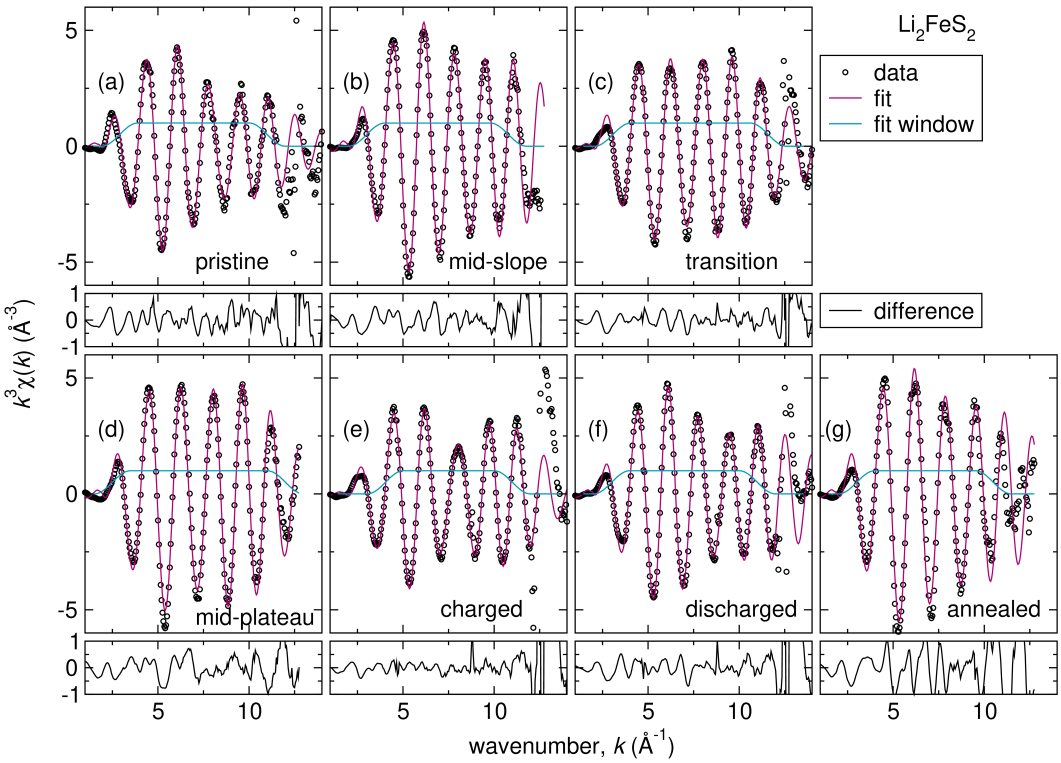

Figure S19: Fe K-edge EXAFS $k^3\chi(k)$ data, fit, fit window, and fit-data difference of the (a) pristine, (b) mid-slope, (c) transition, (d) mid-plateau, (e) charged, (f) discharged, and (g) annealed states of Li_2FeS_2.

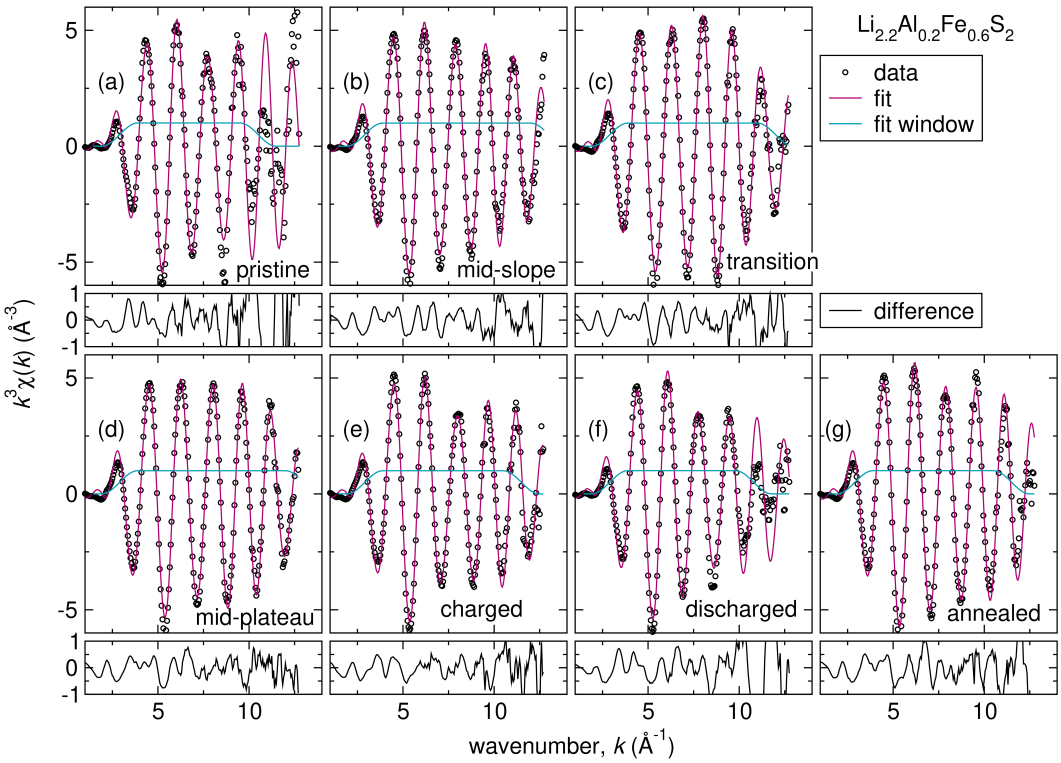

Figure S20: Fe K-edge EXAFS $k^3\chi(k)$ data, fit, fit window, and fit-data difference of the (a) pristine, (b) mid-slope, (c) transition, (d) mid-plateau, (e) charged, (f) discharged, and (g) annealed states of $Li_{2.2}Al_{0.2}Fe_{0.6}S_2$.

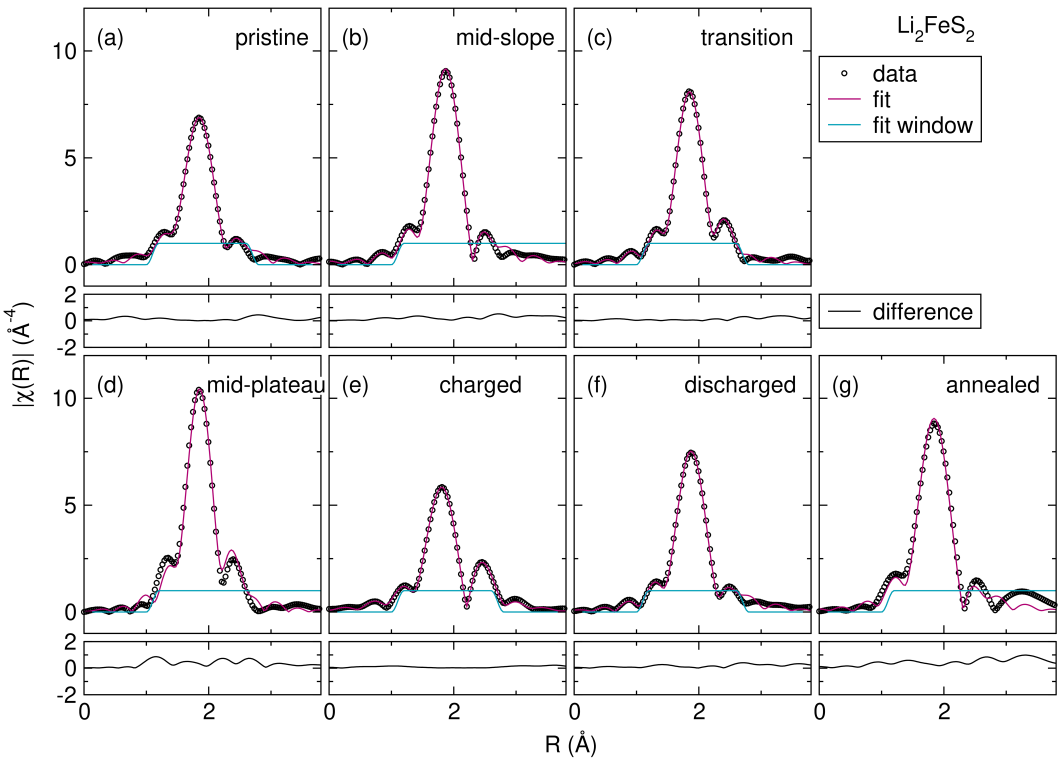

Figure S21: Fe K-edge EXAFS k^3-weighted $|\chi(R)|$ data, fit, fit window, and fit-data difference of the (a) pristine, (b) mid-slope, (c) transition, (d) mid-plateau, (e) charged, (f) discharged, and (g) annealed states of Li_2FeS_2.

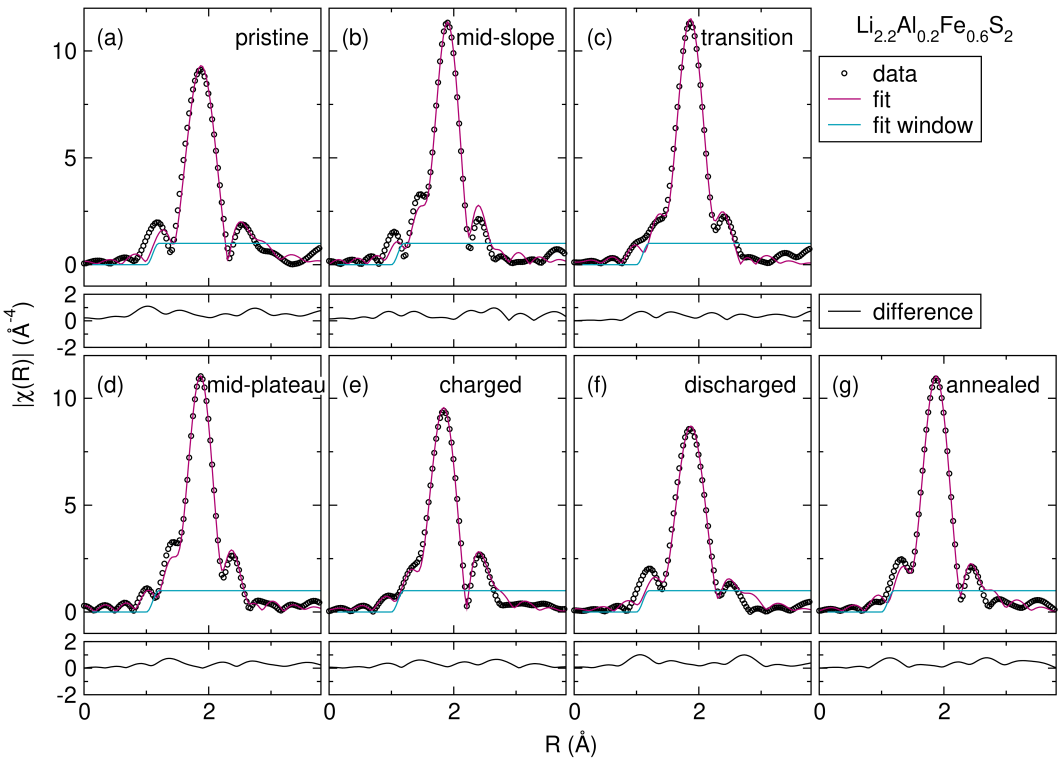

Figure S22: Fe K-edge EXAFS k^3-weighted $|\chi(R)|$ data, fit, fit window, and fit-data difference of the (a) pristine, (b) mid-slope, (c) transition, (d) mid-plateau, (e) charged, (f) discharged, and (g) annealed states of $Li_{2.2}Al_{0.2}Fe_{0.6}S_2$.

Table S8: EXAFS fitting parameters for Li_2FeS_2 and $Li_{2.2}Al_{0.2}Fe_{0.6}S_2$.

Li_2FeS_2

state	S_0^2 intrinsic losses	ΔE_0 energy correction	σ^2 local disorder	$r_{\text{eff, first shell}}$ (Å) Fe-S bond length	$N_{\text{first shell}}$ Fe coord. number	$r_{\text{eff, second shell}}$ (Å) nearest Fe-Fe distance	$N_{\text{second shell}}$ edge-sharing tetrahedra occupancy
pristine	0.618	1.1±0.7	0.006±0.001	2.30±0.01	3.8±0.3	2.72±0.02	0.82±0.2
mid-slope	0.679	4.2±0.3	0.004± ≤0.001	2.30±0.01	3.6±0.1	2.72±0.01	0.58±0.07
transition	0.618	2.2±0.5	0.003± ≤0.001	2.26±0.01	3.0±0.1	2.76±0.01	0.43±0.10
mid-plateau	0.679	3.2±0.3	0.003± ≤0.001	2.26±0.01	3.3±0.1	2.75±0.01	0.54±0.09
charged	0.618	0.7±0.4	0.004± ≤0.001	2.25±0.01	2.8±0.1	2.69±0.01	0.91±0.05
discharged	0.618	3.5±1.0	0.004±0.001	2.31±0.01	3.2±0.3	2.70±0.02	0.67±0.2
annealed	0.788	2.6±0.5	0.004±0.001	2.28±0.01	3.2±0.2	2.71±0.02	0.42±0.1

$Li_{2.2}Al_{0.2}Fe_{0.6}S_2$

state	S_0^2	ΔE_0	σ^2	$r_{\text{eff, first shell}}$ (Å)	$N_{\text{first shell}}$	$r_{\text{eff, second shell}}$ (Å)	$N_{\text{second shell}}$
pristine	0.788	3.5±0.5	0.003±0.001	2.32±0.01	3.0±0.2	2.76±0.01	0.67±0.1
mid-slope	0.788	3.9±0.4	0.004±0.001	2.29±0.01	3.2±0.1	2.74±0.02	0.43±0.12
transition	0.788	3.5±0.5	0.003±0.001	2.26±0.01	3.3±0.2	2.80±0.03	0.35±0.14
mid-plateau	0.788	2.9±0.4	0.004± ≤0.001	2.26±0.01	3.1±0.1	2.75±0.02	0.46±0.10
charged	0.788	2.4±0.6	0.004±0.001	2.26±0.01	3.1±0.2	2.71±0.01	0.78±0.14

continued on next page

continued from previous page

state	S_0^2	ΔE_0	σ^2	$r_{\text{eff, first shell}}$ (Å)	$N_{\text{first shell}}$	$r_{\text{eff, second shell}}$ (Å)	$N_{\text{second shell}}$
discharged	0.788	3.1±0.5	0.005±0.001	2.31±0.01	3.3±0.2	2.73±0.01	0.67±0.10
annealed	0.788	3.8±0.6	0.003±0.001	2.29±0.01	3.3±0.2	2.73±0.02	0.42±0.14

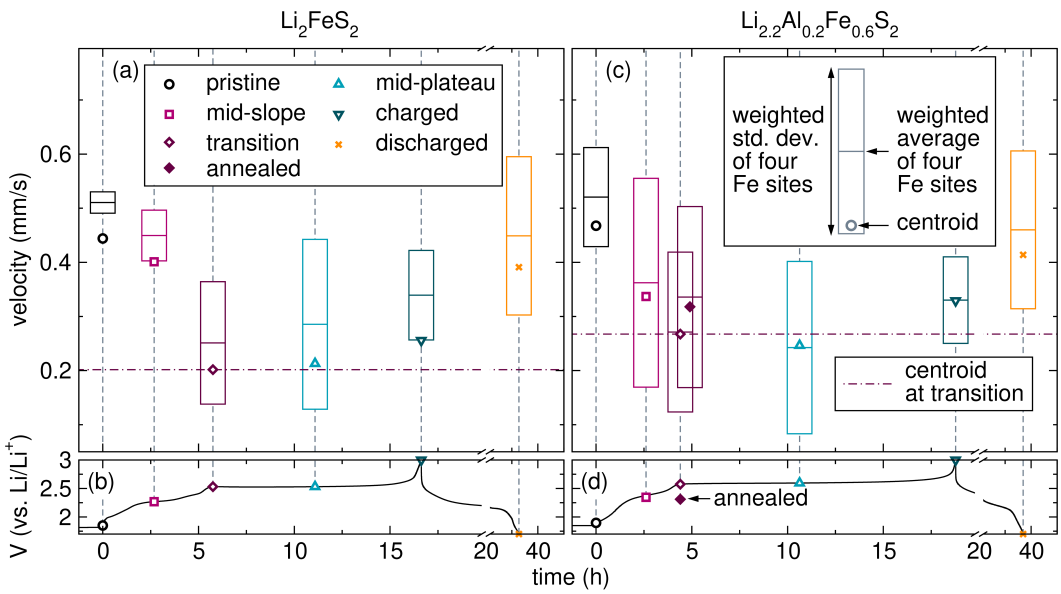

Figure S23: The centroids of the Mössbauer spectra, the weighted averages and weighted standard deviations of the isomer shifts of Li_2FeS_2 (a), with accompanying galvanostatic data (b). Panels (c) and (d) respectively show the same corresponding data for $Li_{2.2}Al_{0.2}Fe_{0.6}S_2$. We calculate the centroids of the spectra in Figures S16 and S17 as centroid = $\frac{\sum_i I(v_i)\cdot v_i}{\sum_i I(v_i)}$ where $I(v_i)$ is the normalized absorption intensity, v_i is the velocity, and i indexes the data points. The dotted/dashed dark purple horizontal line in panels (a) and (c) indicates the centroid at the transition SOC. The centroids, calculated directly from the data without parameters, provide direct access to the isomer shift. They follow the same trend as the weighted average isomer shifts from our fits, confirming that the fits accurately represent the data and are unbiased. The annealed state of Li_2FeS_2 is omitted because it contains multiple phases, preventing meaningful spectral centroid analysis.

Supplementary Note S6: Relative covalency of $(S_2)^{2-}$ and S^{2-} with Fe

The isomer shift increases during the S oxidation plateau in both Li_2FeS_2 and $Li_{2.2}Al_{0.2}Fe_{0.6}S_2$. One could suggest that the increase in the isomer shift is not actually reflective of Fe reduction, but rather caused by the difference in the covalency of $(S_2)^{2-}$ 'ligands' that form during the S oxidation plateau, relative to the covalency of the unoxidized S^{2-} ligands. For this to be true, $(S_2)^{2-}$ would need to be a less covalent ligand than S^{2-}. While $(S_2)^{2-}$ is seemingly less covalent, as one might expect S^{2-} to be a better π donor, structural and Mössbauer data on Fe-S binaries and Fe complexes with thiolate/persulfide ligands show the opposite –that, in fact, $(S_2)^{2-}$ is a more covalent ligand to Fe than than S^{2-}. The Fe-S bond lengths in FeS_2 and FeS, both materials with octahedrally coordinated formal Fe^{2+}, can suggest the relative covalency of $(S_2)^{2-}$ and S^{2-}, because all the ligands in FeS_2 are $(S_2)^{2-}$, and in FeS all the ligands are S^{2-}. The Fe-S bond length in FeS_2 is 2.2645 Å,[19] whereas in FeS it is either 2.519 Å or 2.427 Å.[20] Thus, the shorter bonds in FeS_2 suggest that it is the more covalent material. The reported isomer shifts of FeS_2, which are close to 0.25[21] to 0.325[22] mm/s, and FeS, which is 0.72 mm/s,[23] again indicate far greater covalency in FeS_2. Rickard et al. measured Mössbauer of six-coordinate Fe^{3+} complexes[24, 25] for which they exchange thiolate ligands for persulfide ligands, varying the number of persulfide ligands between 0 and 2.[26] They find that the isomer shift decreases markedly with each persulfide added, from 0.37 mm/s with 0 persulfides, to 0.29 mm/s with 2 persulfides. They attribute the decrease in the isomer shift with the increase in persulfide content to the superior ability of $(S_2)^{2-}$ "to accept electrons from the metal by back-donation, and hence to reduce the isomer shift by reducing the shielding of the *s*-electrons from the nucleus."[26] More recently, similar effects were reported for Fe-S clusters with strong π acceptor ligands like CO.[27] Thus, the increase in the isomer shift during the S oxidation plateau cannot be because $(S_2)^{2-}$ is less covalent with Fe than S^{2-}, as the opposite is true. In fact, on the basis of covalency alone, the formation of more covalent persulfides during the S oxidation plateau should cause the isomer shift to decrease, not increase. We conclude that the isomer shift increase indeed indicates Fe reduction.

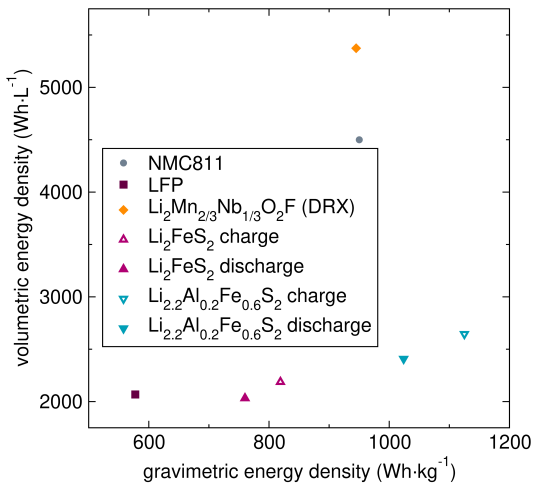

Figure S24: The volumetric energy density versus the gravimetric energy density for commercial Li-ion battery cathodes NMC811 and LFP, and the emerging cathodes DRX, Li_2FeS_2, and $Li_{2.2}Al_{0.2}Fe_{0.6}S_2$. Among these materials, $Li_{2.2}Al_{0.2}Fe_{0.6}S_2$ exhibits the highest gravimetric energy density. Relevant values and references for determining the gravimetric and volumetric energy densities are provided in Table S9.

Table S9: Relevant values and references used to determine the gravimetric and volumetric energy densities shown in Figure S24. For the emerging cathodes, i.e., DRX and those presented here, we also specify the rate in mA/g at which the performance metrics are reported.

relevant values and gravimetric and volumetric energy densities of commercial and emerging Li-ion battery cathodes									
	rate (mA/g)	mole Li^+ per f.u. cycled	molecular weight (g/mole)	normalized unit cell volume ($Å^3$)	gravimetric capacity ($mAh \cdot g^{-1}$)	volumetric capacity ($mAh \cdot L^{-1}$)	average voltage (V)	gravimetric energy density ($Wh \cdot kg^{-1}$)	volumetric energy density ($Wh \cdot L^{-1}$)
$LiNi_{0.8}Mn_{0.1}Co_{0.1}O_2$ (NMC811)	-	0.9[29]	97.3	33.5[30]	250	1204	3.8[29]	950	4576
$LiFePO_4$ (LFP)	-	1.0	157.8	73.2[31]	170	608	3.4[32]	577	2068
$Li_2Mn_{2/3}Nb_{1/3}O_2F$ (DRX)	20	1.5[28]	132.5	38.7[28]	304	1729	3.1	945	5373
Li_2FeS_2 charge	20	1.67	133.8	83.2	334	892	2.452	819	2187
Li_2FeS_2 discharge	20	1.65	133.8	83.2	331	885	2.295	760	2032
$Li_{2.2}Al_{0.2}Fe_{0.6}S_2$ charge	23	1.98	118.3	83.5	449	1056	2.505	1125	2645
$Li_{2.2}Al_{0.2}Fe_{0.6}S_2$ discharge	23	1.97	118.3	83.5	446	1050	2.294	1024	2408

Bibliography

[1] Sharma, R. A. Equilibrium Phases Between Lithium Sulfide and Iron Sulfides. *J. Electrochem. Soc.* **1976**, *123*, 448.

[2] Brec, R.; Dugast, A.; Le Mehauté, A. Chemical and electrochemical study of the Li_xFeS_2 cathodic system ($0<x \leq 2$). *Mater. Res. Bull.* **1980**, *15*, 619–625.

[3] Dugast, A.; Brec, R.; Ouvrard, G.; Rouxel, J. Li_2FeS_2, a cathodic material for lithium secondary battery. *Solid State Ion.* **1981**, *5*, 375–378.

[4] Le Mehaute, A.; Brec, R.; Dugast, A.; Rouxel, J. The Li_xFeS_2 electrochemical system. *Solid State Ion.* **1981**, *3–4*, 185–189.

[5] Batchelor, R. J.; Einstein, F. W. B.; Jones, C. H. W.; Fong, R.; Dahn, J. R. Crystal structure of Li_2FeS_2. *Phys. Rev. B* **1988**, *37*, 3699–3702.

[6] Fong, R.; Dahn, J. R.; Jones, C. H. W. Electrochemistry of Pyrite-Based Cathodes for Ambient Temperature Lithium Batteries. *J. Electrochem. Soc.* **1989**, *136*, 3206.

[7] Brec, R.; Prouzet, E.; Ouvrard, G. Redox processes in the Li_xFeS_2/Li electrochemical system studied through crystal, Mössbauer, and EXAFS analyses. *J. Power Sources* **1989**, *26*, 325–332.

[8] Melendres, C. A.; Tani, B. Moessbauer spectra and lattice parameters of some new sulfide phases of iron. *J. Phys. Chem.* **1978**, *82*, 2850–2852.

[9] Blandeau, L.; Ouvrard, G.; Calage, Y.; Brec, R.; Rouxel, J. Transition-metal dichalcogenides from disintercalation processes. Crystal structure determination and Mossbauer study of Li_2FeS_2 and its disintercalates $Li_{2-x}FeS_2$ ($0.2\leq x \leq 2$). *J. Phys. C: Solid State Phys.* **1987**, *20*, 4271.

[10] Gard, P.; Sourisseau, C.; Ouvrard, G.; Brec, R. Infrared study of lithium intercalated phases in the Li_xFeS_2 system ($0\leq x \leq 2$). Characterization of a new iron disulfide. *Solid State Ion.* **1986**, *20*, 231–238.

[11] Barker, J.; Kendrick, E. Lithium-containing transition metal sulphide compounds. 2010.

[12] Barker, J.; Kendrick, E. The electrochemical insertion and safety properties of the low-cost Li-ion active material, Li_2FeS_2. *J. Power Sources* **2011**, *196*, 6960–6963.

[13] Kendrick, E.; Barker, J.; Bao, J.; Świątek, A. The rate characteristics of lithium iron sulfide. *J. Power Sources* **2011**, *196*, 6929–6933.

[14] Hansen, C. J.; Zak, J. J.; Martinolich, A. J.; Ko, J. S.; Bashian, N. H.; Kaboudvand, F.; Van der Ven, A.; Melot, B. C.; Nelson Weker, J.; See, K. A. Multielectron, Cation and Anion Redox in Lithium-Rich Iron Sulfide Cathodes. *J. Am. Chem. Soc.* **2020**, *142*, 6737–6749.

[15] Kim, S. S.; Agyeman-Budu, D. N.; Zak, J. J.; Andrews, J. L.; Li, J.; Melot, B. C.; Nelson Weker, J.; See, K. A. Effect of Metal *d* Band Position on Anion Redox in Alkali-Rich Sulfides. *Chem. Mater.* **2024**,

[16] Shoemaker, D. P.; Chung, D. Y.; Claus, H.; Francisco, M. C.; Avci, S.; Llobet, A.; Kanatzidis, M. G. Phase relations in $K_xFe_{2-y}Se_2$ and the structure of superconducting $K_xFe_2Se_2$ via high-resolution synchrotron diffraction. *Phys. Rev. B* **2012**, *86*, 184511.

[17] Baker, M. L.; Mara, M. W.; Yan, J. J.; Hodgson, K. O.; Hedman, B.; Solomon, E. I. *K*- and *L*-edge X-ray absorption spectroscopy (XAS) and resonant inelastic X-ray scattering (RIXS) determination of differential orbital covalency (DOC) of transition metal sites. *Coord. Chem. Rev.* **2017**, *345*, 182–208.

[18] Kowalska, J. K.; Hahn, A. W.; Albers, A.; Schiewer, C. E.; Bjornsson, R.; Lima, F. A.; Meyer, F.; DeBeer, S. X-ray Absorption and Emission Spectroscopic Studies of $[L_2Fe_2S_2]^n$ Model Complexes: Implications for the Experimental Evaluation of Redox States in Iron–Sulfur Clusters. *Inorg. Chem.* **2016**, *55*, 4485–4497.

[19] Tokuda, M.; Yoshiasa, A.; Mashimo, T.; Arima, H.; Hongu, H.; Tobase, T.; Nakatsuka, A.; Sugiyama, K. Crystal structure refinement of $MnTe_2$, $MnSe_2$, and MnS_2: cation-anion and anion–anion bonding distances in pyrite-type structures. *Z. Kristallogr. Cryst. Mater.* **2019**, *234*, 371–377.

[20] Fasiska, E. J. Some defect structures of iron sulfide. *Phys. Status Solidi A* **1972**, *10*, 169–173.

[21] Montano, P. A.; Seehra, M. S. Magnetism of iron pyrite (FeS_2) — a Mössbauer study in an external magnetic field. *Solid State Commun.* **1976**, *20*, 897–898.

[22] Garg, V. K.; Liu, Y. S.; Puri, S. P. Mössbauer electric field gradient study in FeS_2 (pyrite). *J. Appl. Phys.* **1974**, *45*, 70–72.

[23] Gosselin, J. R.; Townsend, M. G.; Tremblay, R. J.; Webster, A. H. Mössbauer investigation of synthetic single crystal monoclinic Fe_7S_8. *Mater. Res. Bull.* **1975**, *10*, 41–49.

[24] Coucouvanis, D.; Lippard, S. J. Preparation and structural characterization of six-coordinate iron(III) complexes containing the Fe-S-S linkage. *J. Am. Chem. Soc.* **1968**, *90*, 3281–3282.

[25] Coucouvanis, D.; Lippard, S. J. Crystal and molecular structure of thio-p-toluoyldisulfidobis (dithio-p-toluato)iron(III). *J. Am. Chem. Soc.* **1969**, *91*, 307–311.

[26] Rickards, R.; Johnson, C. E.; Hill, H. a. O. Mössbauer effect and electron paramagnetic resonance investigation of some complexes of iron with 'persulphide' ligands. *J. Chem. Soc., A* **1971**, 1755–1757.

[27] Brown, A. C.; Thompson, N. B.; Suess, D. L. M. Evidence for Low-Valent Electronic Configurations in Iron–Sulfur Clusters. *J. Am. Chem. Soc.* **2022**, *144*, 9066–9073.

[28] Lee, J.; Kitchaev, D. A.; Kwon, D.-H.; Lee, C.-W.; Papp, J. K.; Liu, Y.-S.; Lun, Z.; Clément, R. J.; Shi, T.; McCloskey, B. D.; Guo, J.; Balasubramanian, M.; Ceder, G. Reversible Mn^{2+}/Mn^{4+} double redox in lithium-excess cathode materials. *Nature* **2018**, *556*, 185–190.

[29] Manthiram, A.; Song, B.; Li, W. A perspective on nickel-rich layered oxide cathodes for lithium-ion batteries. *Energy Storage Mater.* **2017**, *6*, 125–139.

[30] Ying, B. et al. Monitoring the Formation of Nickel-Poor and Nickel-Rich Oxide Cathode Materials for Lithium-Ion Batteries with Synchrotron Radiation. *Chem. Mater.* **2023**, *35*, 1514–1526.

[31] Yoshinari, T.; Mori, T.; Otani, K.; Munesada, T.; Yamamoto, K.; Uchiyama, T.; Fukuda, K.; Koyama, Y.; Hagiwara, R.; Orikasa, Y.; Uchimoto, Y. Quantitative Elucidation of the Non-Equilibrium Phase Transition in $LiFePO_4$ via the Intermediate Phase. *Chem. Mater.* **2019**, *31*, 7160–7166.

[32] Yamada, A.; Chung, S. C.; Hinokuma, K. Optimized $LiFePO_4$ for Lithium Battery Cathodes. *J. Electrochem. Soc.* **2001**, *148*, A224.

SUPPLEMENTARY INFORMATION–CHAPTER 4

Table S10: Rietveld refinement results for sXRD patterns of $Li_{2.2}Al_{0.2}Fe_{0.6}S_2$, $Li_2Cu_{0.2}Al_{0.2}Fe_{0.6}S_2$, and $Li_{1.8}Cu_{0.4}Al_{0.2}Fe_{0.6}S_2$ using the $P2_1/m$ monoclinic space group unit cell, corresponding to Figure 4.2a, b, and c, respectively.

All Rietveld refinement results														
	lattice parameters							atomic parameters						
	R_{wp} (%)	reduced χ^2	a (Å)	b (Å)	c (Å)	β (°)	V (Å^3)	atom label	Wyckoff site	x	y	z	occu-pancy	U_{iso}
$Li_{2.2}Al_{0.2}Fe_{0.6}S_2$	3.98	0.02	6.795	7.839	6.269	89.98	333.964	S1	2e	-0.158	0.750	0.744	1.0	0.057
								S2	2e	0.175	0.750	0.252	1.0	0.002
								S3	4f	0.350	0.504	0.749	1.0	0.014
								Al1	2e	0.146	0.750	0.628	0.4	0.005
								Fe1	2e	0.146	0.750	0.628	0.3	0.005
								Fe2	4f	0.348	0.012	0.360	0.3	0.020
								Fe3	2e	0.167	0.250	0.640	0.3	0.020
								Li1	2e	0.146	0.750	0.628	0.3	0.015
								Li2	4f	0.348	0.012	0.360	0.7	0.014
								Li3	2e	0.167	0.250	0.640	0.3	0.018
								Li4	2e	0.500	0.750	0.000	1.0	0.027
								Li5	2a	0.000	0.000	0.000	1.0	0.028

continued on next page

continued from previous page

	lattice parameters							atomic parameters						
	R_{wp} (%)	reduced χ^2	a (Å)	b (Å)	c (Å)	β (°)	V (Å^3)	atom label	Wyckoff site	x	y	z	occu-pancy	U_{iso}
								S1	2e	-0.158	0.750	0.755	1.0	0.016
								S2	2e	0.176	0.750	0.231	1.0	0.004
								S3	4f	0.349	0.512	0.747	1.0	0.015
								Al1	2e	0.146	0.750	0.609	0.4	0.005
								Fe1	2e	0.146	0.750	0.609	0.3	0.020
								Fe2	4f	0.345	0.003	0.358	0.3	0.020
								Fe3	2e	0.158	0.250	0.642	0.3	0.020
$Li_2Cu_{0.2}Al_{0.2}Fe_{0.6}S_2$	7.37	0.10	6.756	7.781	6.272	89.98	329.743	Li1	2e	0.146	0.750	0.609	0.2	0.015
								Li2	4f	0.345	0.003	0.358	0.6	0.014
								Li3	2e	0.158	0.250	0.642	0.6	0.018
								Li4	2e	0.500	0.750	0.000	1.0	0.027
								Li5	2a	0.000	0.000	0.000	1.0	0.028
								Cu1	2e	0.146	0.750	0.609	0.1	0.015
								Cu2	4f	0.345	0.003	0.358	0.1	0.015
								Cu3	2e	0.158	0.250	0.642	0.1	0.015

continued on next page

continued from previous page

	lattice parameters							atomic parameters						
	R_{wp} (%)	reduced χ^2	a (Å)	b (Å)	c (Å)	β (°)	V (Å^3)	atom label	Wyckoff site	x	y	z	occu-pancy	U_{iso}
								S1	2e	-0.160	0.750	0.770	1.0	0.016
								S2	2e	0.162	0.750	0.243	1.0	0.004
								S3	4f	0.309	0.481	0.741	1.0	0.015
								Al1	2e	0.187	0.750	0.644	0.4	0.005
								Fe1	2e	0.187	0.750	0.644	0.3	0.020
								Fe2	4f	0.334	-0.007	0.367	0.3	0.020
								Fe3	2e	0.160	0.250	0.610	0.3	0.020
$Li_{1.8}Cu_{0.4}Al_{0.2}Fe_{0.6}S_2$	8.61	0.13	6.691	7.761	6.284	90.19	326.346	Li1	2e	0.187	0.750	0.644	0.1	0.015
								Li2	4f	0.334	-0.007	0.367	0.5	0.014
								Li3	2e	0.160	0.250	0.610	0.5	0.018
								Li4	2e	0.500	0.750	0.000	1.0	0.027
								Li5	2a	0.000	0.000	0.000	1.0	0.028
								Cu1	2e	0.187	0.750	0.644	0.2	0.015
								Cu2	4f	0.334	-0.007	0.367	0.2	0.015
								Cu3	2e	0.160	0.250	0.610	0.2	0.015

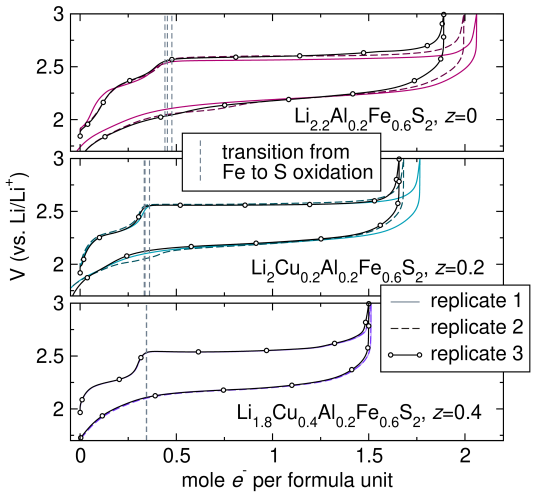

Figure S25: The first cycles of three replicate cells from three separate cells of (a) $Li_{2.2}Al_{0.2}Fe_{0.6}S_2$, (b) $Li_2Cu_{0.2}Al_{0.2}Fe_{0.6}S_2$, and (c) $Li_{1.8}Cu_{0.4}Al_{0.2}Fe_{0.6}S_2$, all cycled at $C/10$ based on 1 e^- per formula unit. We mark the transition point from the sloping region associated with Fe oxidation to the S oxidation plateau during charge for each replicate with a dashed vertical gray line. The corresponding average capacity and standard deviations associated with the two regions are in Table S11.

Table S11: The averages and standard deviations of the first cycle charge capacities of the three replicates of $Li_{2.2}Al_{0.2}Fe_{0.6}S_2$, $Li_2Cu_{0.2}Al_{0.2}Fe_{0.6}S_2$, and $Li_{1.8}Cu_{0.4}Al_{0.2}Fe_{0.6}S_2$ in Figure S25.

	first cycle charge capacities (mole e^- per formula unit)		
	Fe oxidation sloping region	S oxidation plateau	total oxidation
$Li_{2.2}Al_{0.2}Fe_{0.6}S_2$	0.46 ± 0.02	1.52 ± 0.09	1.98 ± 0.09
$Li_2Cu_{0.2}Al_{0.2}Fe_{0.6}S_2$	0.34 ± 0.01	1.36 ± 0.04	1.70 ± 0.06
$Li_{1.8}Cu_{0.4}Al_{0.2}Fe_{0.6}S_2$	0.34 ± 0.0004	1.16 ± 0.01	1.51 ± 0.01

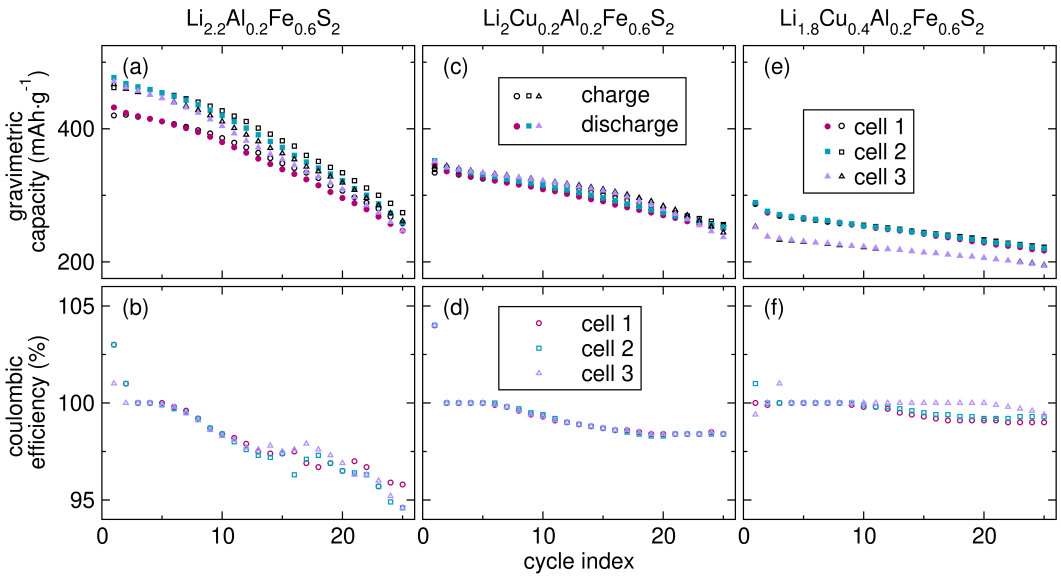

Figure S26: (a) The gravimetric charge and discharge capacities and (b) the coulombic efficiencies of three replicate cells of $Li_{2.2}Al_{0.2}Fe_{0.6}S_2$ cycled at $C/10$ based on 1 mole e^- per f.u. for 25 cycles. Panels (c) and (d), and (e) and (f) show the same corresponding data for $Li_2Cu_{0.2}Al_{0.2}Fe_{0.6}S_2$ and $Li_{1.8}Cu_{0.4}Al_{0.2}Fe_{0.6}S_2$, respectively. The average and standard deviation of the three replicates in (a) and (c) are shown in Figure 4.3d in the main text.

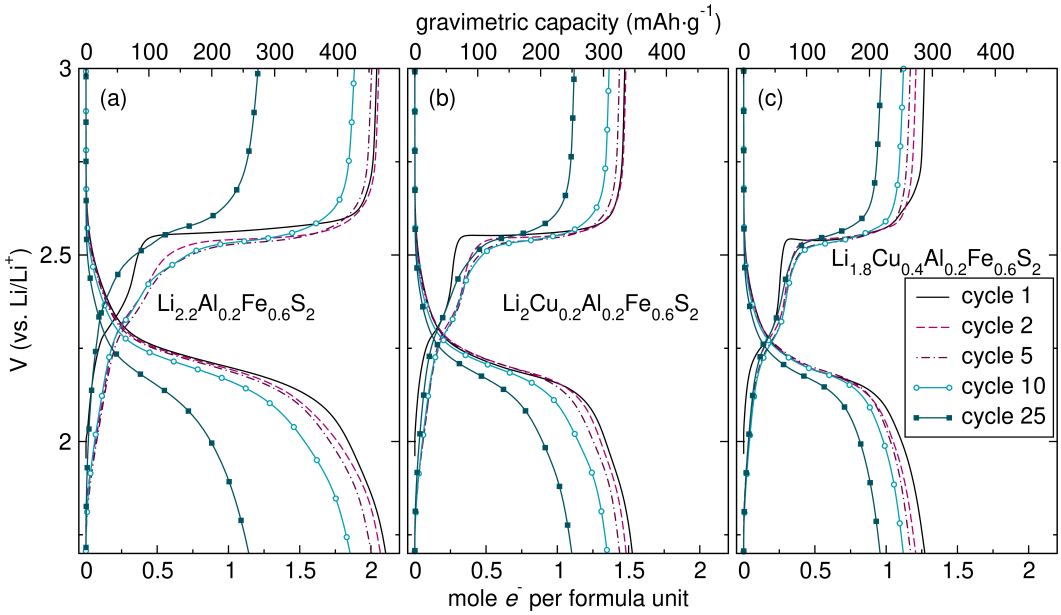

Figure S27: Representative galvanostatic cycles 1, 5, 10, and 25 of (a) $Li_{2.2}Al_{0.2}Fe_{0.6}S_2$, (b) $Li_2Cu_{0.2}Al_{0.2}Fe_{0.6}S_2$, and (c) $Li_{1.8}Cu_{0.4}Al_{0.2}Fe_{0.6}S_2$, all cycled at $C/10$ based on 1 mole e^- per formula unit.

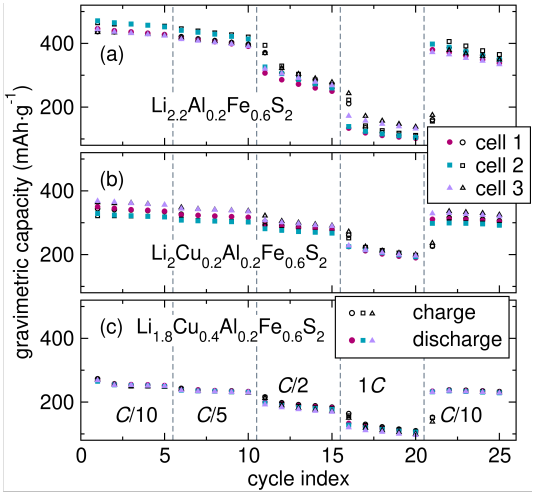

Figure S28: The gravimetric charge and discharge capacities of three replicate cells of (a) $Li_{2.2}Al_{0.2}Fe_{0.6}S_2$, (b) $Li_2Cu_{0.2}Al_{0.2}Fe_{0.6}S_2$, and (c) $Li_{1.8}Cu_{0.4}Al_{0.2}Fe_{0.6}S_2$ subjected to rate capability tests of 5 cycles each at *C*/10, *C*/5, *C*/2, 1C, and again at *C*/10. All *C* rates are based on 1 e^- per formula unit. The average and standard deviation of these replicates are shown in Figure 4.3e in the main text.

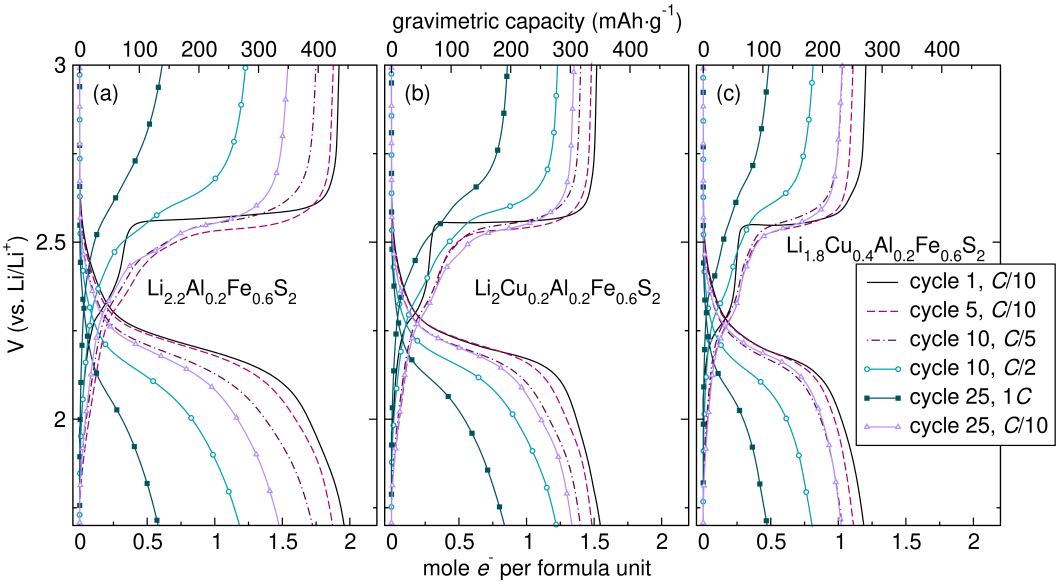

Figure S29: Representative galvanostatic cycles 1 (at *C*/10), 5 (at *C*/10), 10 (at *C*/5), 15 (at *C*/2), 20 (at 1*C*), and 25 (again at *C*/10) of (a) $Li_{2.2}Al_{0.2}Fe_{0.6}S_2$, (b) $Li_2Cu_{0.2}Al_{0.2}Fe_{0.6}S_2$, and (c) $Li_{1.8}Cu_{0.4}Al_{0.2}Fe_{0.6}S_2$ from the rate capability tests shown in Figure S28. All *C* rates are based on 1 mole e^- per formula unit.

Table S12: The averages and standard deviations of the first cycle charge and discharge gravimetric capacities, average voltages, and energy densities of the three replicates of $Li_{2.2}Al_{0.2}Fe_{0.6}S_2$, $Li_2Cu_{0.2}Al_{0.2}Fe_{0.6}S_2$, and $Li_{1.8}Cu_{0.4}Al_{0.2}Fe_{0.6}S_2$ in Figure S25.

	first cycle performance metrics					
	charge			discharge		
	gravimetric capacity ($mAh \cdot g^{-1}$)	average voltage (V)	energy density ($Wh \cdot kg^{-1}$)	gravimetric capacity ($mAh \cdot g^{-1}$)	average voltage (V)	energy density ($Wh \cdot kg^{-1}$)
$Li_{2.2}Al_{0.2}Fe_{0.6}S_2$	449±20	2.505±0.007	1125±49	446±24	2.294±0.004	1024±55
$Li_2Cu_{0.2}Al_{0.2}Fe_{0.6}S_2$	352±12	2.482±0.011	873±29	366±15	2.298±0.002	841±35
$Li_{1.8}Cu_{0.4}Al_{0.2}Fe_{0.6}S_2$	287±1	2.475±0.001	710±3	228±1	2.305±0.002	664±2

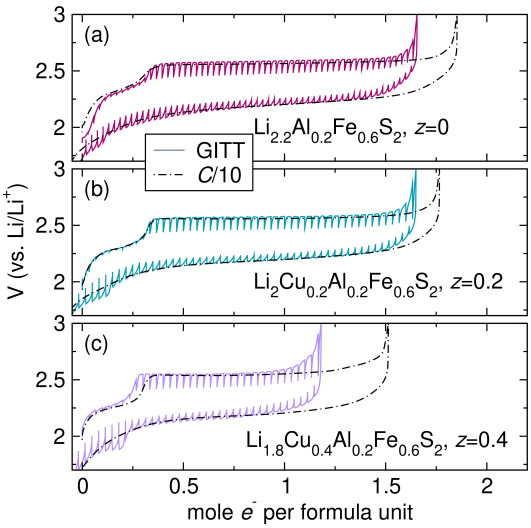

Figure S30: GITT curve and accompanying galvanostatic curve at $C/10$ of the first cycle of (a) $Li_{2.2}Al_{0.2}Fe_{0.6}S_2$, (b) $Li_2Cu_{0.2}Al_{0.2}Fe_{0.6}S_2$, and (c) $Li_{1.8}Cu_{0.4}Al_{0.2}Fe_{0.6}S_2$. GITT was obtained at $C/10$ based on 1 mole e^- per f.u. for 20 min separated by 4 h rest periods at open-circuit.

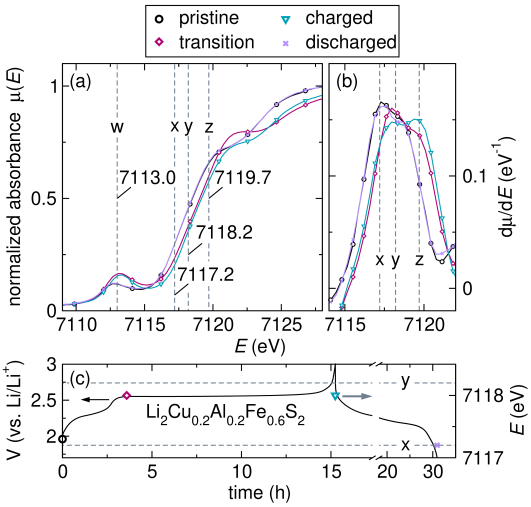

Figure S31: (a) *Ex-situ* Fe K-edge XAS spectra and (b) first derivative of the rising edge for $Li_2Cu_{0.2}Al_{0.2}Fe_{0.6}S_2$. (c) The energies of the maxima of the first derivatives at each of the SOCs overlaid with the corresponding galvanostatic cycling data. The dashed lines in all panels indicate the approximate positions of the pre-edge w, at 7113.0 eV, the two rising edges observed at different SOCs, x and y, at 7117.2 eV and 7118.2 eV, respectively, and the additional high energy feature, z, at 7119.7 eV.

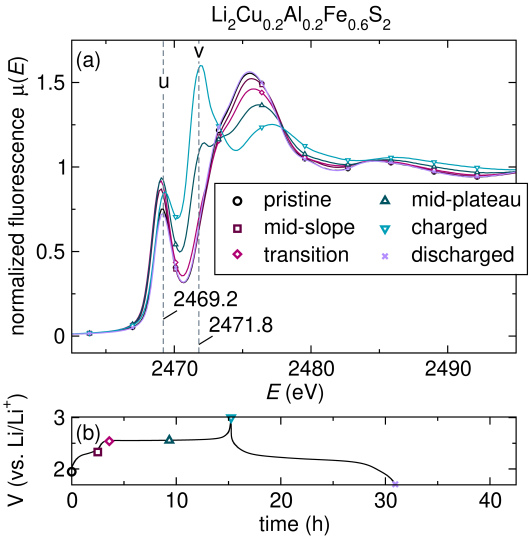

Figure S32: (a) *Ex-situ* S K-edge XAS and (b) a representative first cycle curve indicating the SOCs at which the XAS data was collected for $Li_2Cu_{0.2}Al_{0.2}Fe_{0.6}S_2$. The dashed lines in (a) indicate the two pre-edge features *u* and *v*, at 2469.2 eV and 2471.8 eV, respectively.

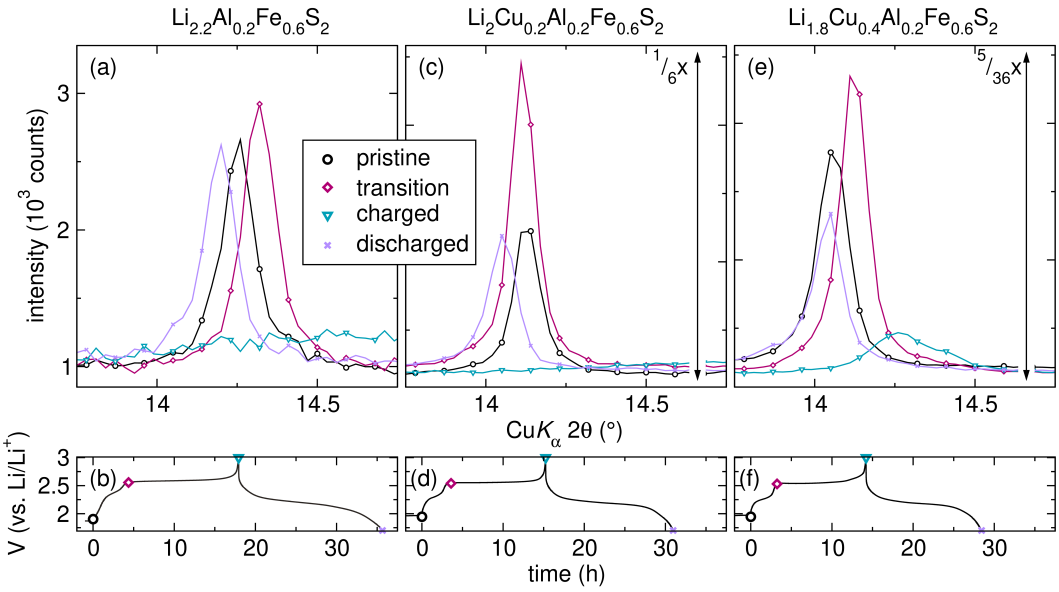

Figure S33: *Ex-situ* XRD, focused on the (0 0 1) reflection between ≈13° to 16° 2θ, of (a) $Li_{2.2}Al_{0.2}Fe_{0.6}S_2$ in the pristine, transition, charged, and discharged states with (b) accompanying galvanostatic data. The same corresponding data for $Li_2Cu_{0.2}Al_{0.2}Fe_{0.6}S_2$ and $Li_{1.8}Cu_{0.4}Al_{0.2}Fe_{0.6}S_2$ is shown in panels (c) and (d), and (e) and (f), respectively.

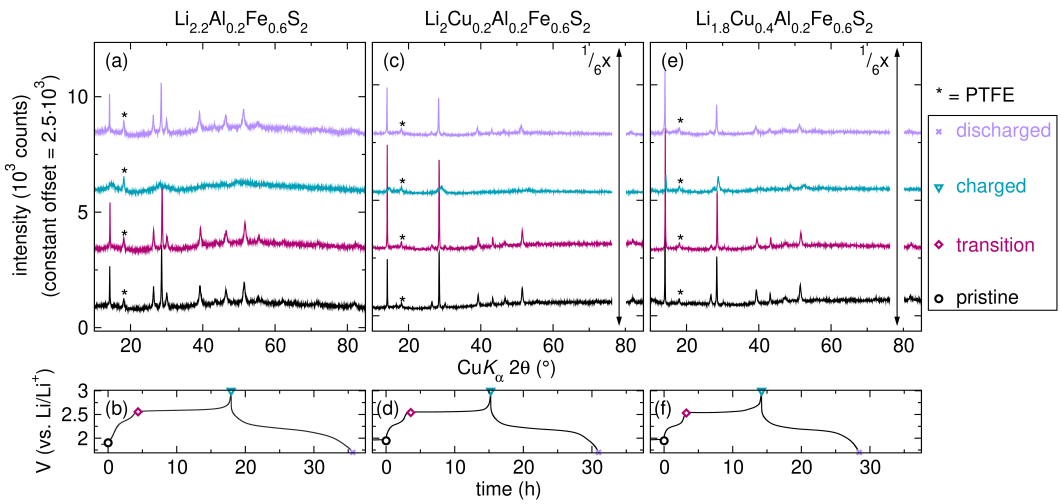

Figure S34: Full *ex-situ* XRD patterns between 10 to 85 2θ (°) of (a) $Li_{2.2}Al_{0.2}Fe_{0.6}S_2$ in the pristine, transition, charged, and discharged states with (b) accompanying galvanostatic data. The same corresponding data for $Li_2Cu_{0.2}Al_{0.2}Fe_{0.6}S_2$ and $Li_{1.8}Cu_{0.4}Al_{0.2}Fe_{0.6}S_2$ is shown in panels (c) and (d), and (e) and (f), respectively. Figure S33 suggests that long-range order is restored in the discharged state by showing the recovery of the layer spacing associated with the (0 0 1) reflection. The near-identical full XRD patterns in the pristine and discharged states shown here confirm that this structural restoration extends to the entire long-range order, not just the layer spacing.

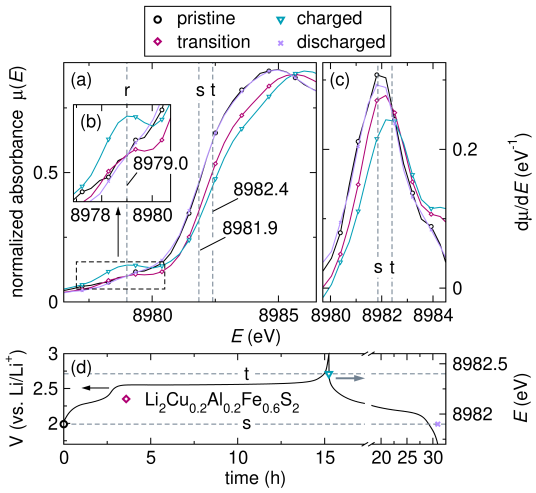

Figure S35: (a) *Ex-situ* Cu K-edge XAS spectra, (b) magnified pre-edge region, and (c) first derivative of the rising edge regions for $Li_2Cu_{0.2}Al_{0.2}Fe_{0.6}S_2$. (d) The energies of the maxima of the first derivatives at each of the SOCs are overlaid with representative galvanostatic cycling data. The dashed lines in all panels indicate the approximate positions of the pre-edge r, at 8979.0 eV, and the lowest and highest energy rising edge positions observed at different SOCs, s and t, at 8981.9 eV and 8982.4 eV, respectively.

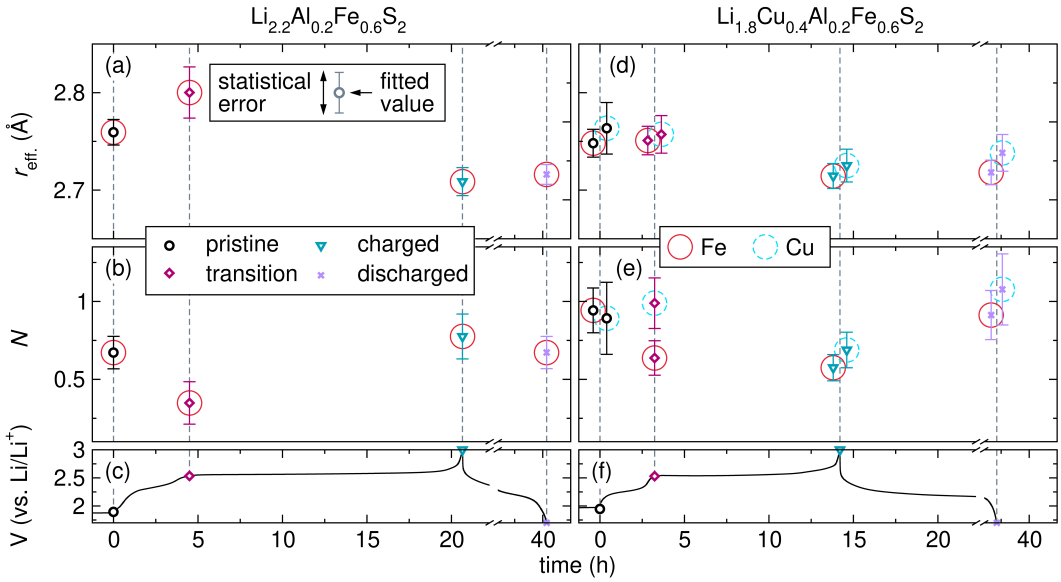

Figure S36: The second shell values of (a) $r_{\text{eff.}}$ and (b) N from Fe K-edge EXAFS analysis of $Li_{2.2}Al_{0.2}Fe_{0.6}S_2$, with (c) accompanying galvanostatic data indicating the SOCs at which EXAFS analysis is conducted. Panels (d), (e), and (f), respectively, indicate the same corresponding data for $Li_{1.8}Cu_{0.4}Al_{0.2}Fe_{0.6}S_2$. Panels (d) and (e) additionally include $r_{\text{eff.}}$ and N, respectively, from Cu K-edge EXAFS analysis of $Li_{1.8}Cu_{0.4}Al_{0.2}Fe_{0.6}S_2$. All $r_{\text{eff.}}$ and N values are shown with statistical error bars. Fe K-edge EXAFS data points are marked with solid red circles, while Cu K-edge EXAFS data points are marked with dashed cyan circles. The first shell data is discussed in the main text. The second shell data shows similar trends for $Li_{2.2}Al_{0.2}Fe_{0.6}S_2$ and $Li_{1.8}Cu_{0.4}Al_{0.2}Fe_{0.6}S_2$.

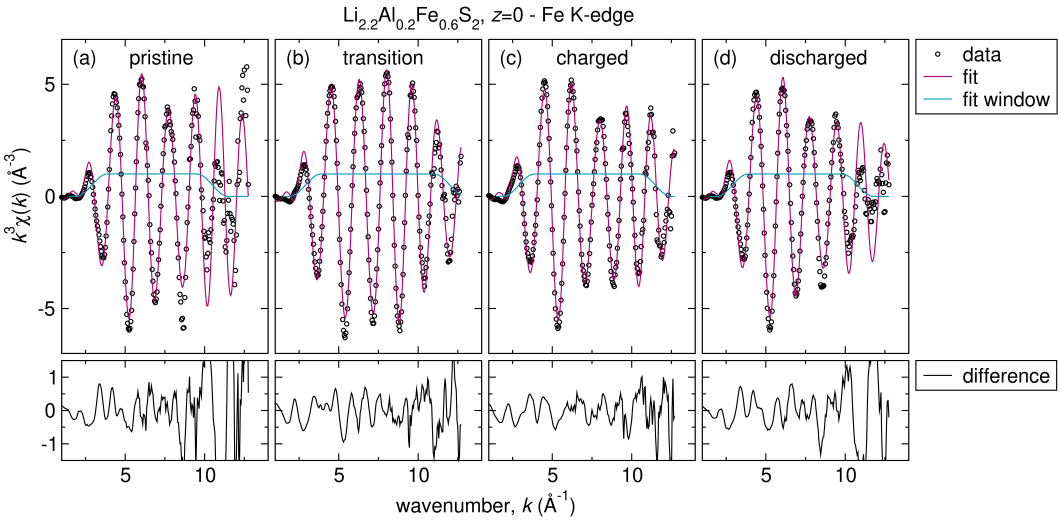

Figure S37: Fe K-edge EXAFS $k^3\chi(k)$ data, fit, fit window, and fit-data difference of the (a) pristine, (b) transition, (c) charged, and (d) discharged states of $Li_{2.2}Al_{0.2}Fe_{0.6}S_2$. The first shell data is discussed in the main text.

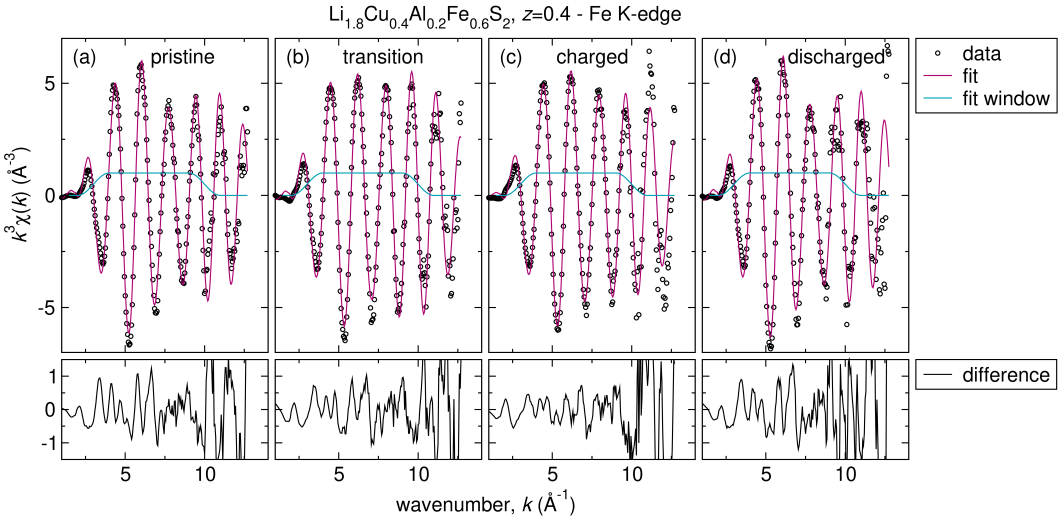

Figure S38: Fe K-edge EXAFS $k^3\chi(k)$ data, fit, fit window, and fit-data difference of the (a) pristine, (b) transition, (c) charged, and (d) discharged states of $Li_{1.8}Cu_{0.4}Al_{0.2}Fe_{0.6}S_2$.

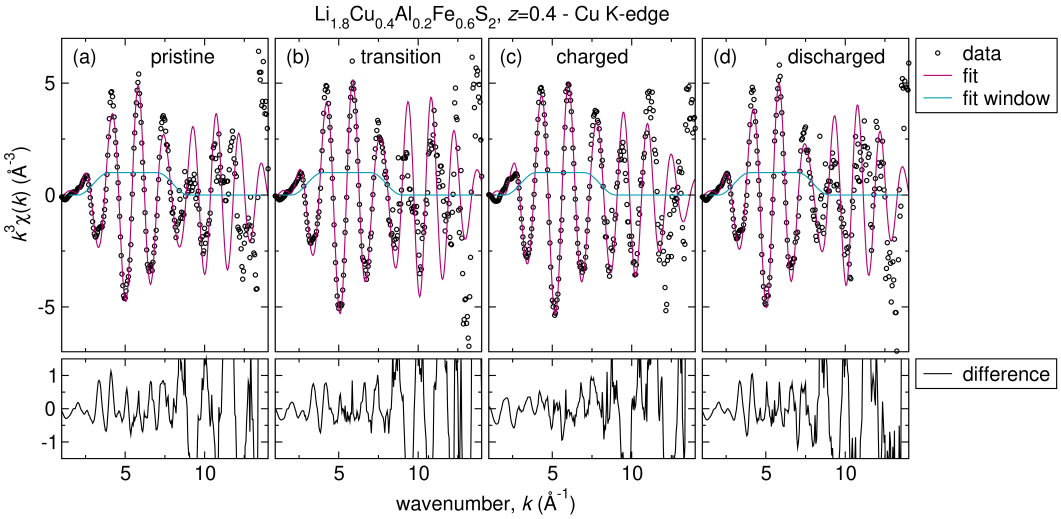

Figure S39: Cu K-edge EXAFS $k^3\chi(k)$ data, fit, fit window, and fit-data difference of the (a) pristine, (b) transition, (c) charged, and (d) discharged states of $Li_{1.8}Cu_{0.4}Al_{0.2}Fe_{0.6}S_2$.

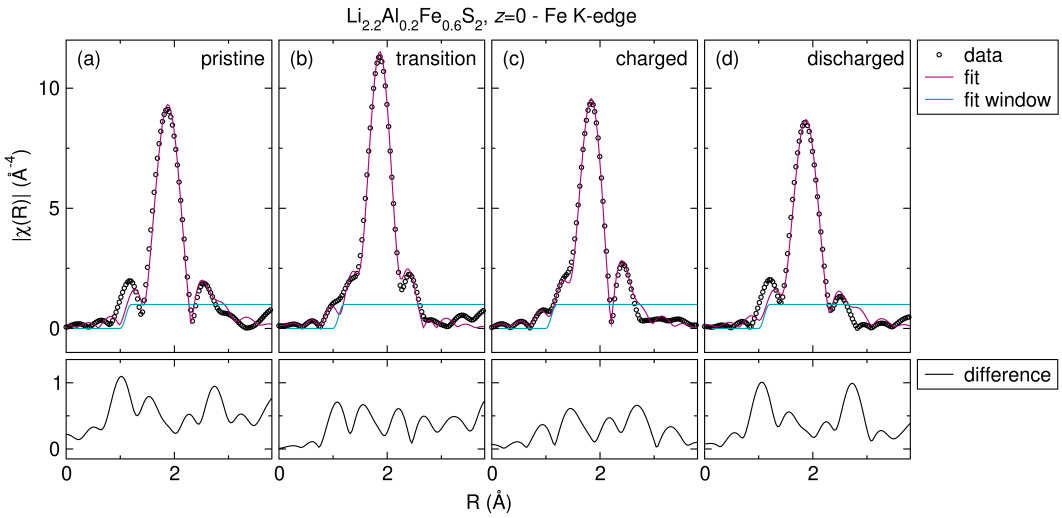

Figure S40: Fe K-edge EXAFS k^3-weighted $|\chi(R)|$ data, fit, fit window, and fit-data difference of the (a) pristine, (b) transition, (c) charged, and (d) discharged states of $Li_{2.2}Al_{0.2}Fe_{0.6}S_2$.

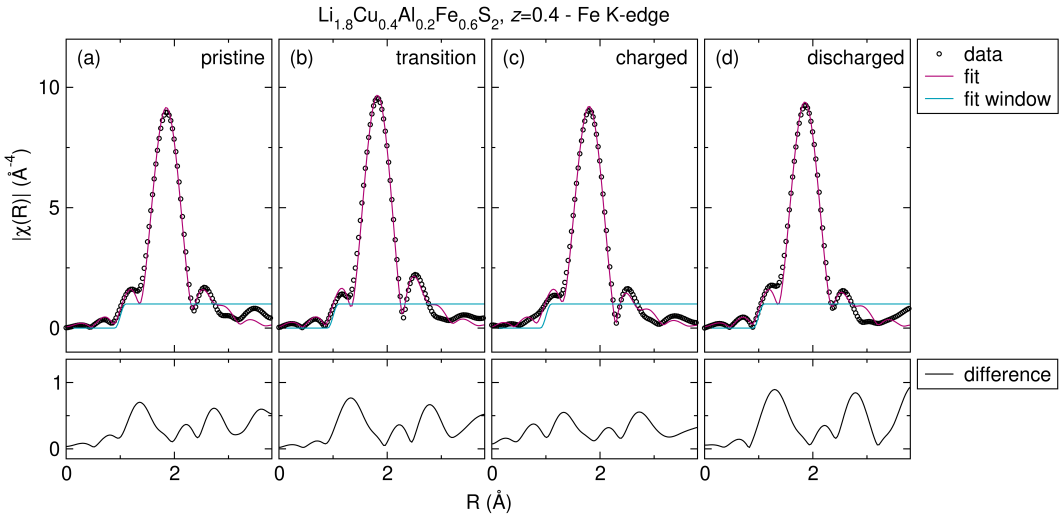

Figure S41: Fe K-edge EXAFS k^3-weighted $|\chi(R)|$ data, fit, fit window, and fit-data difference of the (a) pristine, (b) transition, (c) charged, and (d) discharged states of $Li_{1.8}Cu_{0.4}Al_{0.2}Fe_{0.6}S_2$.

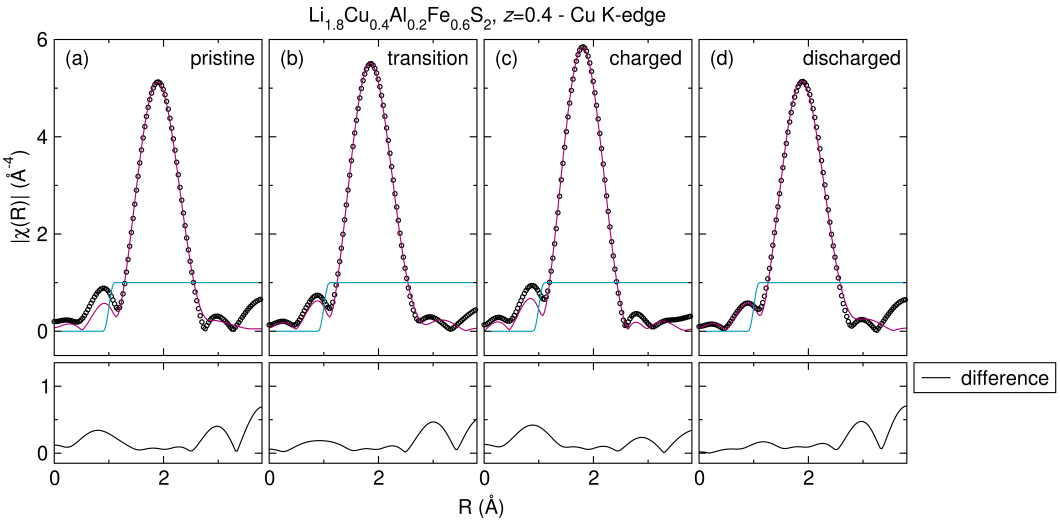

Figure S42: Cu K-edge EXAFS k^3-weighted $|\chi(R)|$ data, fit, fit window, and fit-data difference of the (a) pristine, (b) transition, (c) charged, and (d) discharged states of $Li_{1.8}Cu_{0.4}Al_{0.2}Fe_{0.6}S_2$.

Table S13: EXAFS fitting parameters for $Li_{2.2}Al_{0.2}Fe_{0.6}S_2$ and $Li_{1.8}Cu_{0.4}Al_{0.2}Fe_{0.6}S_2$.

$Li_{2.2}Al_{0.2}Fe_{0.6}S_2$, $z = 0$ – Fe K-edge							
state	S_0^2 intrinsic losses	ΔE_0 energy correction	σ^2 local disorder	$r_{\text{eff, first shell}}$ (Å) Fe-S bond length	$N_{\text{first shell}}$ Fe coord. number	$r_{\text{eff, second shell}}$ (Å) nearest Fe-Fe distance	$N_{\text{second shell}}$ edge-sharing tetrahedra occupancy
pristine	0.788	3.5±0.5	0.003±0.001	2.32±0.01	3.0±0.2	2.76±0.01	0.67±0.1
transition	0.788	3.5±0.5	0.003±0.001	2.26±0.01	3.3±0.2	2.80±0.03	0.35±0.14
charged	0.788	2.4±0.6	0.004±0.001	2.26±0.01	3.1±0.2	2.71±0.01	0.78±0.14
discharged	0.788	3.1±0.5	0.005±0.001	2.31±0.01	3.3±0.2	2.73±0.01	0.67±0.10

$Li_{1.8}Cu_{0.4}Al_{0.2}Fe_{0.6}S_2$, $z = 0.4$ – Fe K-edge							
state	S_0^2	ΔE_0	σ^2	$r_{\text{eff, first shell}}$ (Å)	$N_{\text{first shell}}$	$r_{\text{eff, second shell}}$ (Å)	$N_{\text{second shell}}$
pristine	0.723	2.4±0.6	0.004±0.001	2.31±0.01	3.9±0.2	2.75±0.01	0.94±0.14
transition	0.723	3.0±0.5	0.003±0.001	2.27±0.01	3.6±0.2	2.75±0.03	0.64±0.11
charged	0.723	0.5±0.4	0.004±0.001	2.26±0.01	3.8±0.1	2.71±0.01	0.57±0.08
discharged	0.723	3.6±0.7	0.004±0.001	2.31±0.01	3.9±0.3	2.74±0.02	0.91±0.16

continued on next page

continued from previous page

$Li_{1.8}Cu_{0.4}Al_{0.2}Fe_{0.6}S_2$, z = 0.4 – Cu K-edge

state	S_0^2	ΔE_0	σ^2	$r_{\text{eff, first shell}}$ (Å)	$N_{\text{first shell}}$	$r_{\text{eff, second shell}}$ (Å)	$N_{\text{second shell}}$
pristine	0.899	1.6±1.4	0.004±0.003	2.34±0.02	2.5±0.4	2.76±0.03	0.89±0.23
transition	0.899	1.7±1.1	0.004±0.002	2.31±0.01	2.7±0.3	2.76±0.02	0.99±0.16
charged	0.899	1.4±0.7	0.005±0.001	2.28±0.01	2.9±0.2	2.73±0.02	0.69±0.11
discharged	0.899	1.2±1.4	0.004±0.003	2.32±0.01	2.5±0.4	2.76±0.02	1.08±0.23

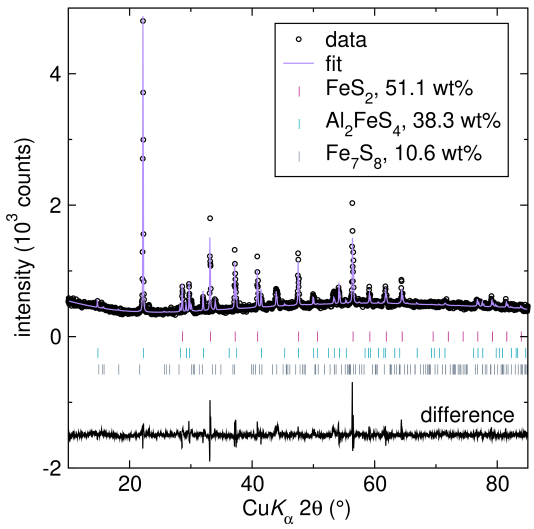

Figure S43: XRD of the attempted synthesis of $Al_{0.2}Fe_{0.6}S_2$. The Rietveld refinement (fit), reflection locations of each phase in the fit, the weight percent contribution of each phase, and the difference between the fit and data are all shown. All observed reflections are accounted for by a three-phase fit to FeS_2 (51.1 wt%), Al_2FeS_4 (38.3 wt%), and Fe_7S_8 (10.6 wt%).

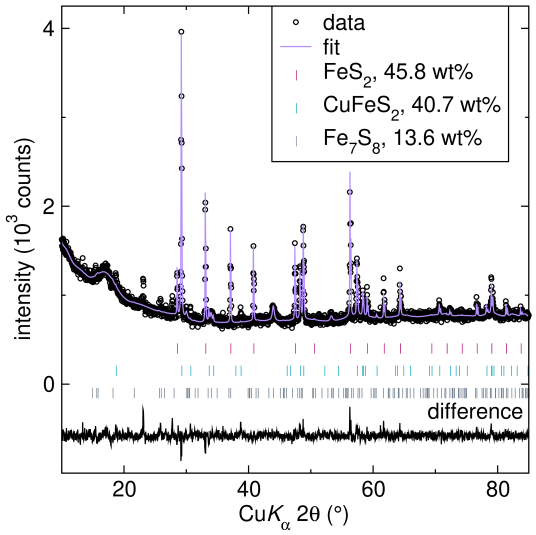

Figure S44: XRD of the attempted synthesis of $Cu_{0.2}Al_{0.2}Fe_{0.6}S_2$. The Rietveld refinement (fit), reflection locations of each phase in the fit, the weight percent contribution of each phase, and the difference between the fit and data are all shown. All but a few minor reflections between 20°and 30°2θ are accounted for by a three-phase fit to FeS_2 (45.8 wt%), $CuFeS_2$ (40.7 wt%), and Fe_7S_8 (13.6 wt%).

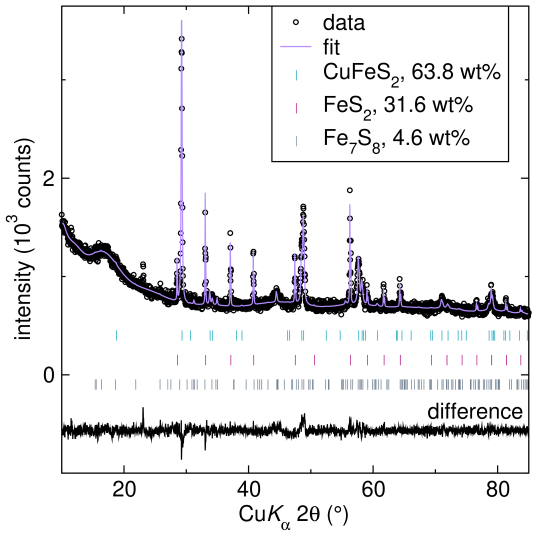

Figure S45: XRD of the attempted synthesis of $Cu_{0.4}Al_{0.2}Fe_{0.6}S_2$. The Rietveld refinement (fit), reflection locations of each phase in the fit, the weight percent contribution of each phase, and the difference between the fit and data are all shown. All but a few minor reflections between 20°and 30°2θ are accounted for by a three-phase fit to $CuFeS_2$ (63.8 wt%), FeS_2 (31.6 wt%), and Fe_7S_8 (4.6 wt%).

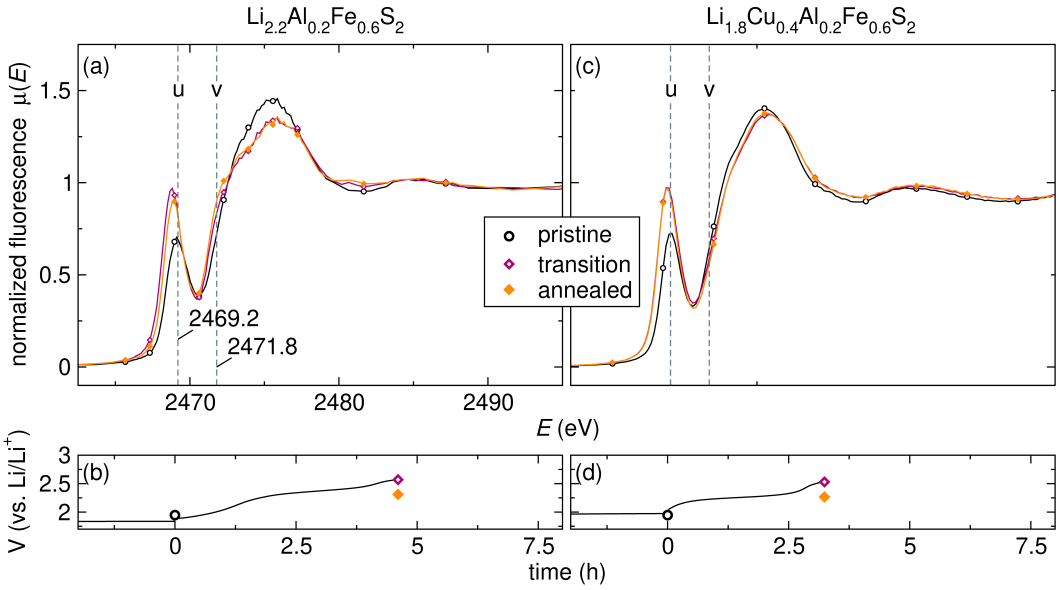

Figure S46: (a) S K-edge XAS spectra of $Li_{2.2}Al_{0.2}Fe_{0.6}S_2$ in the pristine, transition, and annealed states. (b) Galvanostatic data indicating the SOCs at which the XAS data was collected for $Li_{2.2}Al_{0.2}Fe_{0.6}S_2$. The corresponding data for $Li_{1.8}Cu_{0.4}Al_{0.2}Fe_{0.6}S_2$ are in (c) and (d), respectively. The dashed lines in (a) and (c) indicate the two pre-edge features u and v, at 2469.2 eV and 2471.8 eV, respectively.

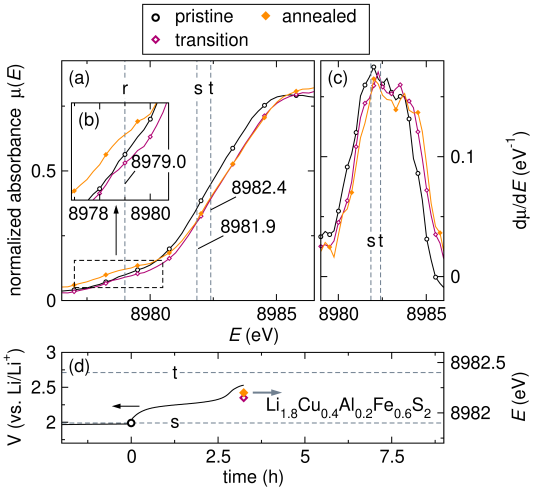

Figure S47: (a) *Ex-situ* Cu K-edge XAS spectra, (b) magnified pre-edge region, and (c) first derivative of the rising edge regions for $Li_{1.8}Cu_{0.4}Al_{0.2}Fe_{0.6}S_2$ in the pristine, transition, and annealed states. (d) The energies of the maxima of the first derivatives at each of the SOCs are overlaid with representative galvanostatic cycling data. The dashed lines in all panels indicate the approximate positions of the pre-edge r, at 8979.0 eV, and the lowest and highest energy rising edge positions observed at different SOCs, s and t, at 8981.9 eV and 8982.4 eV, respectively.

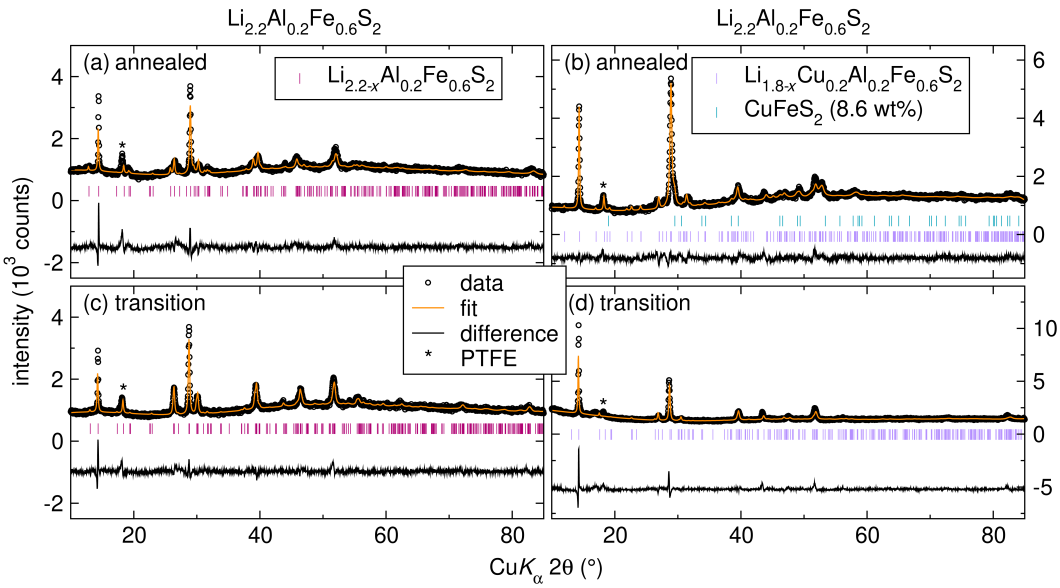

Figure S48: *Ex-situ* XRD of the annealed states of (a) $Li_{2.2}Al_{0.2}Fe_{0.6}S_2$ and (b) $Li_{1.8}Cu_{0.4}Al_{0.2}Fe_{0.6}S_2$, and the transition states of (c) $Li_{2.2}Al_{0.2}Fe_{0.6}S_2$ and (d) $Li_{1.8}Cu_{0.4}Al_{0.2}Fe_{0.6}S_2$. Each panel shows the Rietveld refinement (fit), reflection locations of each phase in the fit, and the difference between the fit and data. All patterns are described by a single phase, except $Li_{1.8}Cu_{0.4}Al_{0.2}Fe_{0.6}S_2$ in the annealed state, which is fit to two phases: chalcopyrite $CuFeS_2$ (8.6 wt%), and $Li_{1.8-x}Cu_{0.4}Al_{0.2}Fe_{0.6}S_2$ (91.4 wt%). While we label the phases in the fits as $Li_{2.2-x}$ in (a) and (c) or $Li_{1.8-x}$ in (b) and (d) to indicate delithiated samples, the crystallographic information files used for the refinements are those of pristine (fully lithiated) $Li_{2.2}Al_{0.2}Fe_{0.6}S_2$ and $Li_{1.8}Cu_{0.4}Al_{0.2}Fe_{0.6}S_2$.

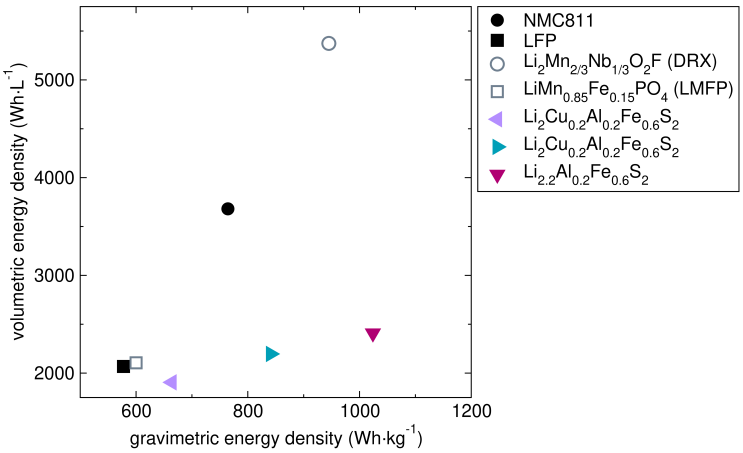

Figure S49: The volumetric energy density versus the gravimetric energy density for commercial Li-ion battery cathodes NMC811 and LFP, and the emerging cathodes DRX, Li_2FeS_2, $Li_{2.2}Al_{0.2}Fe_{0.6}S_2$, $Li_2Cu_{0.2}Al_{0.2}Fe_{0.6}S_2$, and $Li_{1.8}Cu_{0.4}Al_{0.2}Fe_{0.6}S_2$. Relevant values and references for determining the gravimetric and volumetric energy densities are provided in Table S14.

Table S14: Relevant values and references used to determine the gravimetric and volumetric energy densities shown in Figure S49. For the emerging cathodes, i.e., DRX, LMFP, and those presented here, we also specify the rate in mA/g at which the performance metrics are reported.

relevant values and gravimetric and volumetric energy densities of commercial and emerging Li-ion battery cathodes									
	rate (mA/g)	mole Li^+ per f.u. cycled	molecular weight (g/mole)	normalized unit cell volume ($Å^3$)	gravimetric capacity ($mAh \cdot g^{-1}$)	volumetric capacity ($mAh \cdot L^{-1}$)	average voltage (V)	gravimetric energy density ($Wh \cdot kg^{-1}$)	volumetric energy density ($Wh \cdot L^{-1}$)
$LiNi_{0.8}Mn_{0.1}Co_{0.1}O_2$ (NMC811)	-	0.73[2]	97.3	33.5[3]	201	969	3.8[2]	764	3681
$LiFePO_4$ (LFP)	-	1.0	157.8	73.2[4]	170	608	3.4[5]	577	2068
$Li_2Mn_{2/3}Nb_{1/3}O_2F$ (DRX)	20	1.5[1]	132.5	38.7[1]	304	1729	3.1	945	5373
$LiMn_{0.85}Fe_{0.15}PO_4$ (LMFP)	8.5	0.9[6]	157.0	74.3[6]	150	526	4	600	2105
$Li_{2.2}Al_{0.2}Fe_{0.6}S_2$ discharge	23	1.97	118.3	83.5	446	1050	2.294	1024	2408
$Li_2Cu_{0.2}Al_{0.2}Fe_{0.6}S_2$ discharge	21	1.77	129.6	82.4	366	955	2.298	841	2196
$Li_{1.8}Cu_{0.4}Al_{0.2}Fe_{0.6}S_2$ discharge	19	1.51	140.9	81.586	288.1	826.3	2.305	664	1905

Bibliography

[1] Lee, J.; Kitchaev, D. A.; Kwon, D.-H.; Lee, C.-W.; Papp, J. K.; Liu, Y.-S.; Lun, Z.; Clément, R. J.; Shi, T.; McCloskey, B. D.; Guo, J.; Balasubramanian, M.; Ceder, G. Reversible Mn^{2+}/Mn^{4+} double redox in lithium-excess cathode materials. *Nature* **2018**, *556*, 185–190.

[2] C. McNulty, R.; Hampson, E.; N. Cutler, L.; P. Grey, C.; M. Dose, W.; R. Johnson, L. Understanding the Limits of Li-NMC811 Half-Cells. *Journal of Materials Chemistry A* **2023**, *11*, 18302–18312.

[3] Ying, B. et al. Monitoring the Formation of Nickel-Poor and Nickel-Rich Oxide Cathode Materials for Lithium-Ion Batteries with Synchrotron Radiation. *Chem. Mater.* **2023**, *35*, 1514–1526.

[4] Yoshinari, T.; Mori, T.; Otani, K.; Munesada, T.; Yamamoto, K.; Uchiyama, T.; Fukuda, K.; Koyama, Y.; Hagiwara, R.; Orikasa, Y.; Uchimoto, Y. Quantitative Elucidation of the Non-Equilibrium Phase Transition in $LiFePO_4$ via the Intermediate Phase. *Chem. Mater.* **2019**, *31*, 7160–7166.

[5] Yamada, A.; Chung, S. C.; Hinokuma, K. Optimized $LiFePO_4$ for Lithium Battery Cathodes. *J. Electrochem. Soc.* **2001**, *148*, A224.

[6] Oh, S.-M.; Jung, H.-G.; Yoon, C. S.; Myung, S.-T.; Chen, Z.; Amine, K.; Sun, Y.-K. Enhanced Electrochemical Performance of Carbon–$LiMn_{1-x}Fe_xPO_4$ Nanocomposite Cathode for Lithium-Ion Batteries. *Journal of Power Sources* **2011**, *196*, 6924–6928.